Winter 1990

Computational study of red cell distribution in simple networks

Wen-Rong Fu
University of New Hampshire, Durham

Order Number 9119138

Computational study of red cell distribution in simple networks

Fu, Wen-Rong, Ph.D.

University of New Hampshire, 1990

U·M·I
300 N. Zeeb Rd.
Ann Arbor, MI 48106

Computational Study of Red Cell Distribution in Simple Networks

by

Wen-Rong Fu

BS. Tung-Hai University, Taiwan, 1982

MS, Oklahoma State University, 1987

DISSERTATION

Submitted to the University of New Hampshire

in Partial Fulfillment of

the Requirements for the Degree of

Doctor of Philosophy

in

Engineering

December, 1990

This dissertation has been examined and approved.

Russell T. Carr

Dissertation director, Russell T. Carr
Associate Professor of Chemical Engineering

Gael D. Ulrich
Professor of Chemical Engineering

Dale P. Barkey
Assistant Professor of Chemical Engineering

John P. McHugh
Assistant Professor of Mechanical Engineering

William J. Federspiel
Assistant Professor of Biomedical Engineering
Boston University

9-5-90

Date

DEDICATION

This is dedicated to my mother for all her love and support throughout the years.

ACKNOWLEDGEMENTS

I would like to thank my advisor, Dr. R. T. Carr, for his assistance and encouragement throughout the study.

Thanks to Dr. Ulrich, Dr. Barkey, Dr. McHugh and Dr. Federspiel for serving on my committee.

Thanks to Dr. L. L. Wickham for her valuable corrections of this preparation.

I would also like to thank Mr. J. Newell for the fabrication of the experimental devices.

The *in vitro* blood data used in this study are provided courtesy of Dr. Wickham and Dr. Carr.

This work was supported by National Heart, Lung, and Blood Institute Grants R23 HL34405 and R29 HL38313.

Contents

List of Tables

List of Figures

ABSTRACT

COMPUTATIONAL STUDY OF RED CELL
DISTRIBUTION IN SIMPLE NETWORKS

by

Wen-Rong Fu

University of New Hampshire, December, 1990

The distribution of red blood cells (RBC) across the vessel lumen is disturbed when blood flows through a junction. As the blood flows downstream from the junction, the RBC distribution "corrects" itself to regain its original symmetric character. A dispersion-type process has been used to model this rearrangement process in 3-dimensional branching tubes.

In this study, the disturbance in the RBC profile is quantified by tracing streamlines through the junction. The tracing technique is based on scaled-up dye studies. The computation starts at a location where the velocity profile is fully developed. Both uniform and parabolic RBC profiles are examined as possible, final symmetric distributions for the computations. Three velocity profiles are used alternatively. The dispersion convective equation of continuity in cylindrical geometry is solved with the method of finite differences. The resulting RBC concentration profiles is then used to compute flux-flow curves which are frequently used to examine plasma skimming phenomena.

The numerically computed flux-flow curves are compared to *in vitro* experimental data from 50 μm serial bifurcation replicas. The dispersion coefficient is used as an adjustable parameter to give the best match between computation and measurement. The averaged dispersion coefficients obtained agree with previous experimental data and show an enhanced dispersion.

Simple vascular networks are generated and the dispersion model is further applied to the networks. By calculating the discharge hematocrit of each branch vessel in the network the network Fahraeus effect is observed. Influences of flow disturbance to the downstream hematocrit are examined. The effects of flow heterogeneity and the dispersion model on the hematocrit heterogeneity are presented.

Chapter 1

Introduction

The quantitative study of blood flow started when Poiseuille (1840) [1] first used homogeneous fluids in his capillary experiments. Empirically, he established the famous relationship between flow, vessel diameter, fluid viscosity and pressure drop per unit length which is known as the Poiseuille's law. Generally speaking Pouiseuille's law does not apply to the microcirculatory system because it is not possible to think of the blood as a homogeneous fluid with constant viscosity. It is essential to treat it as a suspension of red cells and other formed elements in plasma. Obviously, simple straight tubes do not constitute the whole vessel network of a living body. Branching tubes are more characteristic of the vascular system.

Flowing blood accomplishes transportation of nutrients, heat, waste, and other substances for living animals among which the majority of the oxygen is delivered by the red blood cells. The distribution of red blood cells in the microcirculation also has an important effect on *in vivo* blood rheology. To evaluate the circulation it is not only important to understand the whole blood distribution in a circulating network but also the distributions of each of its constituents. This study is aimed at understanding human red blood cell distribution in branching tubes and its further extension to vascular networks.

1.1 Microcirculation

Most mass transfer between blood and tissue is thought to occur in the microcirculation. In the microcirculation vessels sizes range from about 100 to a few μm, including arterioles,

precapillaries, capillaries, postcapillaries, and venules . Direct measurement of flow conditions is extremely difficult not only because of the sensitivity to mechanical stimulus of the microvessels but also the tiny scale that is involved. Several unique features of blood flow in such small vessels are discussed below to differentiate microcirculation from the systemic circulation.

Apparently the homogeneous fluid approximation is not appropriate in microcirculation because even the largest vessels in microcirculation have only 15 to 20 times the diameter of a red cell. The Reynolds numbers (Re) are usually very low and decreases as microvessels get smaller. For example, in vessels of 100 μm the Re is typically around 0.5 and decreases to about 0.005 in 10 μm vessels [2.3.4]. This implies that the inertial forces are negligible compared to the viscous forces.

The pulsatile character of blood flow is much less important in microcirculation than in larger arteries. A dimensionless parameter, the Womersley number, defined as

$$\alpha = \frac{d}{2}\sqrt{\frac{\omega}{\nu}}$$

is used in pulsatile flow analysis to resemble the Reynolds number. The ω is the angular frequency, ν is the kinemetic viscosity, and d is the tube diameter. A small α (usually less than 1) indicates the flow is more likely to retain its velocity profile. The oscillation of pressure gradient (inertial effect) has little interference and the viscous force controls the profile. As α increases, phase lag starts to set in and the velocity profile is then distorted. In the microcirculation, α is usually very small. In a capillary, α is of the order of 10^{-3}. A "quasi-steady" state is obtained for such small Womersley numbers which means that the velocity profile is in phase and proportional to the local pressure gradient.

The red blood cell distribution through the microcirculation has been studied in a variety of tissues. For example, the tube and corresponding discharge hematocrit[1] in the rat mesentery have been reported [5]. A tube hematocrit is determined by instantaneously

[1]The hematocrit is a measure of red cell concentration which is defined as the volumetric fraction occupied by the red cells.

stopping the flow in a tube and measuring the packed red cell fraction. At fully-developed steady flow this is equal to the cross-sectional cell density. The tube and discharge hematocrits generally decrease through the arterial network and increase through the venous network. Similar results are reported in other microvascular networks. The ratio of the minimum micro-hematocrit to the systemic hematocrit are 0.45 in the rabbit omentum [6]; 0.20 [7]. 0.24 [8] in the hamster cremaster muscle; 0.26 in the cat mesentery [9]; and 0.36 in the rat mesentery [5]. It is suspected that the very low capillary hematocrit comes from the Fahraeus effect in single vessels and the repeated phase separation of red cells and plasma at vascular bifurcations [10].

The distributions of flow and pressure in microvascular networks have been studied extensively [8,11,12]. Most results are reported as average values grouped either by vessel diameter or by branching order. Some histograms of velocity distribution have been reported [7,12]. But systematic analysis of histograms based on vessel size or branching order is not yet available.

1.2 Blood in tubes

Blood is composed of particles (cells) and a medium (plasma) that suspends them. Several types of cell are present in the circulating blood but red cells most significantly influence the mechanical properties of normal blood. They occupy about 45 per cent of the volume in normal blood. If we count the cells in normal blood, for every thousand red cells only one to two white cells and 50 to 100 platelets are present. The platelet is so small that each platelet has only one tenth the volume of a red cell. Thus, more than 95 per cent of the suspended phase is occupied by red blood cells. The compositions of human blood and characteristics of blood cells are illustrated in Table 1.1.

The disk-shaped mammalian red blood cell has a very thin isotropic membrane [13] with viscous hemoglobin solution enclosed. It is easier to bend than to stretch the membrane, making red cells undergo constant surface area deformations in response to stresses [14].

The suspending medium, plasma containing various salts, lipids and proteins, is usually

Table 1.1: Cells in human blood

Cell	No. per mm^3	Unstressed shape and dimensions (μm)	Volume conc. (%) in blood
Erythrocytes	$4-6*10^6$	Biconcave disc $8*1-3$	45
Leukocytes	$4-11*10^3$	Roughly	1
Neutrophils	$1.5-7.5*10^3$	spherical	
Eosinophils	$0-4*10^2$	$7-22$	
Basophils	$0-2*10^2$		
Lymphocytes	$1-4.5*10^3$		
Monocytes	$0-8*10^2$		
Platelets	$250-500*10^3$	Rounded or oval $2-4$	

considered as an aqueous solution and has proven to be a Newtonian fluid [15]. Macromolecules in plasma, for example fibrinogen and globulin, can bridge cell surfaces and cause red cells to aggregate face to face and form rouleaux.

The extent of RBC aggregation and deformation predominantly determines the blood rheological properties. Experimental results based on tube, cone-and-plate, and Couette viscometers show non-Newtonian behavior for blood. Its apparent viscosity varies with hematocrit and red cell aggregation (shear rate dependent). At very low shear rate the red cell aggregation is responsible for the non-Newtonian behavior. When the shear rate is raised high enough to break all the cell rouleaux (approximately 100-200/sec for normal blood), cell deformations contribute to the non-Newtonian behavior. At higher shear rates (approximately >1000/sec for 45% hematocrit at 37°C), cell aggregates are completely broken and cell deformation becomes less important. The apparent viscosity no longer varies with shear rate and the blood can be approximated by a Newtonian fluid [17] if the hematocrit is held unchanged. In addition to the shear rate, hematocrit is another

decisive variable that affects the blood rheological properties. As a consequence of the small diameter of vessels in the microcirculation, wall shear rates can be considerably higher than in the large vessels, sometimes on the order of 1000 sec^{-1}. At these higher shear rates. Fahraeus and Lindqvist [18] measured the blood apparent viscosity (viscosity derived from the Poiseulle equation) in various diameters of tubes. They found that for tubes with diameters less than about 500 μm the apparent viscosity decreased with decreasing diameters down to approximately 60 μm. This has been known as the Fahraeus-Lindqvist effect. Other investigations have shown the Fahraeus-Lindqvist effect continues down to about 8 μm diameter. Barbee and Cokelet [19] proposed that use of average tube hematocrit instead of feed hematocrit would enable one to ignore the Fahraeus-Lindqvist effect. Their experimental results supported this argument at least down to 29 μm tube diameters.

In tubes smaller than about 500 μm the tube hematocrit is less than the feeding hematocrit or the discharged hematocrit. This is called the Fahraeus effect [20] and can be explained by the presence of a nonuniform RBC distribution and a nonuniform velocity profile across the vessel lumen. When the hematocrit in the central zone is higher than the circumferential zone and the velocity is decreasing from the maximum in the center to zero at the tube wall, the mean residence time of cells will be less than that of plasma. To meet the conservation law, the tube hematocrit must be less than the feed or discharge hematocrit. It should be noted that Fahraeus effect alone should not cause a difference from feed to discharge hematocrit. When the size of the small tube is comparable to that of a cell, a screening effect may cause a difference in measured feed hematocrit and discharged hematocrit. The screening effect is an entrance phenomenon resulting from the fact that near the entrance of a small tube from the reservoir, cells might collide with the edge of the entrance or other cells and are then unable to enter the tube as easily as plasma.

The radial movements of particles in Poiseulle flow has been studied by Goldsmith [21]. In very dilute suspensions deformable red cells migrate radially towards the axis of the tube. As the concentration of the suspension is increased, particle-particle interactions and collisions begin to occur. The red cells deform much more than they do in a dilute solution.

The analysis of particle motion in concentrated suspensions is extremely complex. The radial dispersion of red cells in concentrated suspensions has been studied by tracing red cells in ghost cell suspensions. Self-diffusion coefficients were obtained by measuring the radial displacements of red cells over equal time intervals using the random walk theorem. They ranged from 3×10^{-8} cm^2/sec near the center to 1.5×10^{-7} cm^2/sec close to the wall.

The fact that a cell center can never be located on the tube wall is termed the wall exclusion effect. Together with the tendency of cell migration from the tube wall toward the center, it suggests that a layer of cell free (at least poor) suspending fluid is very likely to exist near the wall. This was first observed by Malpighi in the 17th century. The thickness of the plasma layer has been reported to be about 4-13 μm depending on the hematocrit, in 40 to 70 μm glass tubes [22]. In 100 μm arterioles the thickness were reported to be 3 to 5 μm. Carr [24] computed the thickness to be 4 μm in tubes sized from 20 to 100 μm.

In 1968 Phibbs and Burton [25] measured the radial distribution of red cells in rabbit fermoral arteries with diameters of approximately 1 mm. They used a liquid nitrogen quick freezing technique and found the distribution to be uniform except near the wall. Palmer [26] has studied the red cell distribution across a two dimensional slit channel. The size of the channel was 30 μm. By collecting blood from several transverse positions he found that the red cells do not distribute uniformly across the channel.

The velocity profile is also changed by the presence of concentrated particles. Experiments [21] showed that the velocity profile (based on the particle velocities) is blunt near the axis. The actual profile is influenced by the particle concentration, cell to tube diameter ratio, and flow rate. It was also found that the blunting decreases as the flow rate increases and finally reached parabolic at very high flow rates. Baker and Wayland [2] also concluded that the velocity profile is almost parabolic when $\bar{v}/d$ is greater than 6 sec^{-1}.

All the phenomena described above arise in small vessels where the characteristic dimensions of flow channel and particle approach each other. In other words the continuum concept becomes inappropriate and the particulate nature of blood becomes more important.

1.3 Branching points and bifurcations

With the plasma gap near the wall in mind, imagine a small vessel branching off the main vessel on the side and draining a small amount of fluid from the main channel. It is very likely that the small side branch will contain a larger plasma fraction than the main vessel. This is because the small branching vessel takes fluid away from the cell poor region of the main vessel. Krogh [27] first denoted the term "plasma skimming" for this phase separation phenomenon, separation of the suspending medium, plasma and the suspended particles, red cells. He observed a reduction of hematocrit when there was a reduction in flow in the small side branch. Since then plasma skimming has been the subject of numerous studies both *in vivo* and *in vitro* [23,26,28,29,30,31,32,33].

By occluding vessels downstream from branch points Svanes and Zweifach [34] found that the changes in arteriolar hematocrits depend on the flow fraction split into the side branch. Johnson [35] and Johnson *et al.* [36] used optical opacity as an index of the hematocrits at capillary bifurcations in mesentery. They found that the hematocrits of daughter branches are determined by the cell velocities in each branch. *In vitro* experiments concerning plasma skimming have been conducted either by perfusing blood suspensions through small channels, or by using scaled-up models to simulate the blood flow in small vessels both kinematically and dynamically. Yen and Fung [29] used a scaled up model with gelatin pellets suspended in silicon fluid. The flow had very low Reynolds numbers (10^{-2}–10^{-3}) so the branching angle was considered unimportant. They found that in bifurcations with same size branches, the branch with higher velocity would have more cells. Also a critical flow was observed and found to be dependent on the feed hematocrit and the particle/tube size ratio. Palmer [26] used a blood suspension flowing through a tiny (30 μm) two dimensional slit channel. He found a nonuniform hematocrit profile across the slit which should be responsible for the plasma skimming. Dellimore *et al.* [33] used human blood perfused through a cylindrical tube bifurcation of 180 μm diameter. They observed plasma skimming by plotting fractional cell flux versus fractional volumetric flow of a side branch. Fenton *et al.* [37] used different preparations of blood suspensions perfused through

equal-sized-branch bifurcations with sizes ranging from 20 to 100 μm. They concluded that at least three factors are important in bifurcation plasma skimming: feed hematocrit, tube size and flow rate distribution. In addition to the separation of plasma and red cells, recently the issue of plasma platelet separation at junctions has received attention [38].

In spite of so much work having been done on plasma skimming and the factors that affect it, most studies are confined to single bifurcations and assume axisymmetric characteristics as the blood approaches the bifurcation. The problems of plasma skimming when bifurcations in series are considered may be an important issue.

The idea that plasma skimming occurs at a bifurcation strongly suggests that, due to the flow disturbance of the side branch, the red cell concentration profile across the lumen is skewed after a bifurcation. Apparently two parameters affect the extent of asymmetry: one is the amount of flow withdrawn by the side branch (magnitude of the disturbance), and the other is the shape of the streamtube (shape of the separating surface) which goes into the side branch. The term separating surface is defined as the boundary surface which divides the flow into two parts, each part flowing to different branches downstream of the bifurcation. If this skewed red cell concentration profile is carried to the next junction before it is fully rearranged, then the amount of plasma skimming of the second bifurcation will be different from the first one. In such a case the hematocrit profile prior to the bifurcation is an important variable in determining the amount of plasma skimming. Several studies [21,39] suggest that this rearranging process could be relatively slow and would result in a considerably non-axisymmetric hematocrit profile when the second junction is reached.

1.4 Synopsis of this study

The flow behavior of blood at a branching site is examined in this study by conducting a scaled-up dye experiment. Separating surfaces for T-type branch junctions are quantified. Mapping techniques of upstream flow to a downstream location of a bifurcation are presented and verified by the dye experiment. The rearrangement of RBC between bifurcations in series is modeled by a dispersion process. A model mathematical equation describing this

rearrangement process is solved using numerical techniques to obtain RBC concentration profiles at each axial location. Dispersion coefficients are estimated by comparing *in vitro* experimental data obtained for 50 μm bore tubes and calculated results. These mathematical models are then applied to compute hematocrit distributions in a simple network.

Chapter 2

Models of Plasma Skimming

The amount of plasma skimming at a single bifurcation is demonstrated by plotting F* versus Q*, which is usually called a flux-flow curve for simplicity. F* is the volumetric fraction of cells entering one daughter branch and Q* is the volumetric fraction of flow entering the same side branch. In the case that the RBCs are evenly distributed across the parent vessel lumen, there will be no phase separation (no plasma skimming) at the junction and the resulting flux-flow curve for such a single bifurcation is the identity line. Thus the extent of plasma skimming can be quantified by the deviation of the flux-flow curve from the identity line. Another important issue worth addressing is that in two-dimensional (slit) flow, symmetric velocity and RBC profiles result in a symmetric flux-flow curve about the point (Q*=0.5, F*=0.5), this is not necessarily true in three dimensional flow (tube flow for example). This is due to an additional degree of freedom in three dimensions, the shape of separating surface. But the mirror image of a flux-flow curve for one daughter branch through the point (0.5, 0.5) is always the flux-flow curve for the other daughter branch.

Sometimes the hematocrit ratio plot is used in interpreting plasma skimming. In these plots the ratio F*/Q* is plotted against Q* of a branch. Physically F*/Q* represents the ratio of side to parent discharge hematocrit. Not only is the discharged hematocrit ratio directly read from this kind of plot, the differences between such curves are also magnified which are usually small and hard to detect in a flux-flow curve.

If one assumes that each particle (RBC) follows a fluid streamline through the junction, as was done throughout this study, then three determining factors for plasma skimming in a bifurcation are identified : the RBC concentration profile (including the width of the

cell-free gap if there is one), the velocity profile and the shape of separating surface.

2.1 Velocity and hematocrit profiles

As mentioned in the previous chapter, the velocity profile of a red cell suspension in tubes can vary from blunt to parabolic depending on the flow rate [6]. Three different profiles will be examined in this study. The flat (uniform) and parabolic profiles were used to mimic the two extremes at lower and higher flow rates. The 2-phase velocity profile considered takes into account the existance of two layers of fluid with different viscosities, one is the cell-rich core phase and the other is the cell-free plasma gap phase. Taking the average velocity, $\bar{v}$ as the characteristic velocity and defining the dimensionless radial coordinate as $\xi = r/R$ where R is the tube radius and r is the radial coordinate , these velocity profiles can be expressed in the following dimensionless forms,

- flat

$$V(\xi) = \frac{v(\xi)}{\bar{v}} = 1 \tag{2.1}$$

- parabolic

$$V(\xi) = 2(1 - \xi^2) \tag{2.2}$$

- 2-phase

$$V(\xi) = \frac{v(\xi)}{K\bar{v}} = \begin{cases} (1-\xi^2)\phi & 1-G < \xi < 1 \quad \text{gap phase} \\ (1-G)^2 + [1-(1-G)^2]\phi - \xi^2 & 0 < \xi < 1-G \quad \text{core phase} \end{cases} \tag{2.3}$$

where normalized plasma gap width $G = g/R$,

$$K = [(1-G)^2(A-\phi) + \frac{(1-G)^4}{2}(\phi - 1) + \frac{\phi}{2}]^{-1},$$

$$A = (1-G)^2 + [1-(1-G)^2]\phi,$$

and ϕ is the viscosity ratio of the core and gap. Barbee [40] proposed a correlation for ϕ and core hematocrit. Given the feed hematocrit and gap width the viscosity ratio is found from the Barbee correlation through the law of conservation.

The form of the hematocrit profiles used is either uniform or parabolic core hematocrit.

- Uniform

$$H(\xi) = \begin{cases} 0 & 1-G < \xi < 1 \quad \text{gap phase} \\ H_c & 0 < \xi < 1-G \quad \text{core phase} \end{cases} \tag{2.4}$$

- Parabolic

$$H(\xi) = \begin{cases} 0 & 1-G < \xi < 1 \quad \text{gap phase} \\ H_{\max}[(1-G)^2 - \xi^2] & 0 < \xi < 1-G \quad \text{core phase} \end{cases} \tag{2.5}$$

2.2 Cell-free gap width

The idea of a cell-free plasma gap implies that there will be no cells going into the side branch when the disturbance coming from side branch withdrawal is not significant enough to penetrate into the core zone. In some sense, this is similar to the phenomenon frequently observed in capillaries of *in vivo* experiments [29,41] in that a threshold (critical) flow is required to have cells present in a side branch. Using a 2-phase velocity profile and planar (flat) separating surface Carr [24] calculated the cell free plasma gap width and suggested that a 4 μm gap width is adequate for equal sized T-branches ranging from 20 to 100 μm, and 20% to 40% feed hematocrit. He also concluded from his experiment that cell deformability has negligible influence on gap width. The same plasma skimming data was used in this study to calculate the best fit plasma gap width when substituting a flat velocity profile. The results showed that a layer of 2 μm fit the 50 μm diameter data the best.

2.3 Separating surfaces

Various shapes of separating surfaces have been reported. The shape of separating surface is influenced by flow splits, branching angle, ratio of branch sizes, feed hematocrit and flow rate. Based on our experimental results presented in Chapter 4, two kinds of separating surfaces are selected for discussion in this section, flat and arc shaped. Flat surfaces have been used by several investigators [41,42]. As shown in Figure 2-1 the flat surface is determined by one parameter, the perpendicular displacement of the surface from the tube

center, s. When the bifurcation has geometrically symmetric branches and equal flow splits, the separating surface will be located at the center plane. The arc surface, bulging away from the side branch opening, is always assumed to be centered at the tube wall and also determined by only one parameter [38], the radius of the arc, r_a, in these modeling studies.

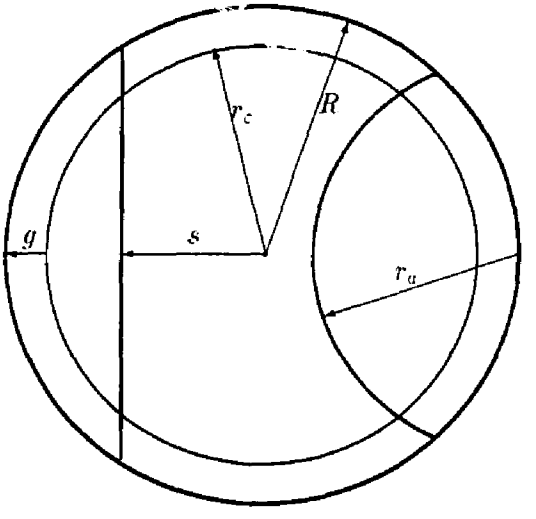

Figure 2-1: Flat and curved (arc) separating surface.

The flux-flow curves are obtained by integrating flow and flux in the flow region A, bounded by separating surfaces and the tube wall:

$$Q^* = \frac{\int_A v(r)\,dA}{2\pi \int_0^R v(r)\,r\,dr} \tag{2.6}$$

$$F^* = \frac{\int_A v(r)\,H(r)\,dA}{2\pi \int_0^R v(r)\,H(r)\,r\,dr}, \tag{2.7}$$

Using a 2-phase velocity profile Fenton *et al.* [37] calculated the Q* and F* for flat separating surfaces, Perkkio and Keskinen [43] have presented the forms for arc surfaces.

A simple parabolic velocity profile, uniform RBC distribution in the core and a cell free gap width, g were assumed for this study. (These are generally assumed in the calculations that follow except when specified.) By introducing following normalized dimensionless

variables.

$$S = s/R, \qquad \text{and}$$

$$R_c = r_c/R = (R - g)/R = (1 - G)$$

Q* and F* for flat and arc separating surface are calculated as following.

- Flat surfaces

$$Q^* = 1 + \frac{2S\sin^3(\cos^{-1} S)}{3\pi} + \frac{S\sin(\cos^{-1} S) - \cos^{-1} S)}{\pi} \tag{2.8}$$

$$F^* = [\frac{\pi}{2} + \theta + \frac{S}{R_c}\cos\theta + R_c S\cos\theta(\frac{\cos^3\theta}{3} - \frac{1}{2}) - \frac{R_c^2}{2}(\theta + \pi)]/\pi(1 - \frac{R_c^2}{2}) \tag{2.9}$$

for $-R_c < S < R_c$ and $\theta = \sin^{-1}\frac{S}{R_c}$.

- Arc surfaces

$$\begin{aligned} Q^* = {} & \frac{4(2 - R_a^2/4)R_a^3\cos^3\theta_1}{3\pi} - \pi R_a^4(\theta_1 - \frac{R_a\cos\theta_1}{2}) - \frac{R_a^4}{2} + \frac{1}{2} \\ & -\frac{1}{3\pi}\{(2 - R_a^2)\cos^3\theta_2 + 3[\theta_2 + (1 - \frac{R_a^2}{2})\cos\theta_2]\} \end{aligned} \tag{2.10}$$

where R_a is the dimensionless arc radius, $R_a = r_a/R$ and

$$\theta_1 = \sin^{-1}\frac{-R_a}{2}, \qquad \theta_2 = \sin^{-1}(1 - \frac{R_a^2}{2}).$$

For $G < R_a < (G + 2)$

$$\begin{aligned} F^* = {} & \{[\frac{3 + (R_c^2 - R_a^2 + 1)/2}{3}](R_a\cos\theta_3)^3 - \frac{R_a^4}{2}[\theta_3 + \frac{(R_c^2 - R_a^2 - 1)\cos\theta_3}{2R_a}] \\ & -\frac{\pi R_a^4}{4} + R_c(1 - \frac{R_c^2}{2})[\frac{\pi}{2} - \theta_4 - \frac{(R_c^2 - R_a^2 + 1)\cos\theta_4}{2R_c}] \\ & -\frac{(R_c^2 - R_a^2 + 1)R_c^3\cos^3\theta_4}{6}\}/[\pi R_a^2(1 - \frac{R_a^2}{2})] \end{aligned} \tag{2.11}$$

where

$$\theta_3 = \sin^{-1}\frac{R_c^2 - R_a^2 - 1}{2R_a}, \qquad \theta_4 = \sin^{-1}\frac{R_c^2 - R_a^2 + 1}{2R_c}.$$

For demonstration, a calculated flux-flow plot for flat and arc separating surfaces is shown in Figure 2-2. The solid curve represents the calculation results based on the flat separation surface and the broken curve on the arc surface. Using 4μm as the gap width in a 20 μm diameter tube, this plot shows the effect of the shape of separation surfaces on plasma skimming.

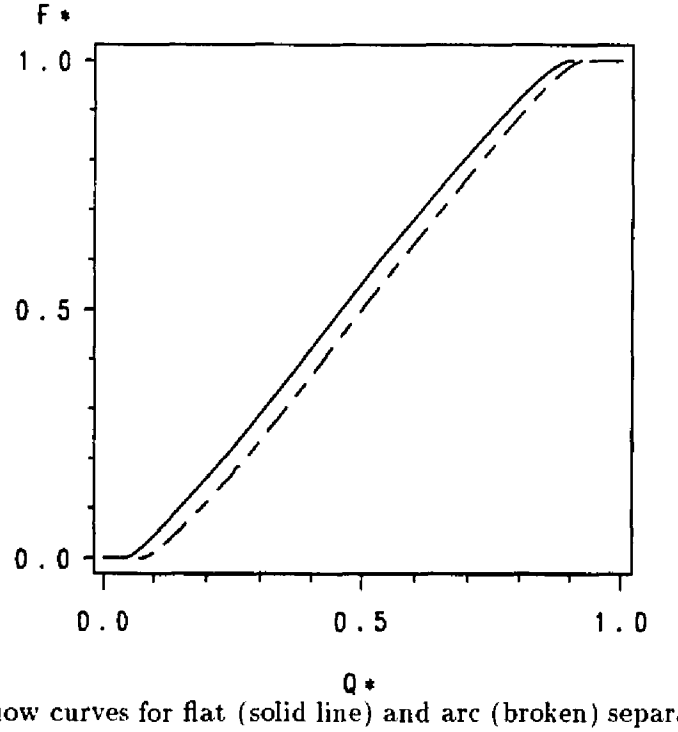

Figure 2-2: Flux-flow curves for flat (solid line) and arc (broken) separating surfaces

Sometimes these S-shaped curves are represented by a logit function to correlate experimental data [33,8.44].

$$\text{Logit}(F^*) = a + b\text{Logit}(Q^*) \tag{2.12}$$

where $\text{Logit}(x) = \ln[(1-x)/x]$. The parameter a determines the asymmetry of the cell distribution between the branches, while b characterizes the shape of the curve. Since a flat separating surface with axisymmetric profiles results in a symmetric flux-flow curve with respect to point (0.5,0.5), the corresponding Logit function fit should have parameter a

vanish. As far as the critical flow is concerned, according to Pries *et al.* [44], the Q* is further substituted by $0.5 - \frac{0.5}{0.5-X_0}(0.5 - Q^*)$, in which X_0 is the critical flow fraction. The no cell flux requirement when Q* is X_0 and $1 - X_0$ is thus satisfied. But this substitution does not allow different critical flows at different ends of the flux-flow plot, which exists when curved separating surfaces are used.

If the plasma gap remains at 4 μm the magnitude of the dimensionless gap width will change as the size of the vessel changes. Obviously as the vessel size increases the plasma gap becomes relatively less important. However when the factor of the shape of separating surface exerts its influence the net effect is not so clear. It is asked if there is a range of vessel sizes in which the choice of the separating surface makes little difference as far as plasma skimming is concerned. A plot of the differences between computed flux-flow curves versus vessel sizes was thus created. The area between two flux-flow curves is used to quantify the difference. The plot is shown in Figure 2-3.

Surprisingly, this plot suggests that the shape of separating surface is irrelavent to the plasma skimming when the parent vessel is larger than about 30 μm in diameter. The choice of separating surface makes a drastic difference when the vessel size is less than 30 μm.

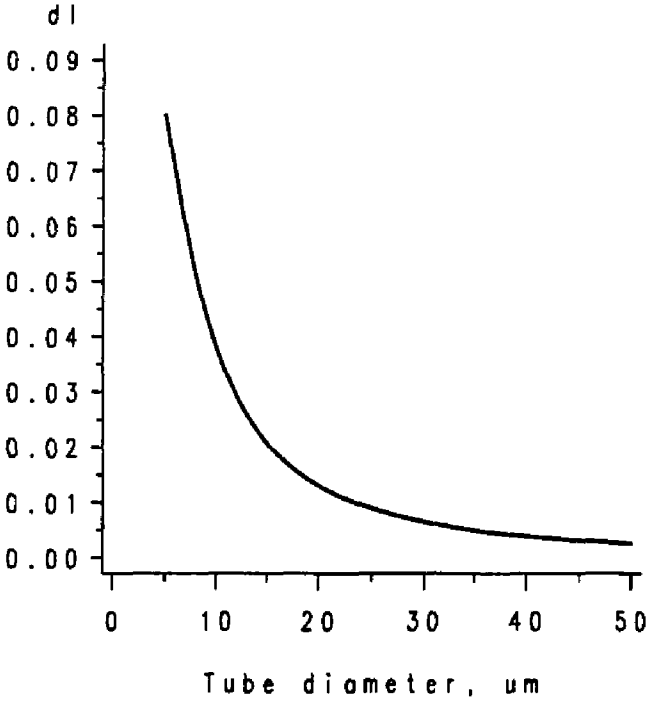

Figure 2-3: Difference in plasma skimming for flat and arc separation surfaces versus tube size.

Chapter 3

Problems of Serial Bifurcations

Though the phase separation is tiny for vessels larger than capillaries (about 20-70 μm [45]), it could be accentuated if a series of bifurcations is encountered. In addition to the problem of plasma skimming at a branching point, the process which takes place in the vessel segment between junctions has to be evaluated if bifurcations in series are considered. The streamlines bend while the blood flows through the junction. By assuming the red cells follow the streamlines [41,24,17,37,43], the cell distribution downstream of the junction is no longer axisymmetric, nor is the velocity profile.

The velocity profile corrects itself through hydrodynamic processes. This hydrodynamic entrance length is usually short compared to the diffusional entrance length. This can be checked by comparing the suspension kinematic viscosity and the red cell diffusivity. A preliminary test from the RBC self-diffusion coefficient derived by Goldsmith [21] shows little question about this statement. Experimentally Levine and Goldsmith [46] showed that the velocity profiles developed mostly within one to two diameters in a diverging Y-bifurcation. Because the viscosity and hematocrit are interrelated, strictly speaking the velocity profile shall not be symmetric until the concentration profile is fully developed (symmetric). In this study it is assumed that the velocity profile recovers from the disturbance in a short distance (compared to the hematocrit recovery length) and remains unchanged throughout the red cell rearranging process. The corrections due to viscosity changes are neglected.

As blood flows between junctions, the hematocrit profile regains symmetry. It is suspected that this is because red cells migrate across streamlines. The driving force of red cell movement across suspension streamlines exists for the following reasons:

- The famous Segré-Silberberg effect [47,48] (or tubular pinch effect), which indicates the existence of inertia-induced radial migration of an isolated neutrally buoyant rigid particle toward an equilibrium position in shear flow. For deformable particles Goldsmith [21] showed that the equilibrium position is at the tube axis even at negligible fluid inertia. In these conditions the rigid particles do not migrate in either direction due to the kinematic reversibility of the flow.

- Shear-induced interactions among neighboring particles in concentrated suspensions (particle collisions), first postulated by Thomas *et al.* [49]. Each particle in shear flow rotates and creates a local velocity field around it. In concentrated suspensions this field influences the neighboring particles and each particle is influenced by the fields created by its neighboring particles. Also, particles travel at different velocities in shear flow, and frequent collisions, not necessary physical contacts, occur among neighboring particles. Particle lateral movements do occur when many particles are involved in this process [50]. Eckstein [51] proposed that when many particles are involved the particle lateral migration is caused by continuous inputs from successive randomly arranged surounding particles. This particle migration process exhibits stochastic behavior associated with random-walk processes. Thus it is plausible to quantify this process by Fick's law of diffusion in terms of a coefficient of self-diffusion. Goldsmith [21] analyzed the random radial displacements of red cells as similar to Brownian motion and measured the self-dispersion coefficient in red cell suspensions with hematocrit of 0.39.

- The tendency of forming a concentric configuration when two immiscible fluids with different viscosities are flowing in a circular pipe, with the thinner fluid encapsulating the thicker fluid. This has been observed experimentally [52,53] and explained theoretically by minimum viscous dissipation. Joseph [54] showed that the viscous dissipation principle is not always true though, the lubrication flow of the thinner fluid encapsulating the thicker fluid is stable as long as the fractional core radius is greater than 0.7. The entrance length of this encapsulation process has been studied

experimentally. The most similar system to the plasma/red cell suspension studied was the xylene/sucrose solution system. Its entrance length was approximately 1 vessel diameter [55].

The high red cell concentration (about 40% to 45% in volume) in the circulatory system probably favors the particle collision mechanism over the tubular pinch effect. The short distance for developing the lubrication layer in two immiscible phases may not apply to the blood suspension case because of the absence of an immiscible interface in blood flow. Local apparent viscosity varies with the hematocrit profile. Immediately downstream of a junction the hematocrit profile is shifted and a sharp interface between enlarged plasma gap (less viscous phase) and shifted cell-rich core (more viscous phase) could exist momentarily. As soon as this interface starts to move herefrom, according to the minimum viscous dissipation principle [56], a gradual gradient of hematocrit across the original interface develops. Then, the lubricating process should slow down asymptotically. This procedure continues until either the minimum viscous dissipation flow configuration is achieved, or the viscosity difference no longer exists.

It is thus believed that after being disturbed (perhaps by the presence of a side branch), the resulting asymmetric hematocrit profile corrects itself. This rearranging process in a blood vessel is driven by at least two different mechanisms. One is the tendency to form a lubricating layer and the other is the shear-induced diffusional type mechanism resulting from neighboring particles interactions. Apparently, local particle concentration and shear rate in the flow field play important roles in the latter mechanism which is not the same as the ordinary diffusion. In fact the wall interference (depending on the geometric parameters), shear rate gradient, particle related fluid Reynolds number, such as $\rho a^2 \gamma / \mu$, and gravity (if particles are not neutrally buoyant) also effect the "diffusional" radial migration. The intrinsic dispersion coefficient is most probably anisotropic (directional) because the hematocrit and shear rate won't be constant when the cells are rearranging themselves between junctions, and that the wall interference only disappears in very large vessels. In this situation the random walk theory does not apply ideally. To consider all

these factors separately introduces extreme difficulties. It is intented in this study that all these effects be included in a lumped parameter, the effective dispersion coefficient.

In summary, the answer to the problem of red cell distribution at hand is divided into two stages. First, the branching tube flow forces the cell-rich core portion in the parent tube to shift to the intralateral side of the daughter branch, the disturbed velocity profile recovers in a short distance, during which the red cells may migrate across streamlines a little but the major shift is due to the streamline bending. At the same time the wall exclusion and some lubrication effect build up a cell-free plasma gap quickly along the intralateral tube wall. When all this is completed, the initial hematocrit distribution is developed. It is assumed that all these actions are included in an initial shift mechanism. The technique to derive this initial shift is described in Section 3.1. Then, starting from this initial hematocrit profile the red cells rearrange themselves toward a symmetric profile as the bulk flow continues down the vessel. This process is modeled by using a constant effective dispersion coefficient as discussed in Section 3.2.

3.1 Initial shift in hematocrit profile

This section will discuss the shift of the hematocrit profile across the junction at an axial location where the velocity profile is fully developed. This is essential and provides the required initial condition if the subsequent rearrangement process is to be quantified. Streamline tracing of suspending medium was attempted to gain the initial condition. Analytical solution was first attempted but found not feasible. Then a semi-empirical technique was developed to give the initial condition.

3.1.1 Stream function approach

If the streamlines do not cross each other in a slit bifurcation, the mapping of streamlines in a two-dimensional junction is easily accomplished by using the concept of stream functions. The stream function of a two dimensional flow can be derived by integrating velocity with respect to the coordinate across the slit, ξ. By definition the difference between the value

of the stream function for two streamlines is exactly the volumetric flow between these two streamlines. If the integration constant is set to zero then the stream function has value zero at ξ=0. The magnitude of the velocity can be adjusted so that the volumetric flow across the slit is normalized, making the value of the stream function equal to 1 at ξ=1. For Poiseuille flow the upstream stream function ψ is thus

$$\psi(\xi) = 3\xi^2 - 2\xi^3 \tag{3.1}$$

The streamline that separates the flow into two daughter branches must have the value Q* if the flow split designates this fraction of flow to enter the side branch. Being constant along a solid boundary surface, the stream function after the velocity profiles in daughter branches are fully developed must be

$$\psi(\zeta) = Q^*(3\zeta^2 - 2\zeta^3) \tag{3.2}$$

for the branch receiving the flow portion having stream function values less than Q* and

$$\psi(\eta) = (1 - Q^*)(3\eta^2 - 2\eta^3) + Q^* \tag{3.3}$$

for the other branch. The ζ and η represent the dimensionless coordinates across branch slits. The streamline tracing can be achieved by equating values of stream functions to solve for downstream location ζ or η.

The streamline in three dimensions is expressed as the intersection of two families of level surfaces [57]. Similar information, the velocity profiles, the separating surfaces, the mapping of streamlines on the boundary surfaces, are used to simulate the derivation of the 2-D case in order to trace every streamline in three dimension. Unfortunately, the extension of the stream function approach to a three-dimensional flow has not been successful. The outcome is comprehensible that in 2-D flow the bending of streamlines has only one degree of freedom (1 directional) which is easily solved by insisting that the downstream velocity profile satisfy the continuity equation. While in 3-D flow the bending is two-directional. The condition of matching the flow between level surfaces (continuity requirement) alone does not suffice to solve a problem with 2 unknown variables. The force balance equation

(Navier-Stokes equation) must be solved simultaneously to get a solution. Such solutions have not yet been available.

3.1.2 Mapping technique

A mapping technique was proposed to determine the initial hematocrit shift. Initiated from the idea of separating surfaces, this technique assumed that the fluid elements never change their relative positions through the junction. To keep their relative positions in the case of a flat separating surface, every point in the flow field to be mapped is imagined as the intersection of two imaginary flat separating surfaces, chord AD and BF as shown in Figure 3-1: one parallel (chord BF) to the actual separating surface (chord CE) and the other (chord AD) perpendicular to it.

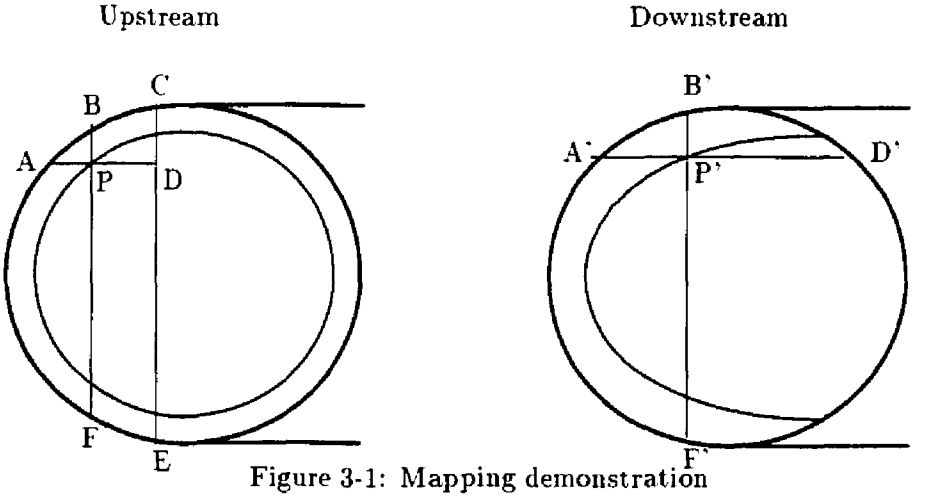

Figure 3-1: Mapping demonstration

One of the ways to maintain relative position after the bifurcation is to require that the flow through area ABCDPA and area ABPFA upstream remain in area A'B'D'P'A' and A'B'P'F'A' downstream respectively. By matching the flow fractions in these regions the locations of chord A'D' and B'F' are determined. The point P' is thus mapped from upstream point P. In this fashion the flow element above point P upstream the junction will never come beneath it after the junction, and the fluid element originally on its left

will remain on its left downstream the junction. With the same idea the straight chords used can be changed to any shape depending on the shape of separating surface. This technique is not only used in mapping the plasma gap boundary, it is also used to shift the upstream hematocrit profiles to downstream when they are not uniform. Depending on the velocity profile used, the evaluation of flow bounded in different shaped regions was done by numerical integration with Simpson's rule. The technique was tested in a dye experiment as described in the next chapter.

3.2 Model equation for cell dispersion between junctions

It is proposed that a dispersion type of process be used to model the cell rearrangement between junctions in a serial bifurcations network. A constant parameter, dispersion coefficient $\mathcal{D}$, is assumed. The mass balance of red cells results in the following convective diffusion equation

$$v \cdot \nabla H = \mathcal{D} \nabla^2 H + \nabla \cdot \vec{m}, \tag{3.4}$$

where v is the velocity, H is the local cells concentration, and $\mathcal{D}$ is the effective particle dispersion coefficient. The $\vec{m}$ is included for generality which is responsible for the driving forces of the Segré-Silberberg effect. The exact form of this vector function is not known. When a cell-free plasma gap is present the domain of Equation 3.4 is confined to the core region in which the cells can be present. The boundary condition near the wall side would be no flux of cells crossing the plasma gap boundary. Mathematically this means a balance between the diffusional flux and $\vec{m}$.

It is assumed that the formation of the plasma gap is due to the exertion of wall stress upon the suspension and established as quickly as the velocity profile regains its symmetry after the disturbance (bifurcation). Thus, in addition to the mapping technique described in the previous section the initial condition of this problem is obtained by also imposing a minimum plasma gap on the inner lateral side of the downstream branch. That is, the mapping techniques apply to the core region only. No cells can ever be mapped into the plasma gap region.

Using the magnitude of RBC self-diffusion coefficient derived by Goldsmith [21], dimensional analysis shows that the dispersion in the axial direction is negligible. It is assumed that the flux vector $\vec{m}$ has only a component in radial direction. For parabolic velocity profile Equation 3.4 can be expressed in cylindrical coordinates as

$$2\bar{v}[1-(\frac{r}{R})^2]\frac{\partial c}{\partial z} = \mathcal{D}[\frac{1}{r}\frac{\partial}{\partial r}(r\frac{\partial c}{\partial r}) + \frac{1}{r^2}\frac{\partial^2 c}{\partial \theta^2}] + \frac{1}{r}\frac{\partial}{\partial r}(rm_r) \tag{3.5}$$

with boundary conditions

$$\begin{cases} -\mathcal{D}\frac{\partial c}{\partial r} = m_r & \text{at} \quad r = R-g \\ c \quad \text{is finite} & \text{at} \quad r = 0 \\ c(r,0,z) = c(r,2\pi,z) & \text{and} \quad \frac{\partial c}{\partial \theta}(r,0,z) = \frac{\partial c}{\partial \theta}(r,2\pi,z) \\ c = c_i(r,\theta) & \text{at} \quad z = 0 \end{cases} \tag{3.6}$$

The asymptotic solution (as $\eta \to \infty$), c_s, must be function of r only. From Equation 3.5 the c_s can be expressed as

$$-\mathcal{D}\frac{\partial c_s}{\partial r} = m_r + \frac{K_1}{r} \tag{3.7}$$

where K_1 is an integration constant. Since c_s is finite at $r = 0$, K_1 must vanish, and the asymptotic solution is determined by the flux vector functin $\vec{m}$. Equation 3.7 is now exactly the same as the first boundary condition in Equation 3.6. Since $c = c_s + c_t$, subtracting the asymptotic solution from the total solution gives the transient solution. The equation and boundary conditions for the transient concentration will always be the same regardless of the asymptotic solution chosen. They are

$$2\bar{v}[1-(\frac{r}{R})^2]\frac{\partial c_t}{\partial z} = \mathcal{D}[\frac{1}{r}\frac{\partial}{\partial r}(r\frac{\partial c_t}{\partial r}) + \frac{1}{r^2}\frac{\partial^2 c_t}{\partial \theta^2}] \tag{3.8}$$

$$\text{B. C.} \quad \begin{cases} \frac{\partial c_t}{\partial r} = 0 & \text{at} \quad r = R-g \\ c_t \quad \text{is finite} & \text{at} \quad r = 0 \\ c_t(r,0,z) = c_t(r,2\pi,z) & \text{and} \quad \frac{\partial c_t}{\partial \theta}(r,0,z) = \frac{\partial c_t}{\partial \theta}(r,2\pi,z) \\ c_t = c_{ti}(r,\theta) & \text{at} \quad z = 0 \end{cases} \tag{3.9}$$

The asymptotic solution is affected only by m_r.

By introducing proper dimensionless variables Equation 3.8 is non-dimensionalize to

$$(1-\xi^2)\frac{\partial C}{\partial \eta} = \frac{1}{\mathrm{Pe}}\left(\frac{\partial^2 C}{\partial \xi^2} + \frac{1}{\xi}\frac{\partial C}{\partial \xi} + \frac{1}{\xi^2}\frac{\partial^2 C}{\partial \theta^2}\right) \tag{3.10}$$

$$\text{B. C.} \quad \begin{cases} \frac{\partial C}{\partial \xi} = 0 & \text{at} \quad \xi = 1 - G \\ C \quad \text{is finite} & \text{at} \quad \xi = 0 \\ C(\xi, 0, \eta) = C(\xi, 2\pi, \eta) & \text{and} \quad \frac{\partial C}{\partial \theta}(\xi, 0, \eta) = \frac{\partial C}{\partial \theta}(\xi, 2\pi, \eta) \\ C = C_i(\xi, \theta) & \text{at} \quad \eta = 0 \end{cases} \tag{3.11}$$

where

$$\xi = \frac{r}{R}, \qquad \eta = \frac{z}{R}$$

$$C = \frac{c_t}{c_r}, \qquad \mathrm{Pe} = \frac{2\bar{v}R}{\mathcal{D}}$$

and c_r is any reference concentration. Similarly if a uniform velocity profile is substituted in place of the parabolic velocity profile, the dimensionless form becomes

$$\frac{\partial C}{\partial \eta} = \frac{2}{\mathrm{Pe}}\left(\frac{\partial^2 C}{\partial \xi^2} + \frac{1}{\xi}\frac{\partial C}{\partial \xi} + \frac{1}{\xi^2}\frac{\partial^2 C}{\partial \theta^2}\right) \tag{3.12}$$

with the same boundary conditions shown in Equation 3.11.

In this study, two asymptotic solution will be specified. One is a flat concentration profile which will eliminate the last term in Equation 3.4. Actually in such case the m_r in Equation 3.7 becomes zero. The other asymptotic solution used will be a parabolic profile with zero concentration on the outside boundary. The parabolic profile results if m_r is a linear function of r. Numerical methods and solutions for Equation 3.10 and 3.11 are demonstrated in Chapter 5.

Chapter 4

Experiments to Determine Separating Surfaces and Mapping

Flow through branching tubes or bifurcations was examined by scaled-up dye experiments. Bifurcations with T-type configuration were studied. A T-type bifurcation is a straight parent tube with another straight side branch extending out perpendicularly from it. For clarity the feeding segment is designated as the parent branch. The other two vessels are defined as daughter branches with one called the side branch, and the other the continuing branch. It was suspected that the daughter to parent branch size ratios (Db/Dp) and the flow splits determine the shapes of separation surfaces. The branching angle is thought to be have little effect at low Reynolds numbers. Separating surfaces of two different size ratios at various fractional flow off the side branch were obtained. Streamline tracing (mapping) through the bifurcation was also accomplished in this experiment to test the mathematical mapping technique presented in the previous chapter.

4.1 Materials and methods

The major experimental apparatus is illustrated in Figure 4-1. The bifurcation is fabricated by drilling a hole through a Lucite block as the parent tube. Another hole is drilled from the side edge untill the parent tube is reached and connected, forming the side branch. The inside wall of these holes are reamed to obtain the desired bore size, and polished so the dye stream can be seen clearly from the outside.

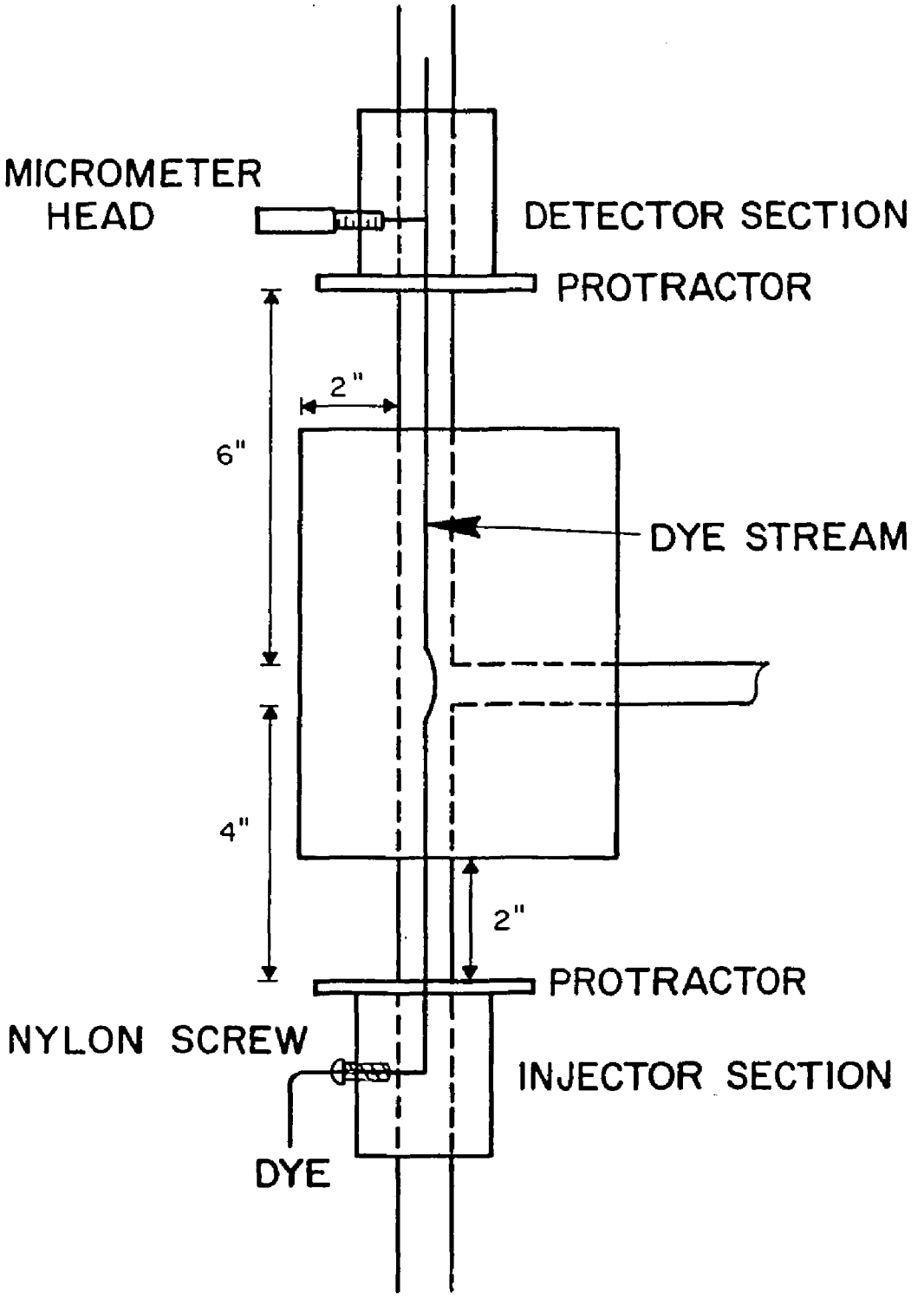

Figure 4-1: Apparatus of the dye experiment

Two similar blocks were built: one has a 0.5-in diameter parent tube and a 0.5-in side branch (Db/Dp=1); the other has the same sized parent tube but half sized (0.25-in) side branch (Db/Dp=1/2). No extra work was done to the rims connecting parent branch and side branch, they remained sharp edged. Three extension plexiglass tubes were mounted firmly to the block at each end of the branches with Teflon tape to prevent leakage. At the feeding end of the plexiglass tube an injector section was connected. The injector section consists of a cylindrical block with a 0.5-in. hole drilled along its axis, a protractor mounted to the cylindrical block, a dye injection needle penetrating through a nylon screw is mounted on the side of the cylinder as shown in Figure 4-1. The nylon screw can be turned in or out of the cylindrical block to adjust the radial location of the injection needle tip in the upstream flow field. At the joint of the injector section and the feeding tube leading to the bifurcation block, two O-rings were fit into slits to serve as leakage sealant and still enable rotation of the whole injector section with respect to the bifurcation block. The displacement of the needle tip from the tube wall was obtained by measuring the external length of the nylon screw using a dial caliper. The angular location was adjusted by rotating the whole injector section. With the help of the protractor the angular displacement was read from a reference position, which consists of a stationary thread with a hanging weight to remain vertical. A similar device, the detector section, is connected to the continuing branch. However, a micrometer head with a sewing needle was mounted on the detector instead of the nylon screw used in the injection section. The radial locaton of the needle tip detecting the dye stream was read directly from the micrometer.

As shown in Figure 4-2, flow is gravity driven by maintaining a constant level difference between feeding and draining reservoirs. Flow fractions of the two daughter branches are controlled by two valves and monitored through two identical rotameters. In order to have low Reynolds number flow (Re $<$ 1) without decreasing the velocity too much, a concentrated (about 60 wt%) sugar solution was prepared and used as the major working fluid for its high viscosity. Tap water served as another working fluid for higher Reynolds numbers. The injected dye solution was prepared by mixing red food coloring with isopropyl

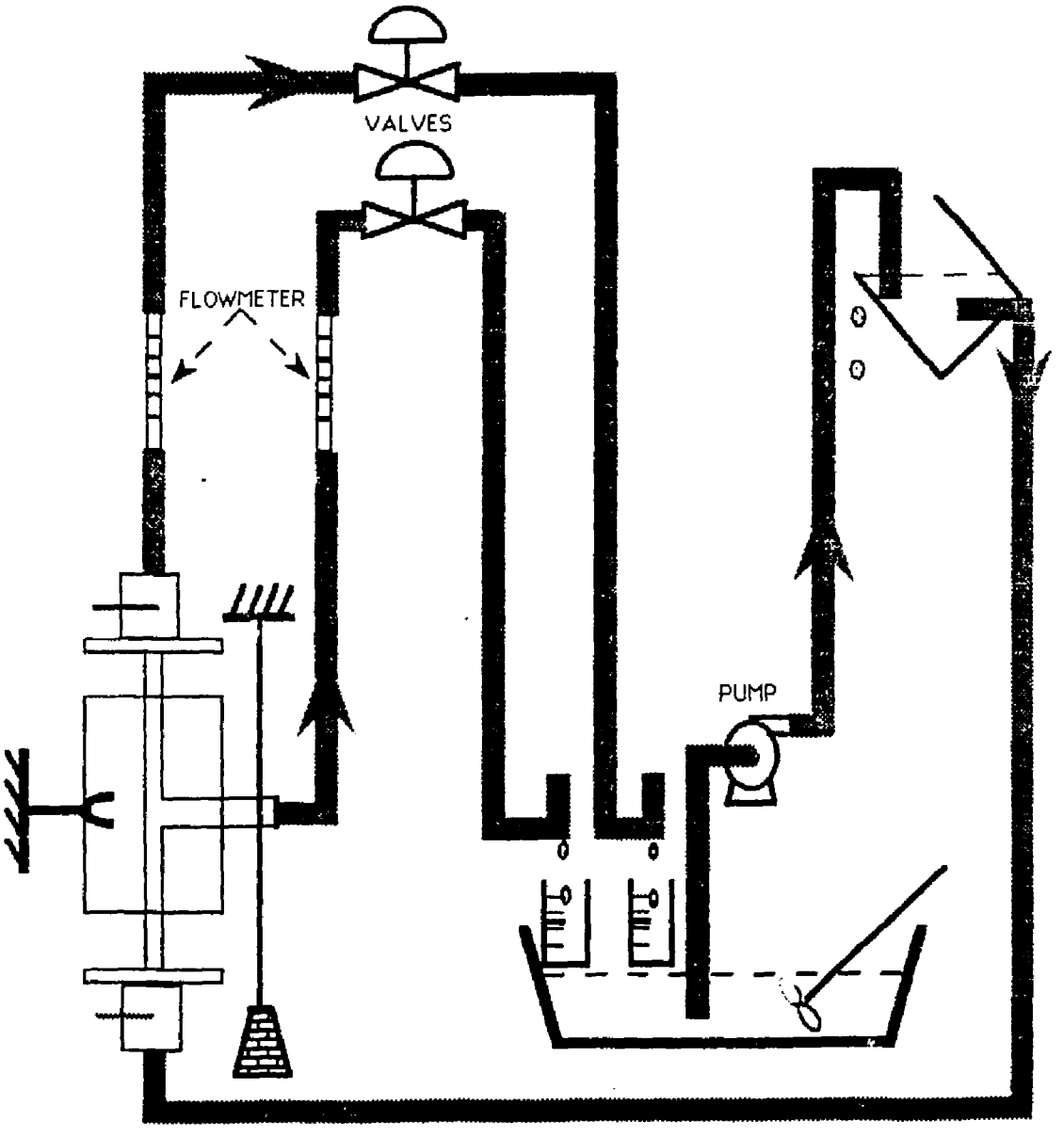

Figure 4-2: Experimental setup.

alcohol or sugar solution to adjust its density so that the buoyancy effects are minimized. Meanwhile the device is set up vertically to decrease these effects. It was visually observed that the dye filament did not flow straight up from the injection needle tip, instead it bent back slightly along the length of the needle before rising vertically. Thus, there is deviation between the needle tip and the actual dye stream locations. This bending depends on the local velocity near the needle tip. Correlation of the injection needle position and the dye location was used to correct this effect. The correlation was obtained by running fluid through a section of straight tube instead of a bifurcation block. Length measurements of the nylon screw represented the needle tip's radial location while the dye stream's position was determined by the micrometer needle tip in the detector section.

The Reynolds number in the parent branch is checked by measuring flow rate and viscosity before and after each run. Flow rate is measured by collecting fluid (about 25 ml) and the viscosity is measured by a cone and plate viscometer (Brookfield RVT).

The separating surface is found by moving the location of the injection needle tip until the dye filament was equally split at the rim of the junction. Initially the experiments were conducted by running water through the model. The entering Reynolds numbers in the parent branch were about 167. At these Reynolds numbers vortices were observed near the junction which agreed with the results reported by Karino *et al.* [58]. Sugar solution was then introduced to decrease the Reynolds number so the vortices were avoided. Separating surfaces for three branching configurations have been obtained: same size branches (0.5 in.–0.5 in.) with side-branch-type jucntion; same size branches with the side branch as the feeding vessel; and half size (0.5 in.–0.25 in.) side-branch-type junction.

The mapping of flow element through the junction is done by setting an upstream dye filament location then detecting its downstream location. Similar to the injection needle, the dye stream bends as it approaches the detection needle. The detection is accomplished by moving the detection needle tip until two criteria are met: first, the dye filament and the tip are visually superimposed angularly; second, the needle tip is radially located at the imaginary dye stream continuation line, which is the line connecting the upstream dye

stream and downstream needle tip.

Data points at upstream circles, 20° apart from each other were mapped to their downstream locations for several different flow splits.

4.2 Results

Figures 4-3, 4-4, 4-5 show the results of the separating surfaces at low Reynolds numbers (less than 1). The numbers associated with each set of data represent the flow fraction, Q* off the side branch. Figure 4-3 shows the flat separating surfaces when the branches have the same diameters (0.5in.-0.5in.). Slight curvature appears as Q* deviates from one half. It is also suspected that the curvature is present near the tube wall although this is not clearly shown in the figure. The results when using the side branch as the feeding branch are shown in Figure 4-4. Again a flat separating surface is obtained for this flow arrangement. Figure 4-5 shows the results when the side branch is half the size of the parent branch. The separating surfaces are curved, bulging away from the opening of the side branch. The solid curves shown in Figure 4-5 are arcs centered at the tube wall. By varying only one parameter, the radius, these arcs fit the data satisfactorily.

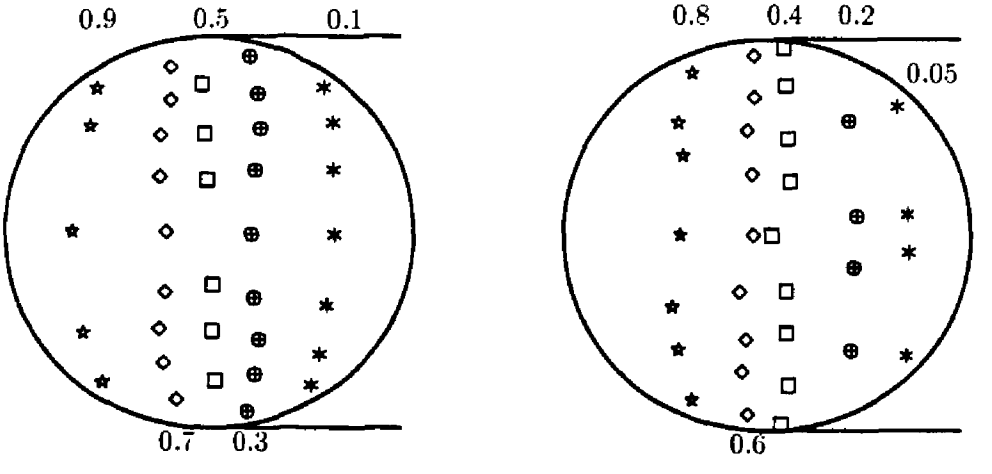

Figure 4-3: Separating surfaces for side-branch-type junction.

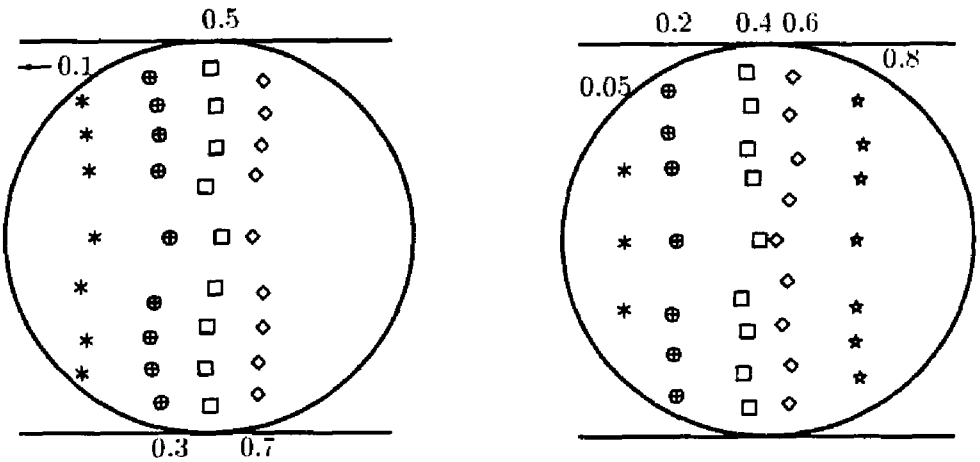

Figure 4-4: Separating surfaces for T-type junction.

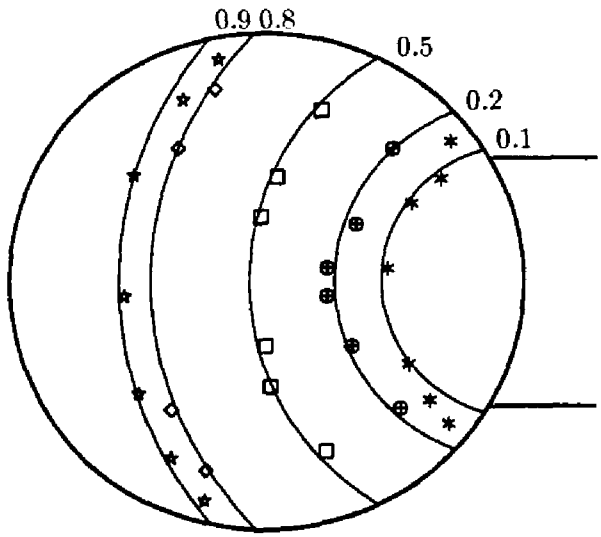

Figure 4-5: Separating surfaces for side branch junction with unequal diameters.

The results obtained by running water at higher Reynolds numbers (about 167) are shown in Figure 4-6. Vortices were seen in these experiments. When a dye stream enters a vortex it is very likely that it spread itself to a broader stream then diverge into more than one stream in the vortex. Very often these branched dye streams end up in different branch tubes and the flow becomes very complicated. The data points shown in Figure 4-6 are those injection positions where injected dye did not enter a vortex.

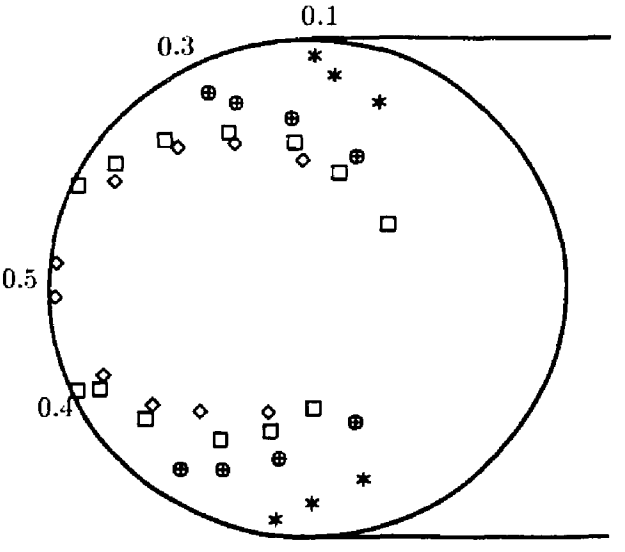

Figure 4-6: Separating surfaces at high Reynolds number.

Figure 4-7 shows previous work done on separating surfaces [60,59,61,31,17]. Among the three crescent shaped separating surfaces with bulges toward the side branch opening. Pinchak and Ostrach reported the Reynolds number to be 500, Øfjord and Clausen reported 600, Stoltz *et al.* did not report flow rates or Reynolds numbers. It is suspected that in such high Reynolds numbers vortex formation seems to be unavoidable in most flow splits [58]. This shape of separating surface is believed to exist only when the side branch flow fraction is small and during which the major vortex is absent.

The double-humped shape reported by Deakin and Blest is peculiar. It has been brought to the author's attention that attempts to locate the absolute position of the injection needle

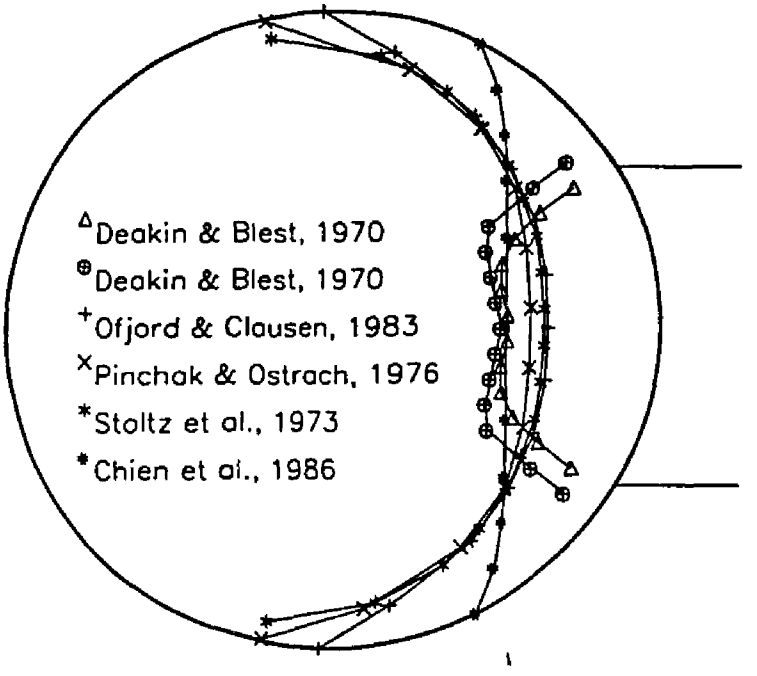

Figure 4-7: The shape of separating surfaces previously obtained.

tip is difficult due to the offset imbedded in the device when it was fabricated. For this reason the separating surfaces shown in this dissertation were all obtained by full range measurement (that is, every point in the flow field shown was actually measured), then about ten degrees of rotation was needed to bring the pictures of surfaces to symmetry. Deakin and Blest only measured one half of the flow field and completed the whole figure by folding the data points through the half plane of assumed symmetry. If the side branch opening has not been located precisely with respect to the data points, the half plane used for flipping over would not be correct and a double-hump can easily result. It is thus suspected that if a full range measurement was conducted instead of folding over, the double-humped image could be avoided. Also the close proximity of the bifurcation and mapping site (about three quarters of a diameter) could cause problems [24]. Chien *et al.* studied the separating surface for the same sized T-junctions with the side branch as the feeding branch. A much greater range of Q^* was examined in their study. At Reynolds numbers ranging from 0.1 to 0.01, a nearly flat shape is reported.

The experimental results of streamline tracing through the junction are shown in Figure 4-8. The fractional circle in each plot is the upstream ring to be mapped (the portion not shown is withdrawn into the side branch). The broken line represents the computational result based on the mapping technique described in the previous chapter. In the case where the side branch has the same size as the parent branch (a, b, c), flat separating surfaces were used to compute the downstream mapping. For the half size side branch (d, e, f) the actual separating surface is curved. The calculation was based on the best fitted arc separating surfaces as the actual separating surface. For simplicity, every point upstream is still defined by two perpendicular chords, similar to the same size side branch case. The fractional flow into the side branch in each plot is : (a), 18%; (b), 50%; (c), 70%; (d), 50%; (e), 82%; (f), 18%. The agreement between the computation and the measurements is quite good. Only when the upstream ring gets close to the tube wall does the computation not agree with measurements as well, especially in the case of half size side branch. Figure 4-9 shows the worst case obtained.

Figures 4-10 and 4-11 show the domains in which the mapping technique works satisfatorily. The curves on the top of each plot is the boundary of possible flow fraction and upstream radius. Above the curve all the streamlines on the ring bend into the side branch. In these plots a circled dot represents satisfactory matches between calculation and experiment, a cross means the agreement is less than satisfactory.

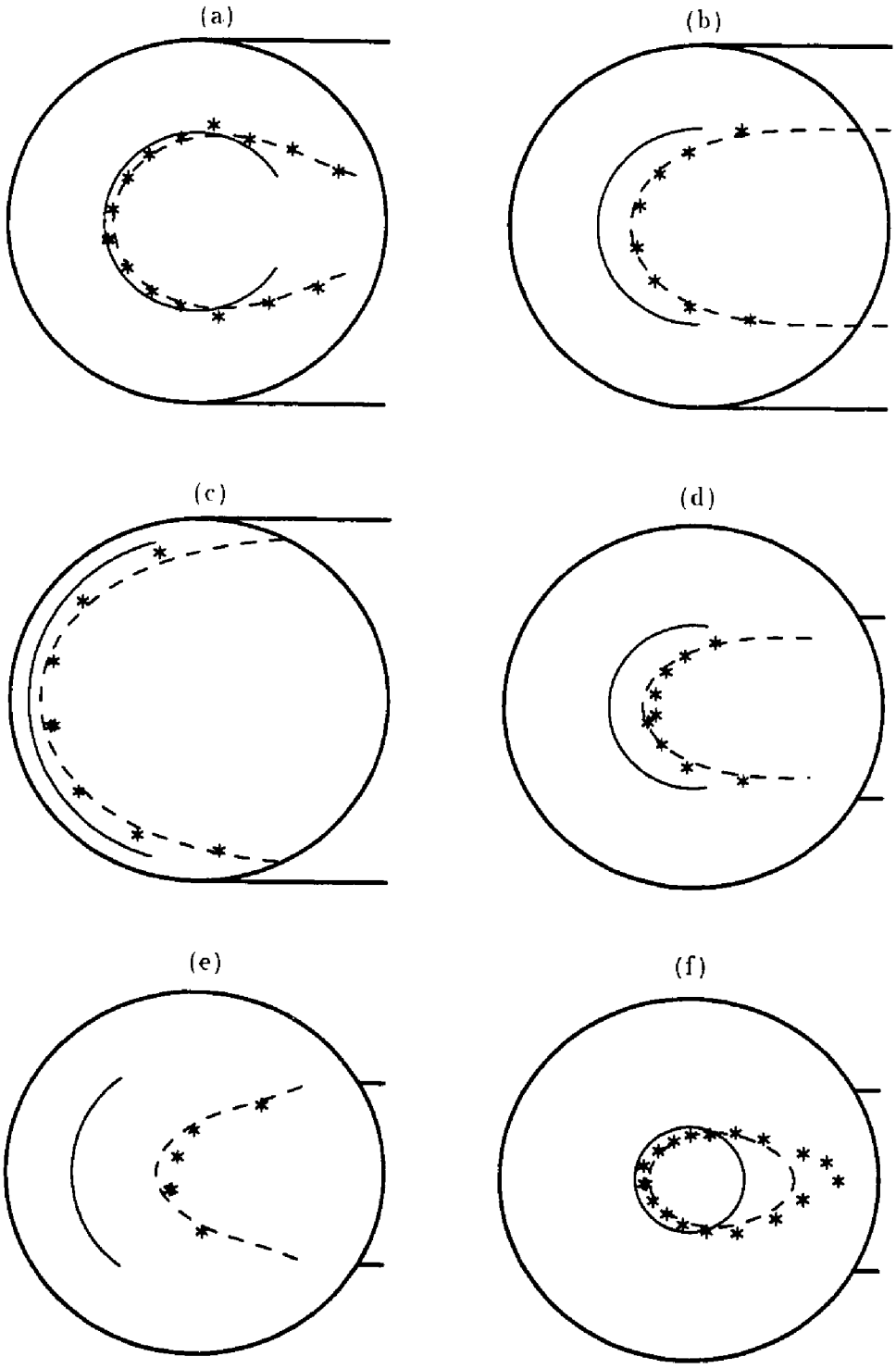

Figure 4-8: Some results of streamline tracing.

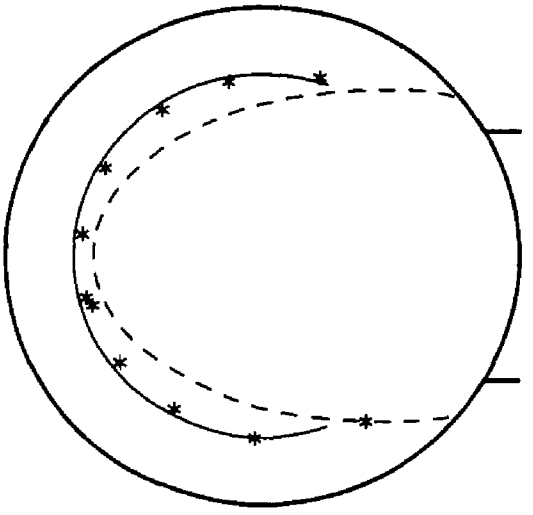

Figure 4-9: The worst match of computational and experimental results.

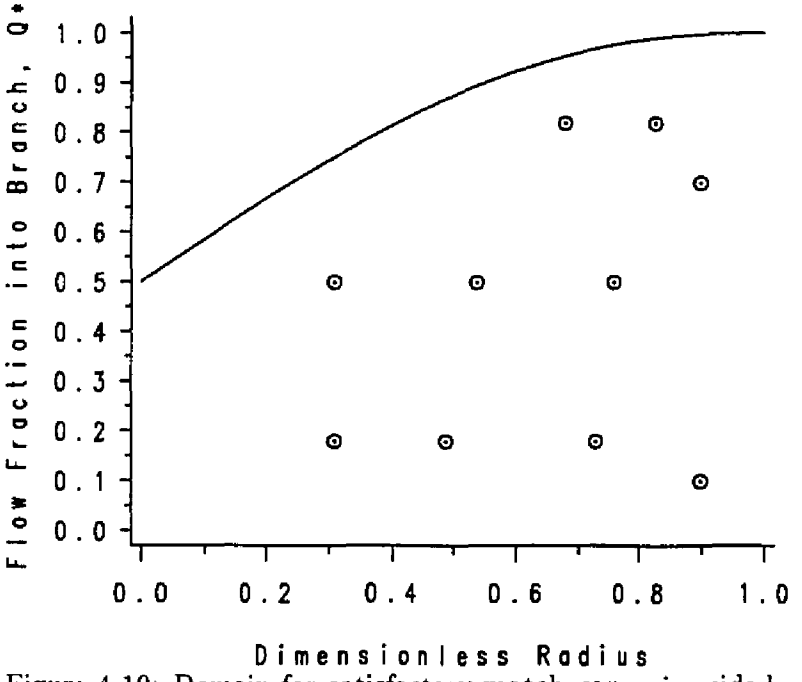

Figure 4-10: Domain for satisfactory match, same size side branch.

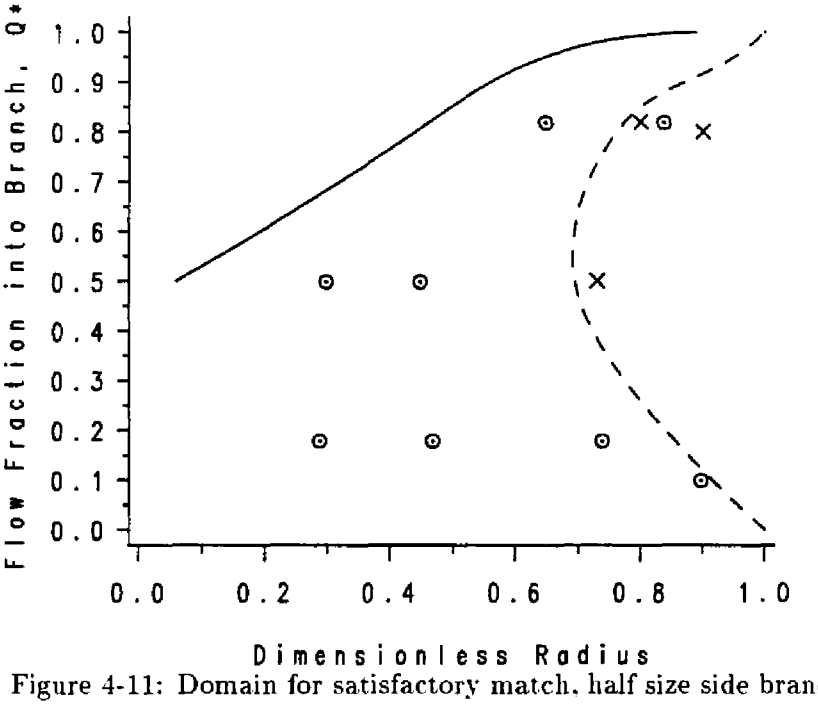

Figure 4-11: Domain for satisfactory match, half size side branch.

Chapter 5

Solution to the Model Equation

The detailed finite differencing numerical method used to solve Equations 3.10 and 3.12 is demonstrated in this chapter. *In vitro* experimental data are used to obtain the effective dispersion coefficient $\mathcal{D}$. The results by using uniform or parabolic shapes as final equilibuium hematocrit profiles are compared. Three velocity profiles as shown in Chapter 2 are applied alternatively to see their effects on red cell dispersion.

5.1 Numerics

To retain the advantage of a tri-diagonal matrix the Alternating-Direction-Implicit (ADI) method was used [62]. From Equation 3.10 the difference equations in both radial and angular directional sweeps were derived as following

$$(1-\xi^2)\frac{C_{i,j}^{k+\frac{1}{2}}-C_{i,j}^{k}}{\frac{\Delta\eta}{2}} = \frac{1}{\mathrm{Pe}}\left[\frac{C_{i-1,j}^{k+\frac{1}{2}}-2C_{i,j}^{k+\frac{1}{2}}+C_{i+1,j}^{k+\frac{1}{2}}}{(\Delta\xi)^2}+\frac{C_{i+1,j}^{k+\frac{1}{2}}-C_{i-1,j}^{k+\frac{1}{2}}}{2\xi\Delta\xi}\right.$$
$$\left.+\frac{C_{i,j-1}^{k}-2C_{i,j}^{k}+C_{i,j+1}^{k}}{\xi^2(\Delta\theta)^2}\right] \tag{5.1}$$

$$(1-\xi^2)\frac{C_{i,j}^{k+1}-C_{i,j}^{k+\frac{1}{2}}}{\frac{\Delta\eta}{2}} = \frac{1}{\mathrm{Pe}}\left[\frac{C_{i-1,j}^{k+\frac{1}{2}}-2C_{i,j}^{k+\frac{1}{2}}+C_{i+1,j}^{k+\frac{1}{2}}}{(\Delta\xi)^2}+\frac{C_{i+1,j}^{k+\frac{1}{2}}-C_{i-1,j}^{k+\frac{1}{2}}}{2\xi\Delta\xi}\right.$$
$$\left.+\frac{C_{i,j-1}^{k+1}-2C_{i,j}^{k+1}+C_{i,j+1}^{k+1}}{\xi^2(\Delta\theta)^2}\right] \tag{5.2}$$

where $\xi=(i-1)\Delta\xi$ and i,j,k are indices for ξ, θ, and η directions respectively. Indices numbering is shown in Figure 5-1.

Collecting similar terms gives

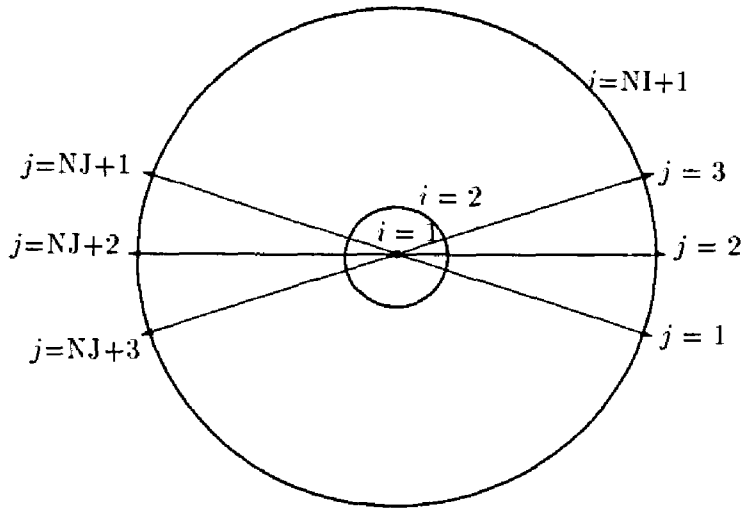

Figure 5-1: Numbering system.

$$C_{i-1,j}^{k+\frac{1}{2}}[\frac{1}{2\xi\Delta\xi} - \frac{1}{(\Delta\xi)^2}] + C_{i,j}^{k+\frac{1}{2}}[\frac{2}{(\Delta\xi)^2} + \frac{2\mathrm{Pe}(1-\xi^2)}{\Delta\eta}] + C_{i+1,j}^{k+\frac{1}{2}}[\frac{-1}{(\Delta\xi)^2} - \frac{1}{2\xi\Delta\xi}] = \frac{C_{i,j-1}^{k} - 2C_{i,j}^{k} + C_{i,j+1}^{k}}{\xi^2(\Delta\theta)^2} + C_{i,j}^{k}\frac{2\mathrm{Pe}(1-\xi^2)}{\Delta\eta} \tag{5.3}$$

$$C_{i,j-1}^{k+1}[\frac{-1}{\xi^2(\Delta\theta)^2}] + C_{i,j}^{k+1}[\frac{2}{\xi^2(\Delta\theta)^2} + \frac{2\mathrm{Pe}(1-\xi^2)}{\Delta\eta}] + C_{i,j+1}^{k+1}[\frac{-1}{\xi^2(\Delta\theta)^2}] = \frac{C_{i-1,j}^{k+\frac{1}{2}} - 2C_{i,j}^{k+\frac{1}{2}} + C_{i+1,j}^{k+\frac{1}{2}}}{(\Delta\xi)^2} + \frac{C_{i+1,j}^{k+\frac{1}{2}} - C_{i-1,j}^{k+\frac{1}{2}}}{2\xi\Delta\xi} + C_{i,j}^{k+\frac{1}{2}}\frac{2\mathrm{Pe}(1-\xi^2)}{\Delta\eta} \tag{5.4}$$

In these two equations the unknown variables are $C^{k+\frac{1}{2}}$'s and C^{k+1}'s on the left hand side of each equation.

The boundary condition requires that at i=NI+1,

$$C_{i+1,j} = C_{i-1,j}. \tag{5.5}$$

Substitution into Equation 5.3 and 5.4 gives

$$C_{i-1,j}^{k+\frac{1}{2}}[\frac{-2}{(\Delta\xi)^2}] + C_{i,j}^{k+\frac{1}{2}}[\frac{2}{(\Delta\xi)^2} + \frac{2\mathrm{Pe}(1-\xi^2)}{\Delta\eta}] + C_{i+1,j}^{k+\frac{1}{2}}[0] = \frac{C_{i,j-1}^{k} - 2C_{i,j}^{k} + C_{i,j+1}^{k}}{\xi^2(\Delta\theta)^2} + C_{i,j}^{k}\frac{2\mathrm{Pe}(1-\xi^2)}{\Delta\eta} \tag{5.6}$$

$$C_{i,j-1}^{k+1}\left[\frac{-1}{\xi^2(\Delta\theta)^2}\right]+C_{i,j}^{k+1}\left[\frac{2}{\xi^2(\Delta\theta)^2}+\frac{2\mathrm{Pe}(1-\xi^2)}{\Delta\eta}\right]+C_{i,j+1}^{k+1}\left[\frac{-1}{\xi^2(\Delta\theta)^2}\right]$$
$$=\frac{2C_{i-1,j}^{k+\frac{1}{2}}-2C_{i,j}^{k+\frac{1}{2}}}{(\Delta\theta)^2}+C_{i,j}^{k+\frac{1}{2}}\frac{2\mathrm{Pe}(1-\xi^2)}{\Delta\eta} \tag{5.7}$$

The singularity at $\xi = 0$ (i=1) was treated by summing values of nodes surrounding it [62].

$$C_{1,j}^{k+\frac{1}{2}}=\frac{2\Delta\eta}{\mathrm{Pe}}\frac{(2\sum_{j=3}^{\mathrm{NJ}+1}C_{2,j}^{k}+C_{2,2}^{k}+C_{2,\mathrm{NJ}+2}^{k})/(2\mathrm{NJ})-C_{1,j}^{k}}{(\Delta\xi)^2}+C_{1,j}^{k}. \tag{5.8}$$

The $C_{1,j}^{k+1}$ is obtained the same way. The symmetry about the tube half plane requires that $C_{i,1} = C_{i,3}$ and $C_{i,\mathrm{NJ}+3} = C_{i,\mathrm{NJ}+1}$.

Two systems of linear algebraic equation are solved for every full step advance in η-direction, one for the first half step and one for the second half. The first half step sweeping in ξ-dimension (Equation 5.3) results in a series of simultaneous linear equations. If the coefficient corresponding to each unknown variable $C^{k+\frac{1}{2}}$ in Equation 5.3 is denoted by $A_1(i), A_2(i), A_3(i)$ respectively, and the right hand side of Equation 5.3 is denoted by $B(i,j)$. Equation 5.3 can be expressed in a matrix form as following.

$$\begin{bmatrix} A_2(2) & A_3(3) & 0 & \cdots & & \\ A_1(2) & A_2(3) & A_3(4) & 0 & \cdots & \\ 0 & A_1(3) & A_2(4) & A_3(5) & 0 & \\ \vdots & 0 & \ddots & & & \vdots \\ & & & & \ddots & 0 \\ & \cdots & 0 & A_1(\mathrm{NI}\text{-}1) & A_2(NI) & A_3(\mathrm{NI}+1) \\ & & & 0 & A_1(\mathrm{NI}) & A_2(\mathrm{NI}+1) \end{bmatrix} \begin{bmatrix} C_{2,j}^{k+\frac{1}{2}} \\ C_{3,j}^{k+\frac{1}{2}} \\ C_{4,j}^{k+\frac{1}{2}} \\ \vdots \\ \vdots \\ C_{\mathrm{NI},j}^{k+\frac{1}{2}} \\ C_{\mathrm{NI}+1,j}^{k+\frac{1}{2}} \end{bmatrix} = \begin{bmatrix} B(2,j) \\ B(3,j) \\ B(4,j) \\ \vdots \\ \vdots \\ B(\mathrm{NI},j) \\ B(\mathrm{NI}+1,j) \end{bmatrix} \tag{5.9}$$

For j=2 to NJ+2 , $B(2,j)$ includes the first term in Equation 5.3 through the evaluation of C_1 from Equation 5.8. The A_1(NI) in the last row includes the coefficient of the third term of Equation 5.3 by applying Equation 5.5. The solved $C^{k+\frac{1}{2}}$'s are then passed to Equation 5.4 to solve for C^{k+1}'s in θ-directional sweep. Similarly, $A_1'(j), A_2'(i), A_3'(i)$ and

$B'(i,j)$ denote the coefficients of Equation 5.4 the matrix form is shown as follows.

$$\begin{bmatrix} A'_2(i) & A'_3(i) & 0 & \cdots & & \\ A'_1(i) & A'_2(i) & A'_3(i) & 0 & \cdots & \\ 0 & A'_1(i) & A'_2(i) & A'_3(i) & 0 & \\ \vdots & 0 & \ddots & & & \vdots \\ & & & & \ddots & 0 \\ & \cdots & 0 & A'_1(i) & A'_2(i) & A'_3(i) \\ & & & 0 & A'_1(i) & A'_2(i) \end{bmatrix} \begin{bmatrix} C'^{k+1}_{i,2} \\ C'^{k+1}_{i,3} \\ C'^{k+1}_{i,4} \\ \vdots \\ \vdots \\ C'^{k+1}_{i,\mathrm{NJ}+1} \\ C'^{k+1}_{i,\mathrm{NJ}+2} \end{bmatrix} = \begin{bmatrix} B'(i,2) \\ B'(i,3) \\ B'(i,4) \\ \vdots \\ \vdots \\ B'(i,\mathrm{NJ}+1) \\ B'(i,\mathrm{NJ}+2) \end{bmatrix} \quad (5.10)$$

For i=2 to NI+1, the $A'_3(i)$ in the first row includes the first term coefficient of Equation 5.4 and the $A'_1(i)$ in the last row includes the coefficient of the third term of Equation 5.4. These tridiagonal matrices were solved by simple eliminations and back substitutions.

A typical FORTRAN program used is listed in Appendix A. The program was tested for stability and convergence by varying mesh sizes in all three directions. The results are listed in Appendix B. The convergence is checked by comparing concentration profiles derived by specifying different mesh sizes. The comparison of two concentration profiles is accomplished by first calculating the flux-flow curve for each concentration profile, then finding the area between the two flux-flow curves as an indication of the difference between two concentration profiles. The difference of the initial concentration profile and the symmetric profile is used as a reference scale. The results show that no noticeable difference is observed by varying mesh sizes in radial and axial directions (less than 0.01% difference with respect to the reference scale). Obviously the ADI differencing is not unconditionally stable in cylindrical coordinates as it is in rectangular coordinates. It becomes unstable as $\Delta\eta$ is increased (or $\Delta\xi$ decreased). The mesh size in angular direction has little or no effect as far as the stability is concerned, but it will change the convergence when it is extremely small. Empirically we conclude that the solution is stable when the ratio $\frac{\Delta\eta/\mathrm{Pe}}{(\Delta\xi)^2}$ is less than about one half. The numerical solution was also checked against an analytical solution. A mesh density of [$\Delta\xi$,

$\Delta\theta$]=[(1-G)/65.π/45] with η/Pe equal to 0.02/240 has given satisfactory results.

The analytical solution readily available is for flat velocity profile and axisymmetrical situation, which means that the angular variation is absent [63]. With initial condition, $f(\xi)$, the solution has the form

$$C'(\xi,\eta) = \frac{2}{R_c^2}\sum_{n=0}^{\infty}\{[\exp(-2\alpha_n^2\eta/\mathrm{Pe}R_c^2)]\frac{J_0(\xi\alpha_n/R_c)}{J_0^2(\alpha_n)}\int_0^{R_c}\xi' f(\xi')J_0(\xi'\alpha_n/R_c)d\xi'\} \qquad (5.11)$$

where the α_n are the roots of

$$J_1(\alpha) = 0$$

An axisymmetric initial condition is specified for the testing of the numerical operations. The resulting concentration profile in two different axial locations are compared with the analytical solution derived from Equation 5.11. The detail is demonstrated in Appendix B. The results of the comparison show one to two percent difference between the analytical solution and the solution obtained by the method of finite differencing. The difference is almost parallel, that is, one of the concentration profile is always greater than the other throughout every radial position. A mass balance check between the initial concentration profile and a calculated downstream concentration profile is thus conducted to see whether this one to two percentage error is resulted from the finite differencing calculation. A difference less than 0.01% is found in this mass balance check. It is thus suspected that the one to two percentage error between analytical and the numerical solutions resulted from the specification of the initial condition. In the numerical solution, the initial condition cannot be assigned exactly the same as that in the analytical calculation due to the descretization. At the radial mesh size and the initial condition specified in the example run, the initial mass input difference is estimated to be about 1.5%, which explains the one to two percentage difference obtained earlier.

5.2 Comparison to data

Computational results were compared to published phase separation data in serial bifurcations [64]. These *in vitro* experimental data were obtained by perfusing blood through

models with two 50μm- 50μm bifurcations located on opposite sides of a straight tube. Reported experimental data include Q1*, the fractional flow off the first branch; Q2*, the fractional flow off the second branch; F2*, fractional red cell flux off the second branch; flow rate and tube length between bifurcations. Q1* quantifies the disturbance to the red cell profile, Q2* and F2* are used to produce flux-flow curves. Flux-flow plots can show the symmetry of the developing hematocrit profile. A symmetric flux-flow curve through point (0.5, 0.5) indicates that the hematocrit distribution is axisymmetric [37]. Data points were first sorted by Q1*. Four groups, with Q1* equal to 30%±5%, 40%±5%, 50%±5%, 60%±5% were obtained. In comparing the length in which dispersion of cells takes place the important parameter is η/Pe [65]. By definition

$$\frac{\eta}{\mathrm{Pe}} = (\frac{z}{R})(\frac{\mathcal{D}}{2\bar{v}R}) = (\frac{z}{Q})(\frac{\pi\mathcal{D}}{2}). \tag{5.12}$$

If $\mathcal{D}$ is assumed constant, z/Q becomes the important parameter. In each group of Q1*, collected data points were further divided into two sub-groups based on the reported z/Q values. Each set of sub-group is plotted on a flux-flow curve for comparison with calculation results. The grouped data is listed in Appendix B.

Once the velocity profile is chosen the numerical solution of the red cell concentration profile at any axial location, η/Pe, can be used to produce a flux-flow curve. A flat separating surface was used to calculate the red cell flux and volumetric flow through Equation 2.6 and 2.7. Calculated curves were compared to the experimental curves in an effort to determine which value of $(\eta/\mathrm{Pe})_{cal}$ best fit the data. The best fit curve is the one that minimizes the absolute error between experimental data and the calculated curve. The error is defined as the vertical distance between the two. By matching the average experimental z/Q and computational η/Pe corresponding to the best fit curves, the dispersion coefficient $\mathcal{D}$ can be calculated by definition as

$$\mathcal{D} = \frac{2}{\pi}\frac{\eta/\mathrm{Pe}}{z/Q} \tag{5.13}$$

5.2.1 Flat hematocrit profile

Assuming that the hematocrit profile tends to correct itself to a uniform distribution across the core region in the vessel. Figure 5-2 and 5-3 show the best fit flux-flow curve to each data group. Parabolic velocity profile and a 4μm plasma gap width (G=0.16) are used in the calculations. In each plot three curves are shown. The lowest curve is the curve calculated from the initial concentration profile (immediately after the branch), which is derived by the mapping techniques demonstrated in Section 3.1.2. While the upper most curve is for the axisymmetric concentration profile when the cells are totally rearranged. The curve between is the best fit to the data points according to the criteria stated above.

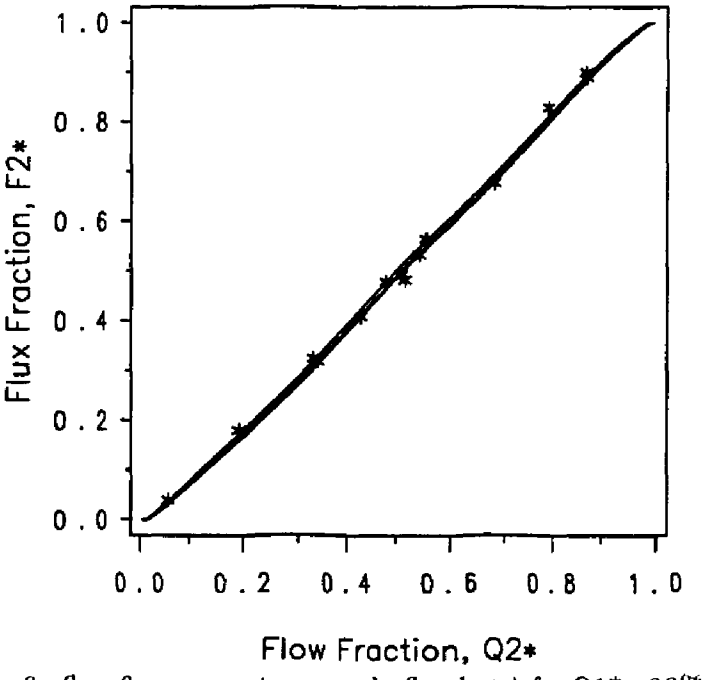

Figure 5-2: Best fit flux-flow curve (para. vel., flat hct.) for Q1*=30%, z/Q=134.2 s/mm^2.

For only two out of eight groups can the best fit curves be found within the initial and final equilibrium curves. The other plots showed that the initial and symmetric curves could not envelope the data. The calculated dispersion coefficients from matching the best fit curve are listed in Table 5.1.

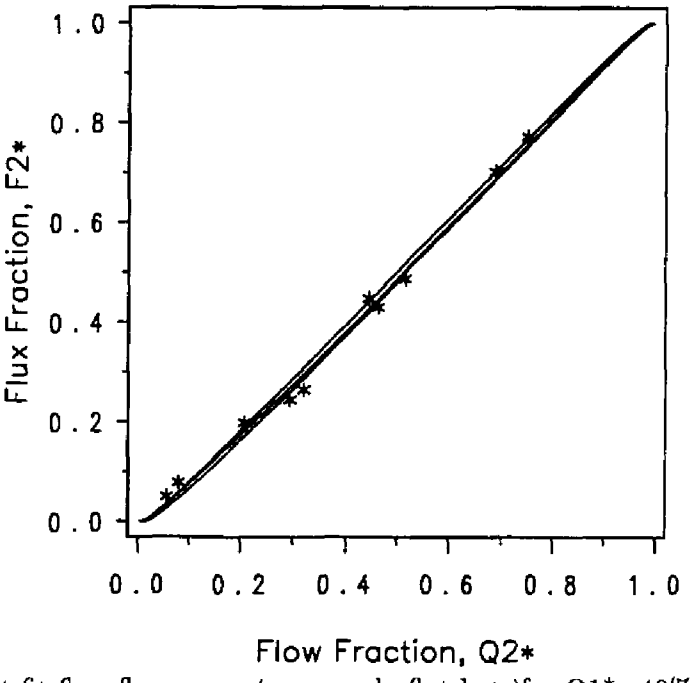

Figure 5-3: Best fit flux-flow curve (para. vel., flat hct.)for Q1*=40%, z/Q=142.0 s/mm^2.

Table 5.1: Dispersion coefficients for uniform hematocrit and parabolic velocity profiles

Q1* (%)	z/Q (s/mm^2)	$\mathcal{D}$ (cm^2/s)	Q1* (%)	z/Q (s/mm^2)	$\mathcal{D}$ (cm^2/s)
30	24.6	$< 2.2 \times 10^{-9}$	50	22.2	$< 2.4 \times 10^{-8}$
30	134.2	7.9×10^{-7}	50	153.9	$< 3.4 \times 10^{-9}$
40	24.4	$< 2.2 \times 10^{-8}$	60	52.6	$> 2.4 \times 10^{-5}$
40	142.0	9.3×10^{-7}	60	488.2	$< 1.1 \times 10^{-9}$

Having not been able to envelope most of the data by the calculation, the idea of parabolic hematocrit profile was proposed. The area enclosed by the two extreme curves (initial curve and symmetric curve) is anticipated to be broader.

5.2.2 Parabolic hematocrit profile

A two-dimentional study [26] showed that the equilibrium RBC concentration profile across a slit is not necessarily uniform in a small channel. The equilibrium profile of hematocrit for three-dimensional tube flow is not clear yet. The effect of hematocrit profile on the results of the calculation is examined in this section by forcing a parabolic profile as the final equilibrium profile. Assuming the same governing equation (Equation 3.4) except that the asymptotic hematocrit profile has changed to a parabolic one, the driving force of the rearranging process can be thought of as the concentration deviation from the parabolic equilibrium profile. The initial concentration profile was obtained by tracing back every node in the domain to its location upstream from the first bifurcation. Assuming a fully developed parabolic hematocrit profile upstream of the first bifurcation, the same mapping technique was used to obtain the initial profile. Having Q1* and the corresponding F1* for the first bifurcation, the magnitude of the final hematocrit profile was calculated by conservation of the red cells. The actual initial concentration profile fed into the computer program is the difference between this mapped initial profile and the final parabolic profile. The output concentration profile from the calculations is added back to the final parabolic hematocrit profile to calculate the flux-flow curve.

The resulting dispersion coefficients are listed in Table 5.2. The calculated flux-flow plots matching the experimental data are shown in Figure 5-4, 5-5, 5-6, 5-7, 5-8, and Figure 5-9.

The problem of not being able to envelope the data within two extreme curves seemed to improve by using the parabolic equilibrium hematocrit profile. Among eight cases, best fits could be found for all except two. But these figures (5-4 through 5-9) also showed that the best fit curves are not in harmony with the trend of the data. Almost all the fitted curves start at lower F* than the data when the Q* is small, and increase more sharply

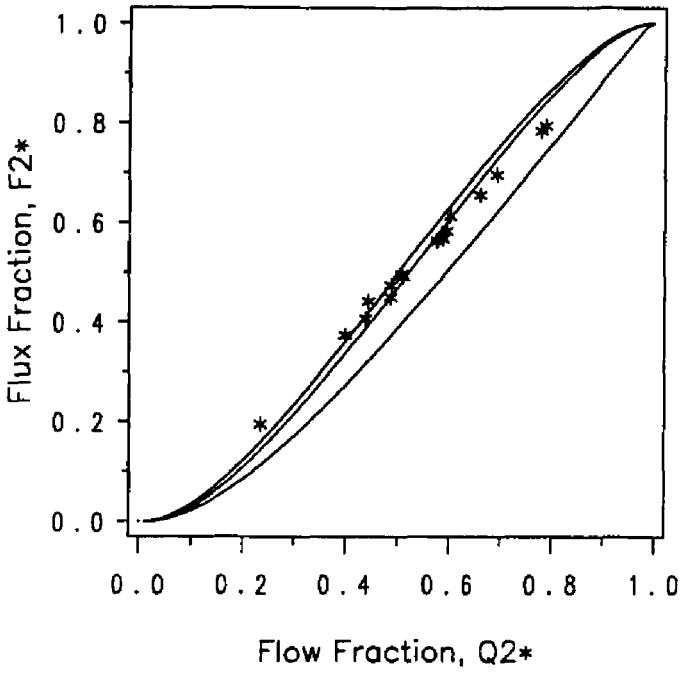

Figure 5-4: Best fit flux-flow curve (para. vel., para. hct.) for Q1*=30%, z/Q=24.6 s/mm^2.

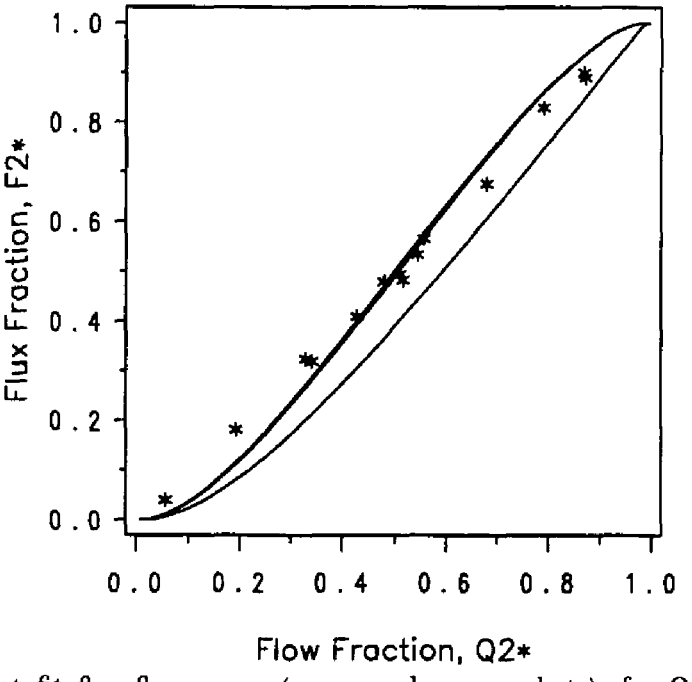

Figure 5-5: Best fit flux-flow curve (para. vel., para. hct.) for Q1*=30%, z/Q=134.2 s/mm^2.

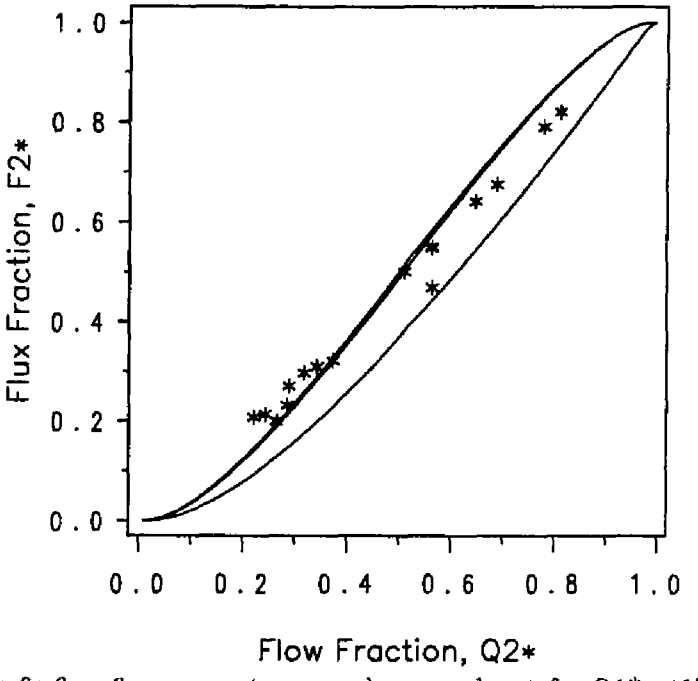

Figure 5-6: Best fit flux-flow curve (para. vel., para. hct.) for Q1*=40%, z/Q=24.4 s/mm^2.

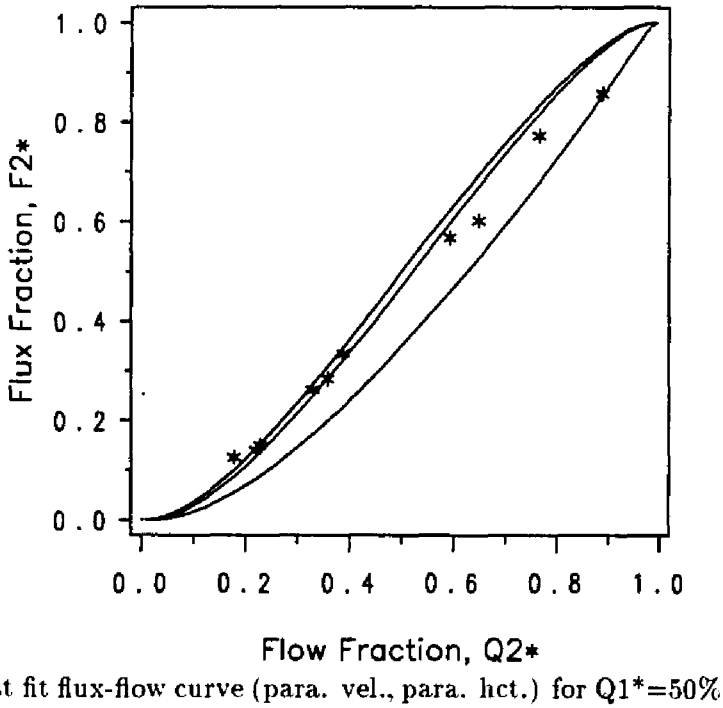

Figure 5-7: Best fit flux-flow curve (para. vel., para. hct.) for Q1*=50%, z/Q=22.2 s/mm^2.

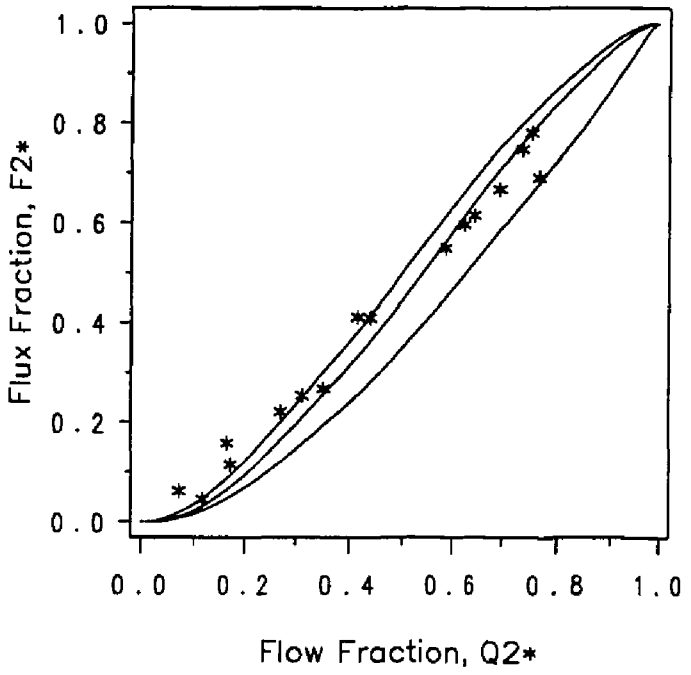

Figure 5-8: Best fit flux-flow curve (para. vel., para. hct.) for Q1*=50%, z/Q=153.94 s/mm^2.

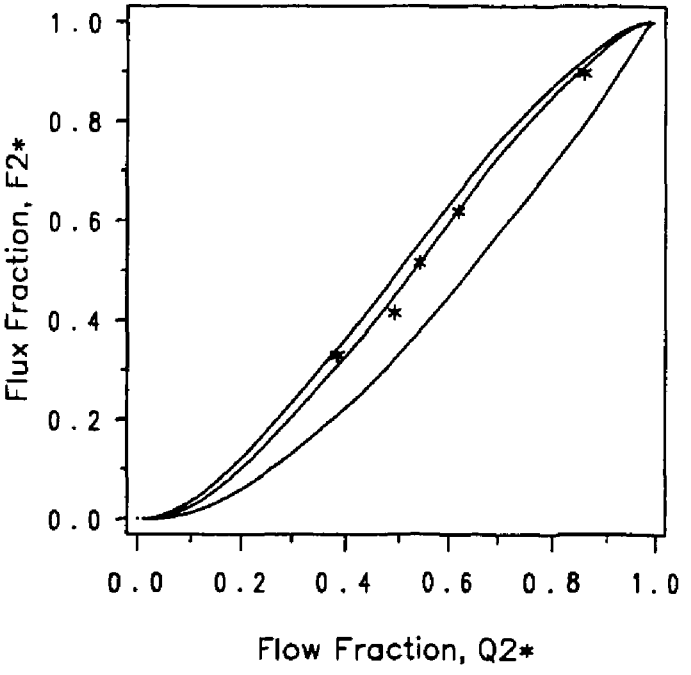

Figure 5-9: Best fit flux-flow curve (para. vel., para. hct.) for Q1*=60%, z/Q=488.2 s/mm^2.

Table 5.2: Dispersion coefficients for parabolic hematocrit and parabolic velocity profiles

Q1* (%)	z/Q (s/mm^2)	$\mathcal{D}$ (cm^2/s)	Q1* (%)	z/Q (s/mm^2)	$\mathcal{D}$ (cm^2/s)
30	24.6	4.2×10^{-5}	50	22.2	5.5×10^{-5}
30	134.2	1.3×10^{-5}	50	153.9	5.0×10^{-6}
40	24.4	7.4×10^{-5}	60	52.6	$> 6.6 \times 10^{-5}$
40	142.0	$> 2.5 \times 10^{-5}$	60	488.2	2.2×10^{-6}

than the data do. Finally all the curves end up at a higher F* when the Q* approaches 1. Two more steps were taken to counter this: one was to introduce a flat velocity profile in the computation: the other was to take into account the shear effects.

It was suggested that a flat velocity profile would be closer to the experimental situations. In order to use a flat velocity profile the plasma gap width was adjusted by refitting the experimental data obtained by Carr [24] for 50 μm tubes. The best fit curve supported the gap width to be 1.75 μm (G=0.07). Similar procedures were followed by using the flat velocity profile. The calculated dispersion coefficients are shown in Table 5.3.

Table 5.3: Dispersion coefficients for uniform hematocrit and flat velocity profiles

Q1* (%)	z/Q (s/mm^2)	$\mathcal{D}$ (cm^2/s)	Q1* (%)	z/Q (s/mm^2)	$\mathcal{D}$ (cm^2/s)
30	24.6	1.7×10^{-5}	50	22.2	$< 1.2 \times 10^{-6}$
30	134.2	5.5×10^{-6}	50	153.9	5.2×10^{-7}
40	24.4	2.0×10^{-5}	60	52.6	$> 3.5 \times 10^{-5}$
40	142.0	1.7×10^{-6}	60	488.2	3.8×10^{-7}

The results of the best fit are shown in Figure 5-10, 5-11, 5-12, 5-13, 5-14 and Figure 5-15. The use of a flat velocity profile resulted in six out of eight best fit curves. The matching of the curves and the data is satisfactory.

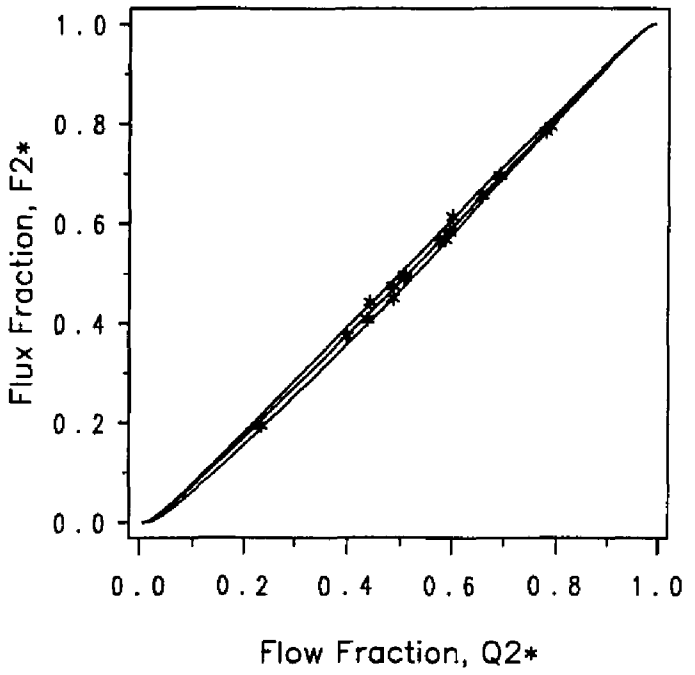

Figure 5-10: Best fit flux-flow curve (flat vel., flat hct.) for Q1*=30%, z/Q=24.6 s/mm^2.

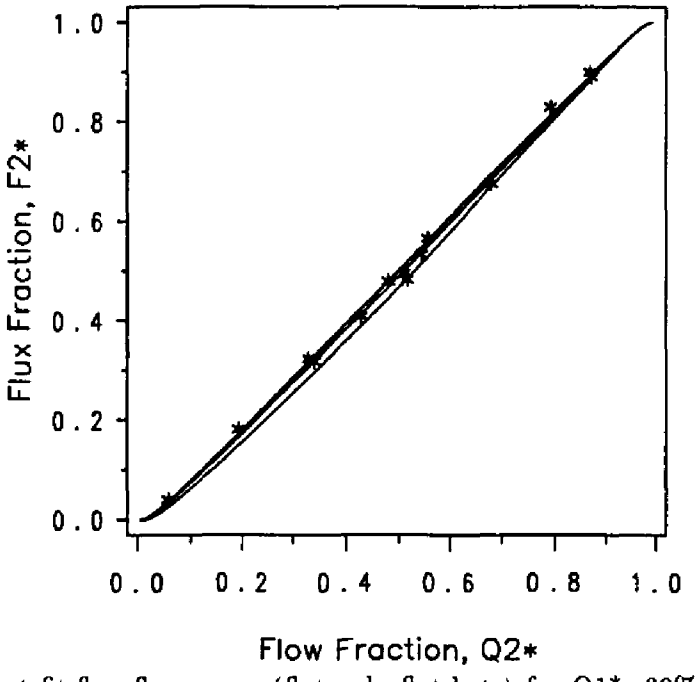

Figure 5-11: Best fit flux-flow curve (flat vel., flat hct.) for Q1*=30%, z/Q=134.2 s/mm^2.

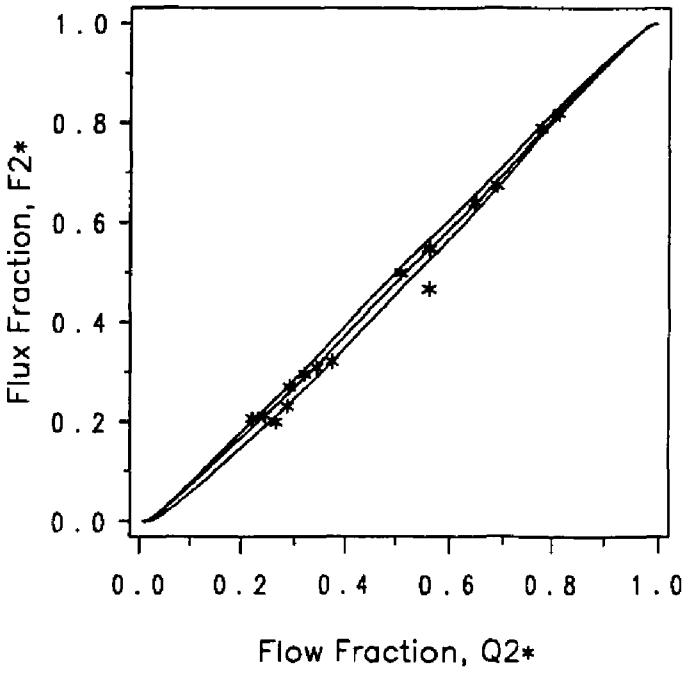

Figure 5-12: Best fit flux-flow curve (flat vel., flat hct.) for Q1*=40%, z/Q=24.4 s/mm^2.

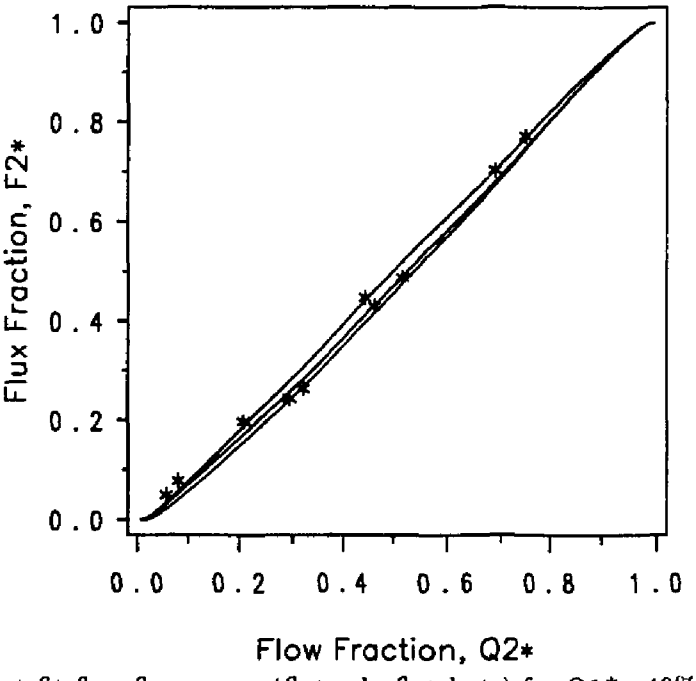

Figure 5-13: Best fit flux-flow curve (flat vel., flat hct.) for Q1*=40%, z/Q=142.0 s/mm^2.

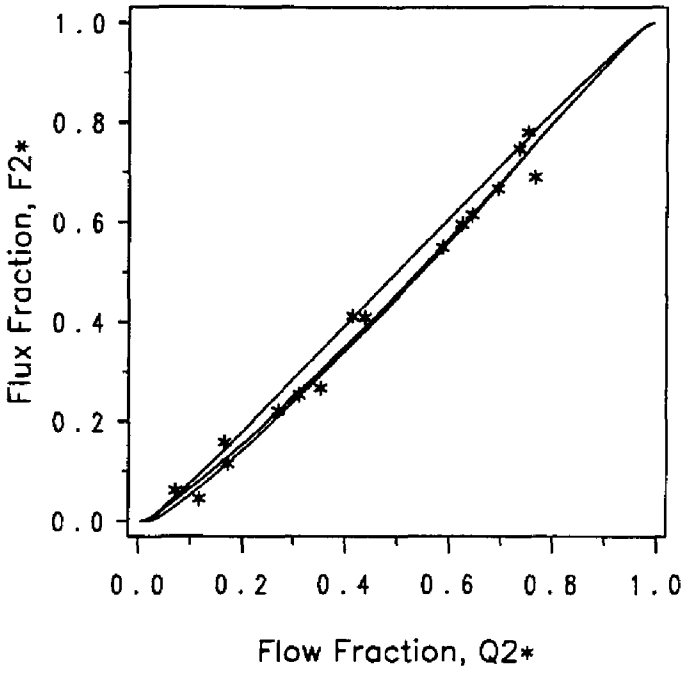

Figure 5-14: Best fit flux-flow curve (flat vel., flat hct.) for Q1*=50%, z/Q=153.9 s/mm^2.

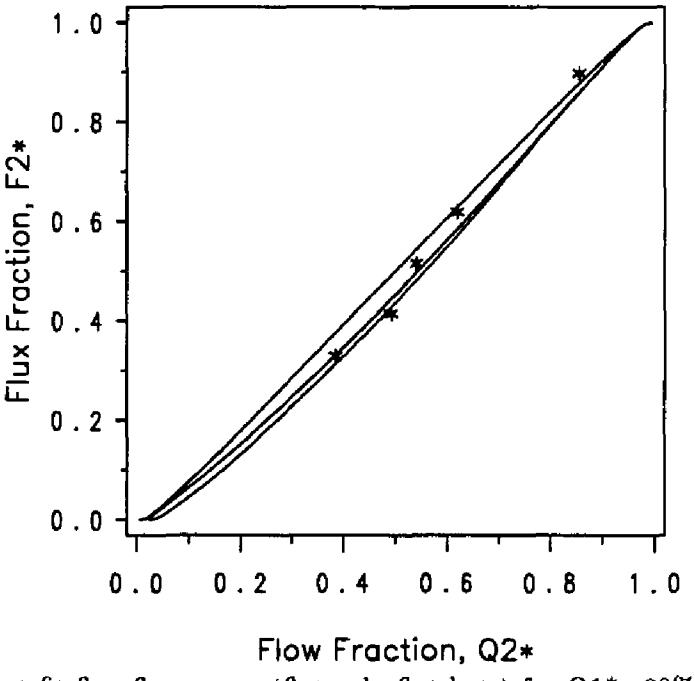

Figure 5-15: Best fit flux-flow curve (flat vel., flat hct.) for Q1*=60%, z/Q=488.2 s/mm^2.

5.2.3 Zydney's correlation for "$\mathcal{D}$"

The diffusivity is likely to be shear rate dependent instead of a global constant. It is desired to evaluate the validity of Equation 3.4 at different shear rates. Zydney [66] collected published self-diffusion data for suspensions of deformable particles, both liquid drops and red blood cells in tube flow. With the local shear rates evaluated at the mean particle position using reported velocity profile he replotted the dimensionless effective particle diffusivity $\mathcal{D}/(a^2\gamma)$ versus particle volume fraction and proposed a formula to fit the data

$$\frac{\mathcal{D}_p}{a^2\gamma} = k\phi_p(1-\phi_p)^n, \tag{5.14}$$

where $\mathcal{D}_p$ is the particle diffusivity, a is the particle radius, γ is the local shear rate, and ϕ_p is the particle volumetric fraction. The k and n were parameters evaluated by the best fit to the experimental data and found to be 0.15 and 0.8 respectively. Having this correlation the dispersion coefficient $\mathcal{D}$ in Equation 5.12 need not to be constant any more. Although it is still not possible to treat the dispersion coefficient at each point, it can now be shown how an "overall" shear rate during the experiment affects the proposed constant dispersion coefficient model.

After being grouped by Q1*, the experimental data were regrouped by η/Pe, instead of z/Q as in the previous section. If the wall shear rate of a Poiseuille flow is substituted into the Zydney's correlation, the parameter η/Pe becomes

$$\frac{\eta}{\mathrm{Pe}} = \frac{2za^2k\phi_p(1-\phi_p)^n}{R^3}. \tag{5.15}$$

Seven sets of regrouped data based on η/Pe were obtained with their η/Pe shown in Table 5.4. The regrouped data are also shown in Appendix C. A similar finite differencing program was run and the best fit flux-flow curve found for each group of data. Using a flat aymptotic hematocrit profile, flat and 2-phase velocity profiles were examined in this set of calculations. Figure 5-16, 5-17, 5-18, 5-19, 5-20, 5-21,and Figure 5-22 show the best fit curves and Table 5.5 shows the comparisons of η/Pe between calculation and experiments for flat velocity profile being used.

Table 5.4: Experimental data grouped by η/Pe

Q1*	$(\eta/\mathrm{Pe})_{\max.}$	$(\eta/\mathrm{Pe})_{\min.}$	$(\eta/\mathrm{Pe})_{\mathrm{avg.}}$	no. of data
30%	0.09	0.08	0.082	8
30%	0.10	0.09	0.094	24
40%	0.10	0.09	0.094	17
50%	0.07	0.06	0.061	9
50%	0.10	0.09	0.095	22
60%	0.12	0.11	0.118	6
60%	1.00	0.89	0.898	5

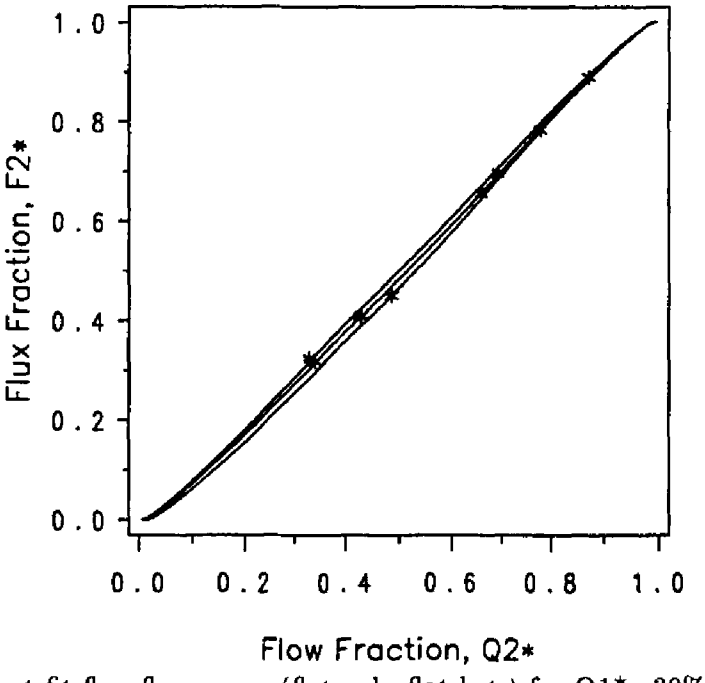

Figure 5-16: Best fit flux-flow curve (flat vel., flat hct.) for Q1*=30%, $(\eta/\mathrm{Pe})_{exp.}$=0.082.

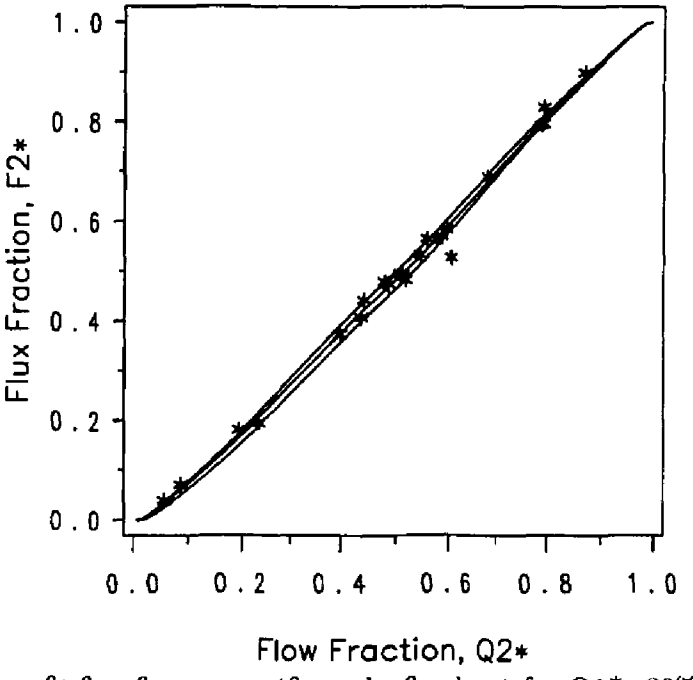

Figure 5-17: Best fit flux-flow curve (flat vel., flat hct.) for Q1*=30%. $(\eta/\mathrm{Pe})_{exp.}$=0.094.

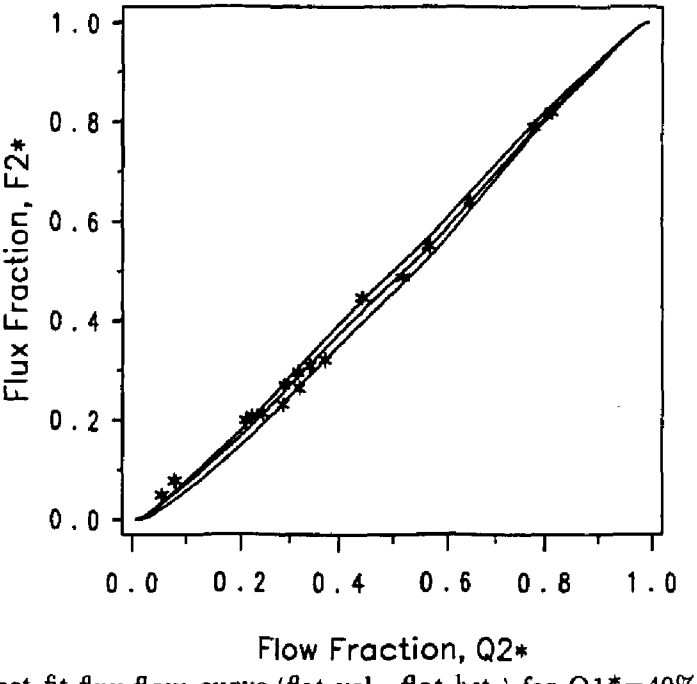

Figure 5-18: Best fit flux-flow curve (flat vel., flat hct.) for Q1*=40%. $(\eta/\mathrm{Pe})_{exp.}$=0.094.

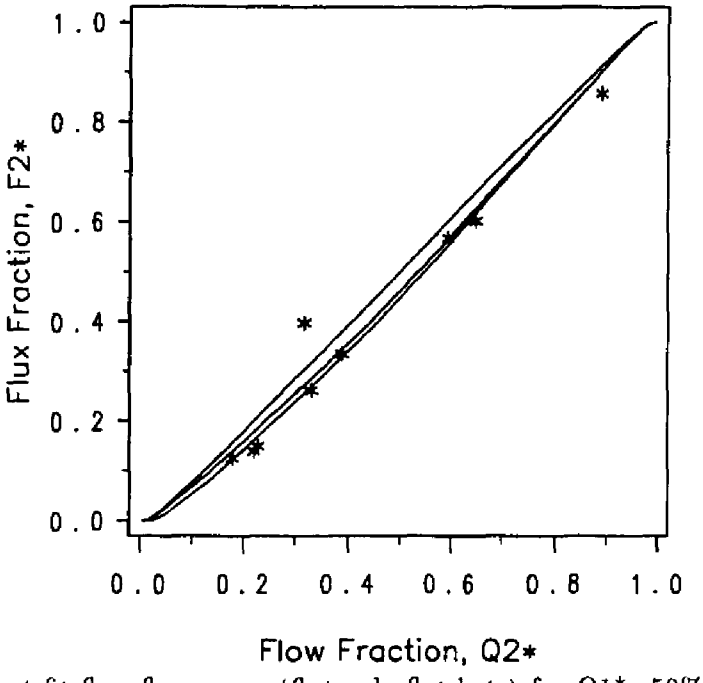

Figure 5-19: Best fit flux-flow curve (flat vel., flat hct.) for Q1*=50%, $(\eta/\mathrm{Pe})_{exp.}$=0.061.

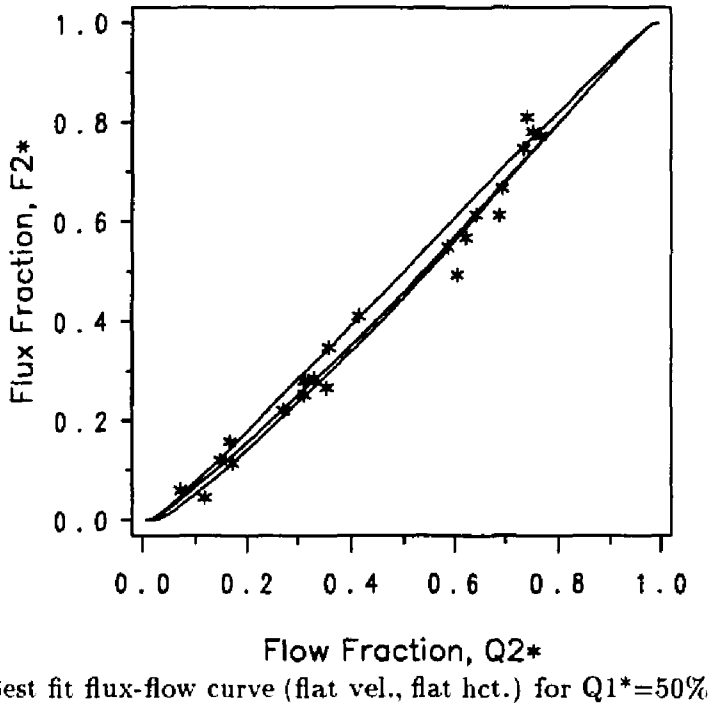

Figure 5-20: Best fit flux-flow curve (flat vel., flat hct.) for Q1*=50%, $(\eta/\mathrm{Pe})_{exp.}$=0.095.

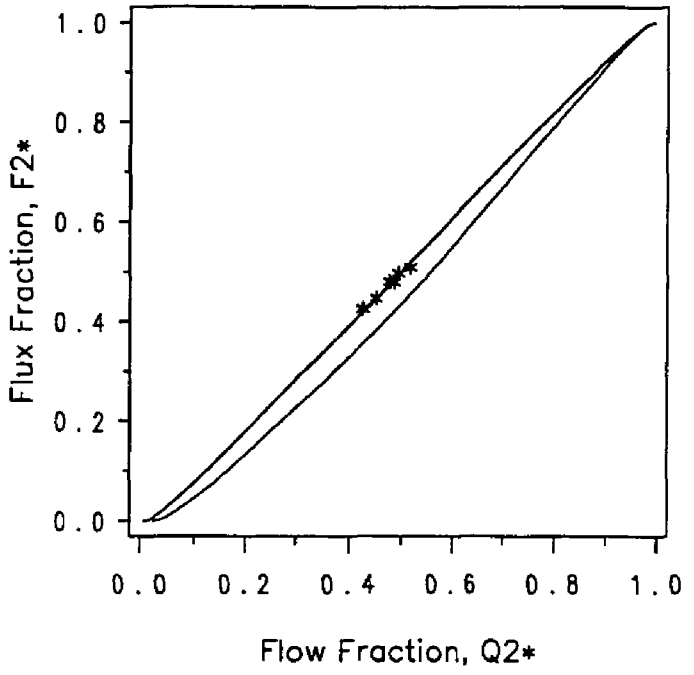

Figure 5-21: Best fit flux-flow curve (flat vel., flat hct.) for Q1*=60%. $(\eta/\mathrm{Pe})_{exp.}$=0.118.

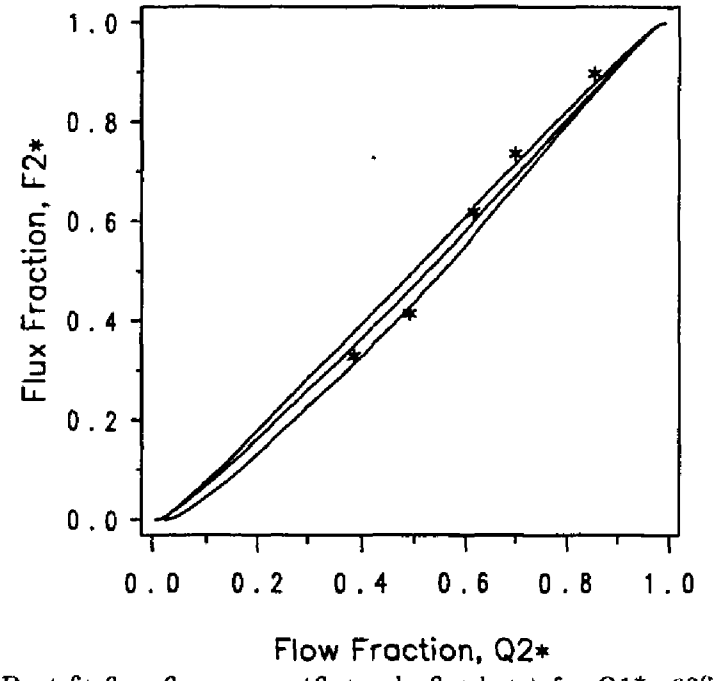

Figure 5-22: Best fit flux-flow curve (flat vel., flat hct.) for Q1*=60%, $(\eta/\mathrm{Pe})_{exp.}$=0.89.

Table 5.5: Comparison of experimental and calculated η/Pe in flat vel. prof.

Q1*	$(\eta/\mathrm{Pe})_{\mathrm{exp.}}$	$(\eta/\mathrm{Pe})_{\mathrm{cal.}}$	$\frac{(\eta/Pe)_{exp.}}{(\eta/Pe)_{cal.}}$
30%	0.082	0.079	1.04
30%	0.094	0.079	1.19
40%	0.094	0.079	1.19
50%	0.061	0.033	1.85
50%	0.095	0.025	3.80
60%	0.118	0.454	0.26
60%	0.898	0.088	10.20

For convenience, in the case of 2-phase velocity profile the Pe was redefined as

$$\mathrm{Pe} = \frac{\bar{v}R[(1-G)^2(A-\phi) + \frac{(1-G)^4(\phi-1)+\phi}{2}]}{\mathcal{D}} \tag{5.16}$$

Results of computation and experiments are shown in Figure 5-23, 5-24, 5-25, 5-26, 5-27, 5-28 and Table 5.6.

Table 5.6: Comparison of experimental and calculated η/Pe for 2-phase velocity profile.

Q1*	$(\eta/\mathrm{Pe})_{\mathrm{exp.}}$	$(\eta/\mathrm{Pe})_{\mathrm{cal.}}$	$\frac{(\eta/\mathrm{Pe})_{exp}}{(\eta/\mathrm{Pe})_{cal}}$
30%	0.161	0.067	2.4
30%	0.186	0.042	4.5
40%	0.186	0.100	1.9
50%	0.121	0.033	3.7
50%	0.187	0.033	5.7
60%	0.234	—	—
60%	1.773	0.108	16.4

The sensitivity of the initial condition on the best fit results is investigated. Each data set is fitted by increasing or decreasing the initial condition (the Q1*) one tenth of the

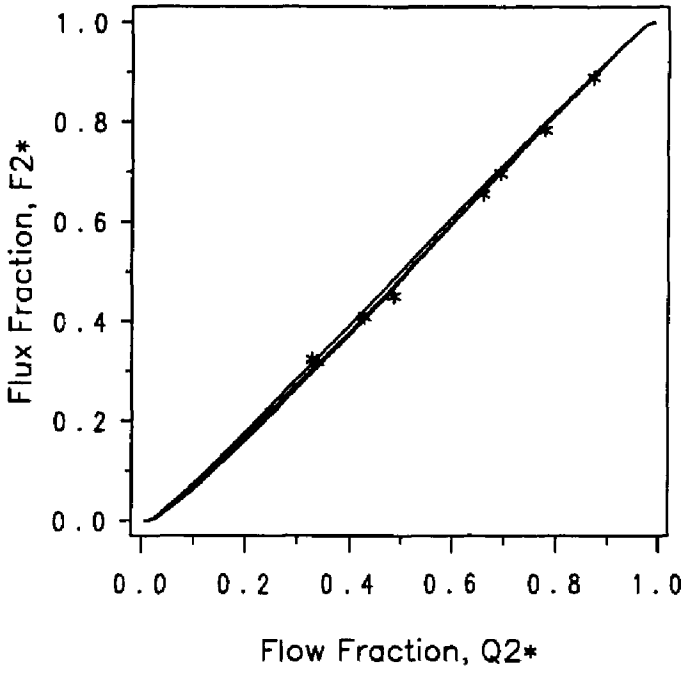

Figure 5-23: Best fit flux-flow curve (2-ph. vel.. flat hct.) for Q1*=30%. $(\eta/\mathrm{Pe})_{exp.}$=0.161.

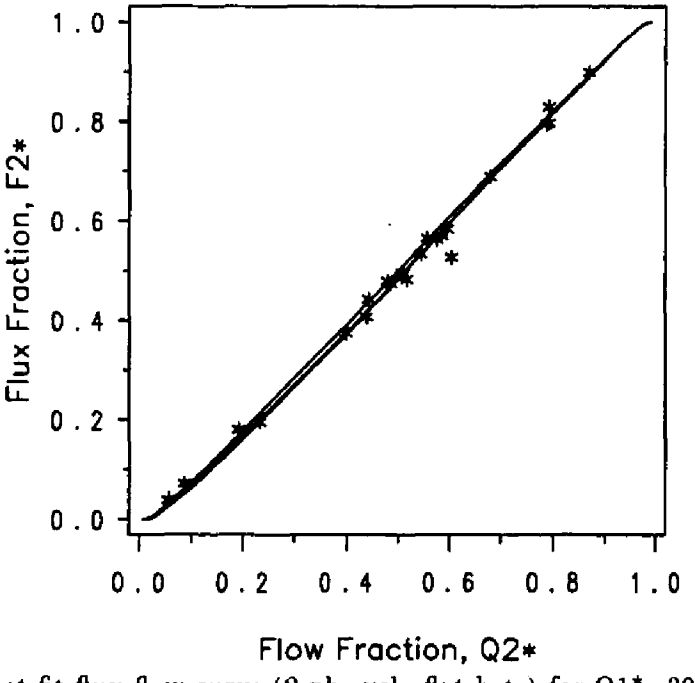

Figure 5-24: Best fit flux-flow curve (2-ph. vel., flat hct.) for Q1*=30%, $(\eta/\mathrm{Pe})_{exp.}$=0.186.

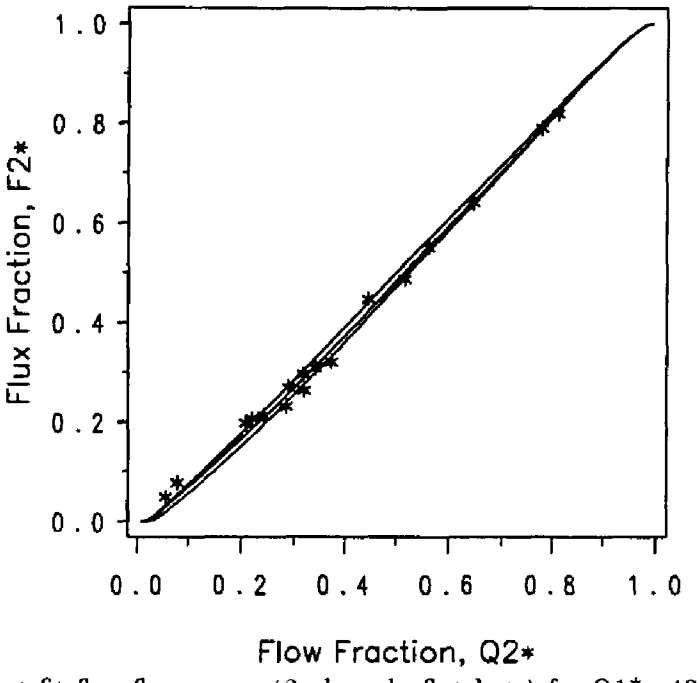

Figure 5-25: Best fit flux-flow curve (2-ph. vel., flat hct.) for Q1*=40%, $(\eta/\mathrm{Pe})_{exp.}$=0.186.

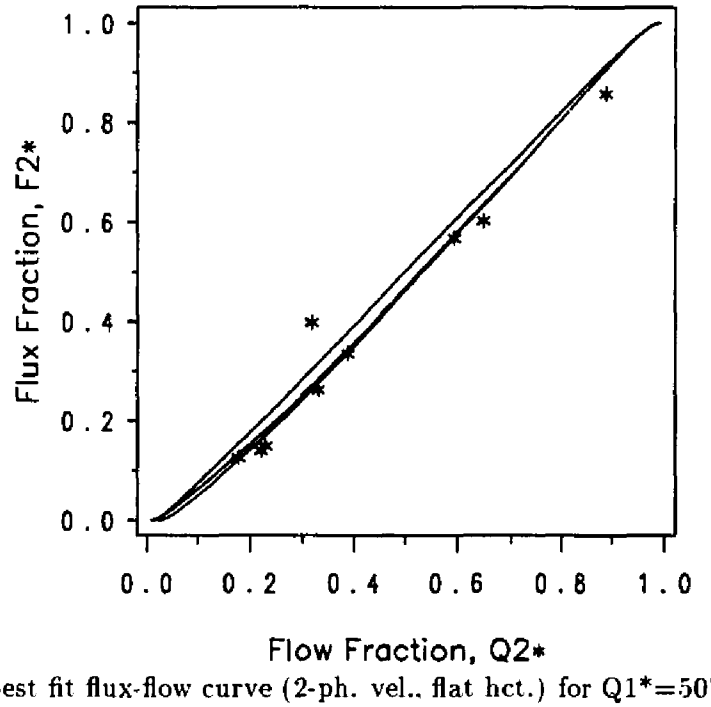

Figure 5-26: Best fit flux-flow curve (2-ph. vel., flat hct.) for Q1*=50%, $(\eta/\mathrm{Pe})_{exp.}$=0.121.

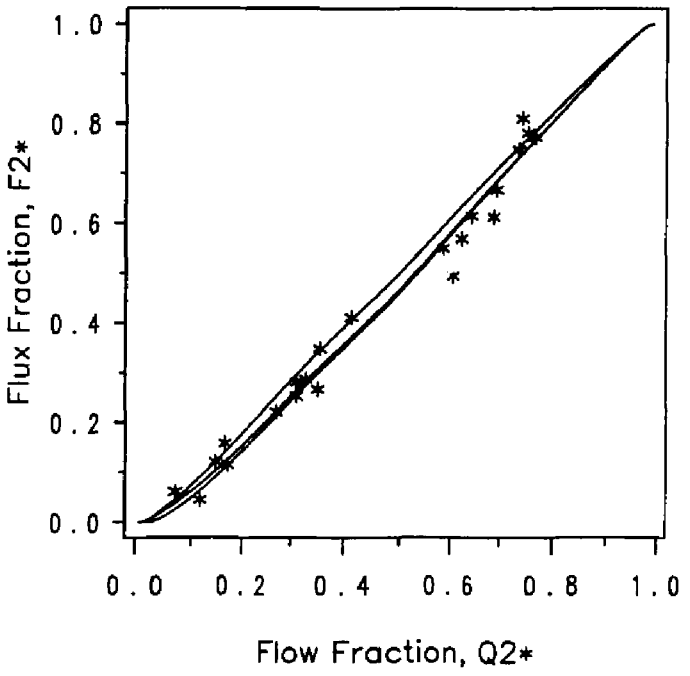

Figure 5-27: Best fit flux-flow curve (2-ph. vel., flat hct.) for Q1*=50%. $(\eta/\mathrm{Pe})_{exp.}$=0.187.

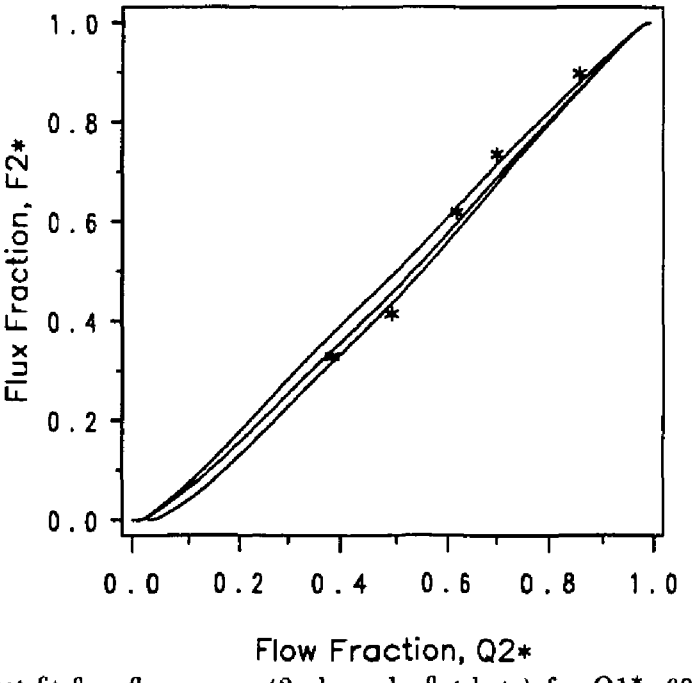

Figure 5-28: Best fit flux-flow curve (2-ph. vel., flat hct.) for Q1*=60%, $(\eta/\mathrm{Pe})_{exp.}$=1.773.

total flow. The ratio of $(\eta/\mathrm{Pe})_{exp.}$ to $(\eta/\mathrm{Pe})_{cal.}$ is plotted against Q1* for each data set. Figure 5-29 shows such plots. The footnote on the figure shows that the plus signs represent the results for best fitting the data set with Q1*=30%, $(\eta/\mathrm{Pe})_{exp.}$=0.082, and so on.

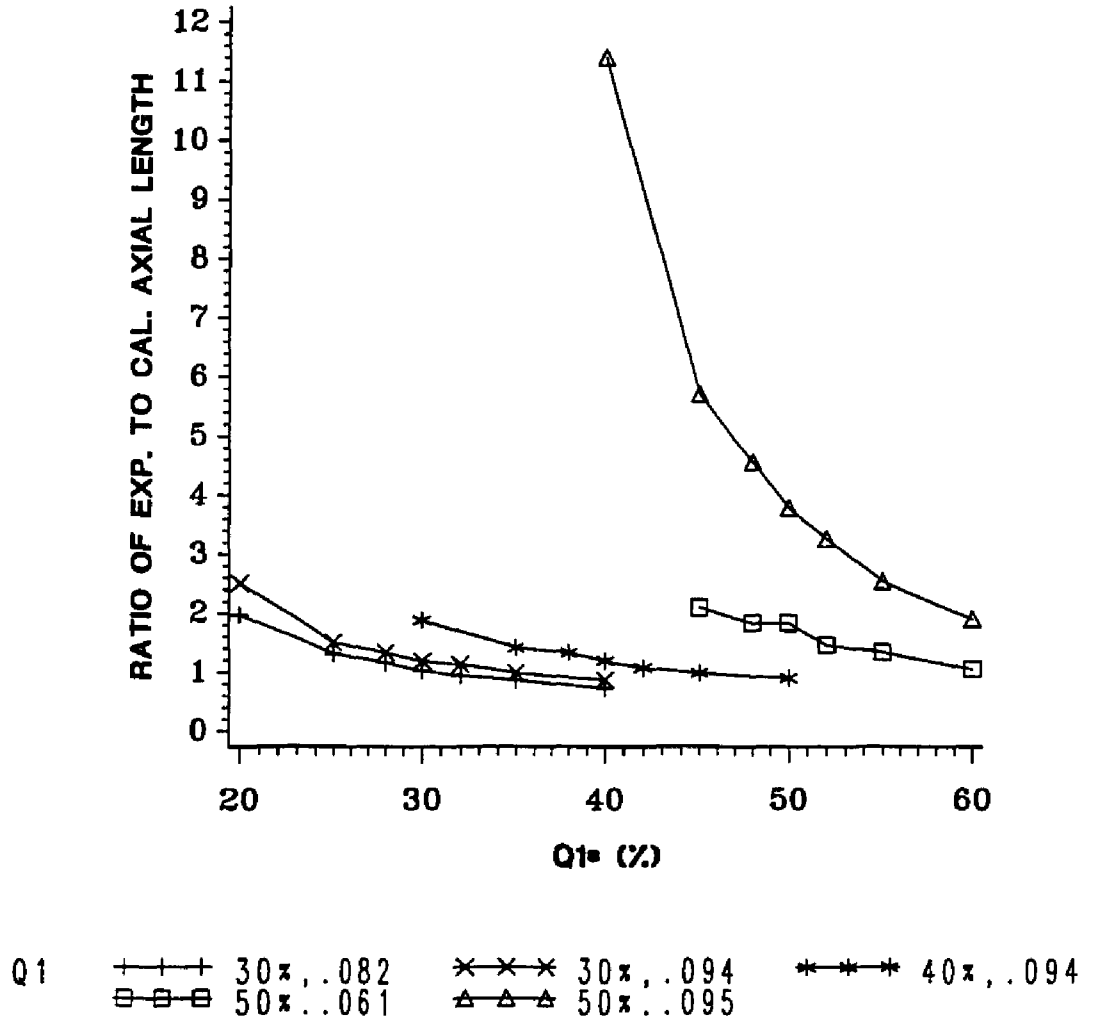

Figure 5-29: Sensitivity of initial concentration.

Noted that the experimental data were first grouped by Q1*, has 10% spanning in each set of data. For example, the data categorized in the data set with Q1*=30% have measured Q1* span from 25% to 35%.

5.3 Discussion

The dispersion coefficients obtained by the best fit to *in vitro* experimental data are on the order of 10^{-5} to 10^{-7}, about two orders of magnitude greater than the self-diffusion coefficient derived by Goldsmith [21]. The reported wall shear rates (calculated by assuming Poiseuille flow) under which the data used in this study were gathered, were also at least one to two orders of magnitude higher than those reported in Goldsmith's paper. Consulting the dimensionless parameter $\mathcal{D}/a^2\gamma$, the "averaged" dispersion coefficients obtained in this study still seem to be slightly greater than the reported self-diffusion coefficient, which agrees with the result reported by Leighton and Acrivos [67,68] for rigid particles: the net effect of non-random particle motion enhances the particle dispersion. The disagreement of computations and experiments for cases when Q1*=60% might be attributed to the following two reasons: one is the fewer experimental data available (5 and 6 points in each group); the other is the inaccuracy in estimating the initial condition when the withdrawal (disturbance) is large.

Table 5.5 and 5.6 reveal that the experimental η/Pe values are always higher than the calculated ones (results for Q1*=60% were excluded due to the reasons stated above). Although all the differences are either within the 95% confidence interval of Zydney's correlation (Equation 5.14) or within the error range of the data collected for the correlation, it is suspected that the use of wall shear rate of a Poiseuille flow ($4\bar{v}/R$) explains some of the difference. Because of the blunting of the velocity profile at the cell concentrated region, the actual shear rate in which the red cell dispersion takes place could be less than the number being put into Equation 5.14 for $\mathcal{D}$. This means the real values of $(\eta/\mathrm{Pe})_{exp}$ would be smaller than suggested and the agreement would be better. Another reason for this difference may be the initial condition used in the calculation. The shape of the separating surface and the mapping technique are derived from situations with parabolic velocity profiles, while in the tubular flow of the blood suspension they may be different. If the initial condition (cell distribution) has not been defined appropriately, the disagreement between calculation and experiment would not be a surprise.

Chapter 6

Simple Network Model

The mathematical models proposed in previous chapters are to be combined and applied to very simple vessel networks in this chapter. The network model is first generated, subjected to the parameters available and the limitations of the mathematical model presented in this dissertation. The hematocrit of each branch of the network is then calculated either with or without the diffusion model. The results of the hematocrit distribution are presented in a vector form to permit comparison among different situations. The comparison is done by choosing a "reference" vector and calculating the deviation of each vector from this reference.

The "network Fahraeus effect" is first examined to see how the hematocrit shift effects the overall network hematocrit [69,70]. Based on the mass conservation law, the network Fahraeus effect states that in a complete network of branching vessels, the number average discharge hematocrit of the network is definitely less than the discharge hematocrit that feeds the network if the following three conditions are satisfied. Condition 1) the flow heterogeneity exists among the network vessels. 2) a discharge hematocrit heterogeneity exists due to the phase separation at upstream junctions. 3) the flow and discharge hematocrit are positively correlated. It should be noted that the network Fahraeus effect still can be seen even when the positive correlation between flow and discharge hematocrit is not strong.

The next question asked is, how far downstream can a disturbance in the volumetric flow distribution in the network be propagated and detected. The disturbance is modeled by varying the flow split in one of the bifurcations and the resultant discharge hematocrits at downstream branches are calculated. Due to the concepts of separating surface and

dispersion process. the extent of phase separation in the network depends on the orientation of the side branch. Two geometrical arrangements of the network are employed to study their influences.

The degree of heterogeneity of RBC distribution within a network is another issue of interest. The effect of including the dispersion model on the hematocrit heterogeneity of a network is presented. The flow heterogeneity in a network is also defined to show its correlation with the hematocrit heterogeneity.

6.1 Network generation

The configuration of the vessel network used must be restricted due to some limitations of the streamline mapping technique. The mapping results obtained by using two chords for curved separating surfaces (different sized side branch) need improvement to be satisfactory. Because of this shortcoming the network used in this study will be restricted by having all branches of equal diameter. This closely approximates some microvascular beds. as the diameter ratio of parent to daughter branch decreases with the vessel size. The existing geometrical data from human eye bulbar conjunctiva [71] shows the diameter ratio to be about 1.28 for arterial vessels with diameter of 14 to 18 μm. The microvessels in cat mesentery have mean diameter ratios of 1.22 at vessel sizes of about 10 μm [72].

Due to the uncertainty in matching the density of the dye solution and the working fluid, streamline mapping are not available for the side branch; only the continuing branch is mapped. Although it is believed that at very low Reynolds numbers the branching angle makes neglible difference (the side branch and the continuing branch become similar), the mapping technique is not to be used for the side branch for caution's sake. This leaves one only able to deal with vessel networks where bifurcations branch off the same parent vessel.

The vessel networks used in this study are created by using as many available real parameters as possible. It is emphasized again that no attempt is made to simulate any real vessel network. For the restrictions stated above, two network topologies are selected and shown in Figure 6-1.

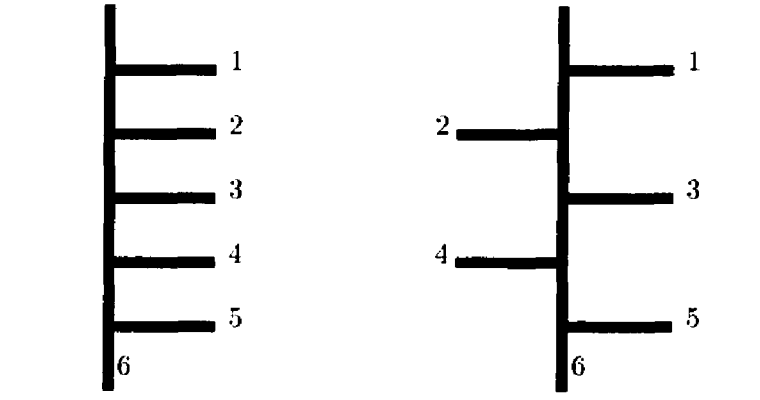

Figure 6-1: Network configurations

One is a series of bifurcations branching off the main vessel on the same side. the other has the bifurcations branching off each side alternatively.

By observing branching river networks, Horton [73] defined a bifurcation ratio as the ratio of the number of streams at a given order to the number of streams at the next higher order. by ordering the network centripetally[1]. He found that the bifurcation ratio tends to be a constant throughout the network. The stream number at different orders is thus given by

$$N_u = R_B^{1-u} N_1. \tag{6.1}$$

where N_u is the number of branches of order number u. R_B is the bifurcation ratio, N_1 is the number of first order segments. Horton also found that the similar relationship applied to the average length of streams of a given order.

$$L_u = R_L^{u-1} L_1 \tag{6.2}$$

where L_u is the average length of a given order u, L_1 is the average length of the first order segnemts and R_L is the length ratio. Fenton and Zweifach [71] applied Horton's stream law in the vascular bed. They used the bifurcation ratio to generate the topology of the

[1]Ordering from the most distal streams, as order 1, toward the larger streams.

vascular network stochastically. In addition, they also found that a similar relationship closely approximates changes in vessel diameters between orders. That is

$$D_u = R_D^{u-1} D_1 \tag{6.3}$$

where D_u represents the average diameter of a given order u. D_1 is the average diameter of the first order vessels and R_D is the diameter ratio.

In the current study the geometric parameters of the networks, if free of restrictions , are all determined in this fashion. *In vivo* experimental data from rabbit omentum arteries [71] suggested a diameter ratio 1.30 with an average capillary diameter of 12.3μm. and a length ratio of 1.61 with an average capillary length of 135 μm. Ordering the network branch centripetally the vessel-size and branch-order has the following correspondence according to Horton's law.

order	1	2	3	4	5	6
diameter(μm)	12.3	16.0	20.8	27.0	35.1	45.7
length(μm)	135	217	350	563	907	1460

To select vessel diameters around 50 μm the corresponding order is 6 and the length is 1460 μm. The η/Pe is then calculated from Equation 5.15. To save the CPU time and exaggerate the effects, this length is cut in half and resulted in the η/Pe to be 0.06 for the following network calculation.

The flow split at each bifurcation is determined stochastically by Popel's flow histogram [74] assuming there is no dispersion on geometric parameters. That is, about 30% of the vessels have the average flow, 25% have three quarters of the average , 25% have one and a quarter of the average , 10% have one and half the average, 10% have one half the average. Among the six branches shown in Figure 6-1 two would have the average flow, the rest have 0.5, 0.75, 1.25, and 1.5 times of the average. The sequence is randomly arranged, from upstream down they are 1.25, 1. 0.75, 1.5, 1, 0.5. The corresponding calculated flow splits, Q*, are then 20%, 20%, 20%, 50%, 70%.

Both flat and 2-phase velocity profiles are used in the dispersion model. Tube size of

the network is assigned to be 50 μm. The plasma gap width used are 2 and 4 μm for flat and 2-phase velocity profiles, respectively.

6.2 Vector comparisons

Hematocrit distribution in a network is expressed as a vector in order to demonstrate its spatial variation and be able to quantitatively compare the heterogeniety of red cell distribution. Each discharge hematocrit of the network branch is assigned to a designated component of a vector based on its geometrical location. Vectors are compared through their deviation from a standard vector. The deviation is defined as the magnitude of their difference. Two presumed standard vectors are used for comparison. One is the hematocrit distribution vector of a network which has the same distribution of flow splits except the red cells have been fully rearranged before approaching the next bifurcation. In this case no diffusion equation is solved to obtain the standard vector. Fractional cell flux F* is calculated directly from Equation 2.7. The discharge hematocrit of each branch is then calculated from the feed hematocrit as

$$(H_d)_{branch} = \frac{F*}{Q*}(H_d)_{feed} \tag{6.4}$$

The other standard hematocrit distribution vector is just the homogeneous hematocrit distribution in which no phase separation has occured. In normalized form it is the unit vector $\vec{I}$.

6.3 Computational results

Discharge hematocrits in each branch of the networks shown in Figure 6-1 are computed. The fractional flow split in the second branch or the third branch are varied as the disturbance, while holding Q* constant in the rest of the branches. The calculated hematocrit is compared with the first standard hematocrit vector (the one with red cells fully rearranged in every vessel segment). This comparison shows whether hematocrit profile rearrangement

makes any difference on red cell distribution in the network. The difference of each corresponding component, ΔH_n, is plotted against Q* at the varying branch. Figure 6-2 shows such a plot when the branches are on the same side of the straight tube (the left configuration in Figure 6-1). The broken lines represent the results when the flow in the second branch is varying, while the solid lines represent the flow variation in the third branch. Each line has an associated number representing the branch number (refer to Figure 6-1). The components of the difference vector, ΔH_n never have values significantly larger than zero, yet some have values as low as -0.2. Therefore, if one defines average hematocrit as a number average, the idea of shifting hematocrit profiles enhances the so called "network Fahraeus effect". The branches farthest downstream have the largest deviations from the total rearrangement case. Notice that the broken and solid curves for branch 5 fall on top of each other. The same is true for branches 4 and 6. This suggests that the location of upstream side branch divisions in flow is not important in determining downstream branch hematocrits; only the cummulative magnitude of the side branch flows is important when all branches are on the same side as the parent vessel. As far as the hematocrits in branches 4, 5 and 6 are concerned, it does not matter if a change in flow rates occurs in branch 2 or 3, the result is nearly the same.

A similar plot is given in Figure 6-3 for the alternating side branch network. Again the components of the difference vector are plotted as a function of Q2* and Q3*. Broken lines represent results for varying Q2* and the solid lines are for changes in Q3*. The magnitude of the difference vector components are much smaller in this case. Obviously the alternating side branch arrangement results in much less network Fahraeus effect in this example. Alternating shifts in the hematocrit profile keep the red cell concentration profile closer to axisymmetry.

In contrast to the same side network, the location of flow variations does make a difference in downstream hematocrits when branches are on alternating sides of the parent. This is most noticable in branch 4 in this case. Increasing the flow into branch 2 results in increased hematocrits for branch 4, yet branch 4 hematocrits decrease when flow is increased

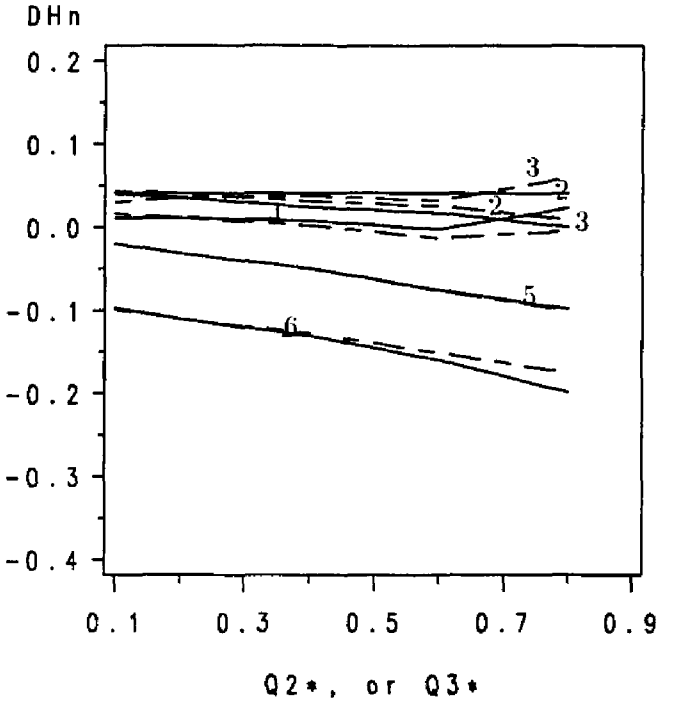

Figure 6-2: Effects of disturbance at different locations for same side branches

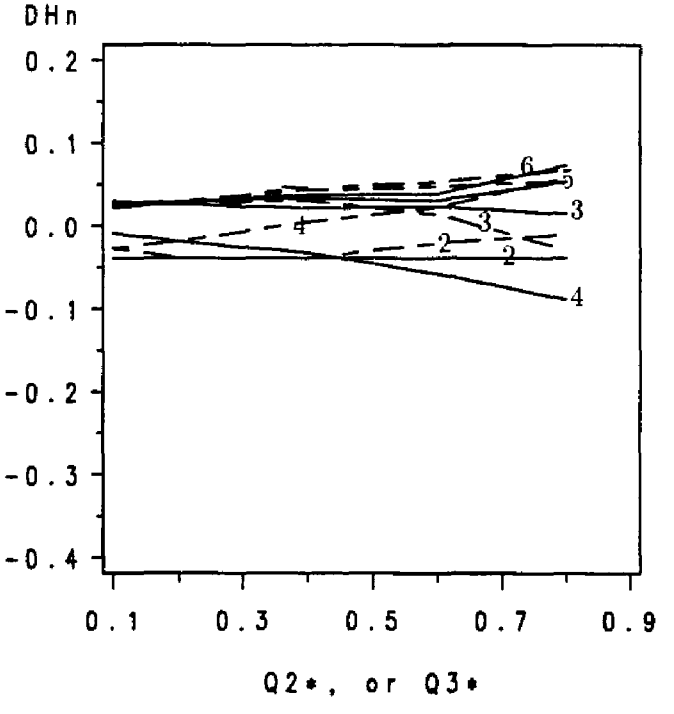

Figure 6-3: Effects of disturbance at different locations for alternating side branches

in branch 3.

Changing the velocity to a 2-phase type profile in the calculation results in curves shown in Figure 6-4 for the same side side branch configuration. The influence attenuation of the disturbance location is also seen in this plot, similar to the results shown in Figure 6-2.

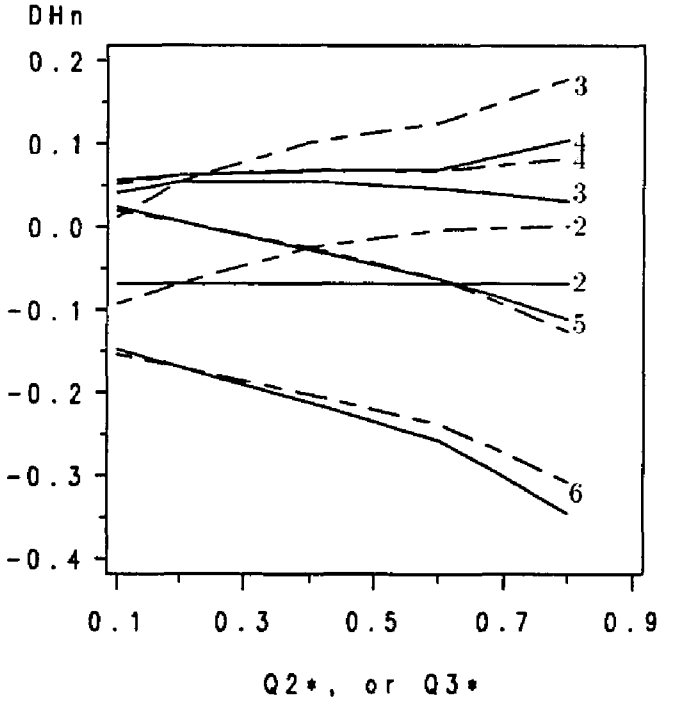

Figure 6-4: Same side for 2-phase velocity profile

In addition to the comparison of the hematocrit distribution vector with the situation where the cells are fully rearranged, the heterogeniety of the hematocrit distribution in a network is also examined. Starting from a normalized feed hematocrit the homogeneous distribution requires that every branch has the same discharge hematocrit, 1. The branch number averaged deviation from the homogeneous hematocrit distribution, $\vec{I}$, defined as

$$\text{Hematocrit heterogeniety} = \frac{\|\vec{H} - \vec{I}\|}{\|\vec{I}\|} = \frac{\|\vec{H} - \vec{I}\|}{\sqrt{n}} = \sqrt{\frac{1}{n}\sum_{n}(H_n - 1)^2}$$

is used as an index to quantify the heterogeniety of a network hematocrit distribution. Figures 6-5 and 6-6 show the index of hematocrit heterogeneity plotted as the ordinate versus

the flow splits in the second or the third branch with the flow split in the fourth branch, Q_4^*, as the third parameter. Figure 6-5 shows the results computed with the dispersion model, while Figure 6-6 shows the results where the red cells are fully rearranged. A flat velocity profile and the same-side side branch network are used in these computations. Three pairs of plots are shown in the figures, each represents the fourth fractional flow split to be 20%, 50%, and 80%. In each pair the broken line represents the results when the flow in the second branch is varying, while the solid line represents the flow variation in the third branch.

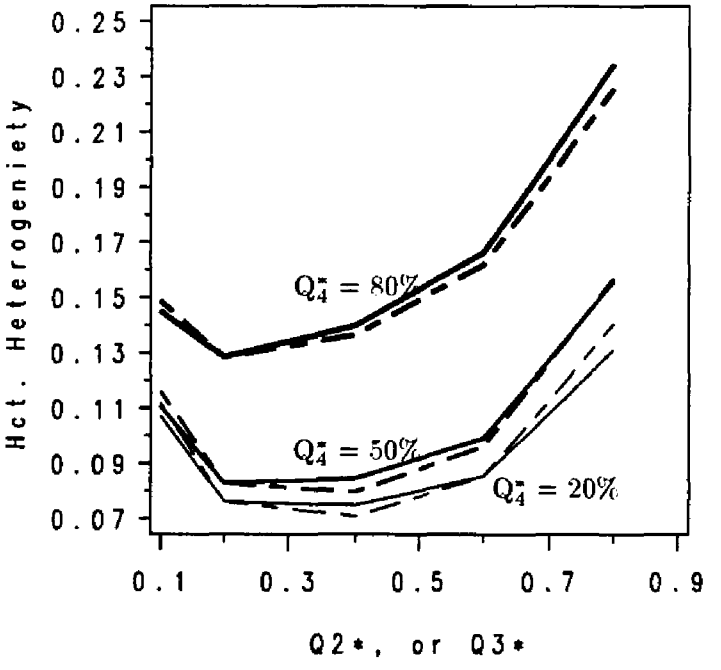

Figure 6-5: Heterogeniety vs. flow variation for same side branching configuration

The first thing to be noted from these plots is that the fully rearranged red cell profile results in a more homogeneous hematocrit distribution. Figure 6-5 again showed that the location of the flow variations is not as important as the variations themselves as far as network heterogeneity is concerned. It is also noted that a flow distribution for the most homogeneous hematocrit distribution exists.

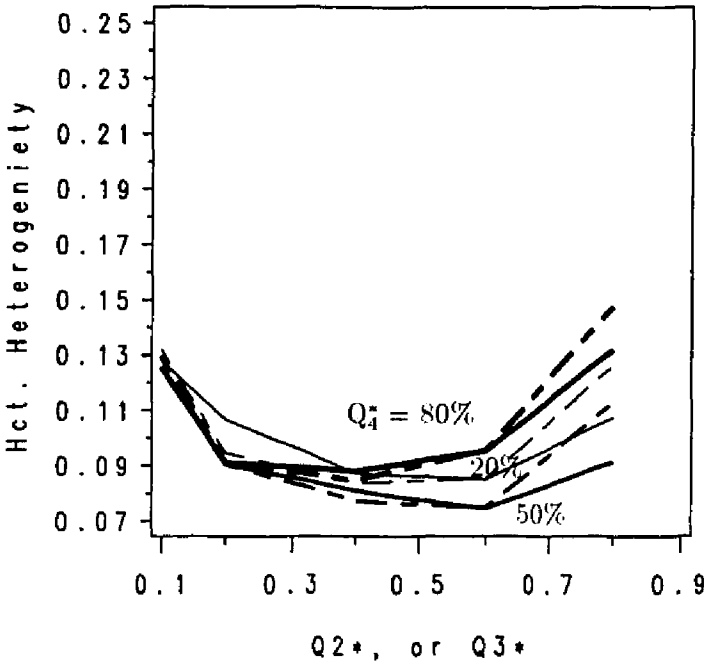

Figure 6-6: Heterogeniety vs. flow variation for fully rearranged red cells.

Based on the concept that the heterogeneity of hematocrit distribution depends on the volumetric flow distribution, a homogeneous flow distribution, also expressed in vector form, is used as the standard to correlate the hematocrit heterogeneity with flow heterogeneity. For the same η/Pe used in previous computations with flat velocity profiles, a flow split distribution of [0.50, 0.24, 0.28, 0.30, 0.30, 0.70] would result in a homogeneous hematocrit distribution, $\vec{I}$. Using this flow distribution as the standard, every flow split vector previously used can be expressed in terms of its deviation from the standard flow distribution which is defined as

$$\text{Flow heterogeniety} = \frac{\|\vec{Q} - \vec{Q}_{standard}\|}{\|\vec{Q}_{standard}\|}$$

Replotting the results presented in Figure 6-5 should show a monotonic relationship. Such a plot is shown in Figure 6-7.

The scattering of results shown in Figure 6-7 is expected because there are multiple flow distributions possible for any specified degree of flow heterogeneity. And not all of these possible flow distribution give the same hematocrit heterogeneity. The range of the scatter

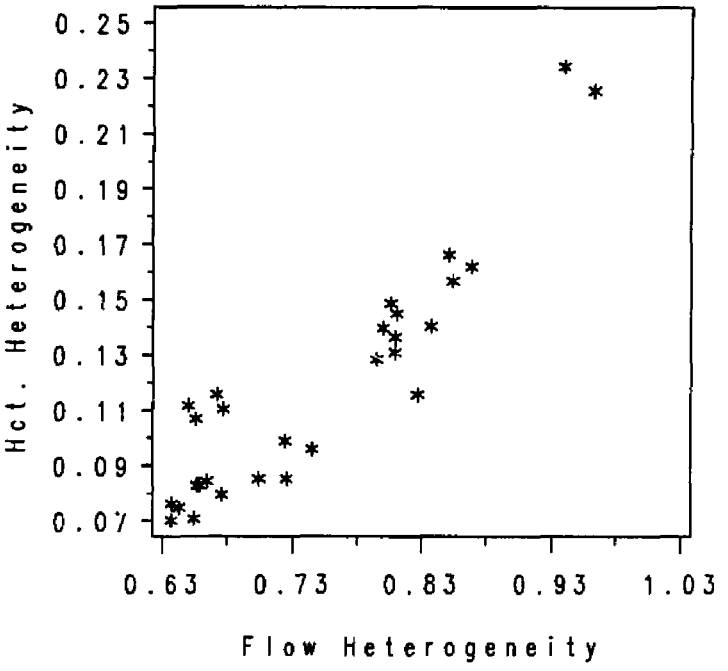

Figure 6-7: Hematocrit heterogeniety vs. flow heterogeniety

represents the span of hematocrit heterogeniety within the same flow heterogeniety.

Chapter 7

Conclusions and Recommendations

In summary, this study has accomplished the measurement of separating surfaces for both equal sized side branches and half sized side branch bifurcations at low Reynolds numbers (< 1). Flat separating surfaces are a good approximation for the case of an equally sized side branch. Arc shaped separating surfaces bulging away from the opening of the side branch are obtained for half sized side branches.

The extent of plasma skimming was calculated for both flat and arc separating surfaces. When a plasma gap of 4 μm in width is used, the shape of the separating surface becomes unimportant if the tube diameter is 30 μm or more.

A mathematical technique for mapping streamlines through a bifurcation was proposed and tested by scaled-up dye experiments. Satisfactory agreements for almost all the branching flow are obtained when the separating surface is a flat one. In the case where the separating surface is arc shaped, the technique needs some modifications for mapping the flow region near the tube wall.

A dispersion type of process has been proposed to describe red cell redistribution across the lumen while blood flows between junctions. A constant diffusion coefficient is assumed in the process. This adjustable lumped parameter, $\mathcal{D}$, is determined by matching the numerical solution of the model equation and the *in vitro* experimental data. The results agree fairly well with the Zydney's correlation derived from collected published data when the effects of shear rate are taken into account. It is thus well confirmed that the dispersion

process is strongly shear rate dependent.

The tested streamline tracing technique and the dispersion model have been applied to a simple vascular networks to calculate the discharge hematocrit distribution. Hematocrit distribution is expressed in vector form for comparison. Noticeable difference was found when the current model is used compared to the case where the asymmetry of the red cell profile is neglected. This difference varied with flow splits in upstream branches of the network. It has been found that the location of the flow splits variations has less influence on the downstream branch hematocrits compared to the magnitude of the variation itself. An index of hematocrit heterogeneity has also been developed to compare the hematocrit distributions. The heterogeneity of hematocrit distribution depends strongly on the flow distribution. A correlation has been attempted for the hematocrit heterogeneity with flow heterogeneity.

The separating surface has played a crucial role in this study. However several questions are left unanswered:

- How does the shape of separating surface vary with the side/parent branch size ratio?
- Concentrated cell suspensions are not likely to have the same velocity profile as that in the dye experiment. How well, then, do the separating surfaces obtained from the dye experiments resemble the actual ones during blood flow?
- Since the solutions for Stokes flow through a tubular junction are not available, how can one map streamlines into the side branches without testing experimentally for more extensive network applications?

Appendix A

Computer Program

The FORTRAN 77 source codes of the body of the finite differencing and major I/O portion are listed below.

```
PROGRAM PARAALL
COMMON CO,NI,NJ,DR,DTHETA,DZ,PE
REAL CNEW(65,50),COLD(65,50),Z,QSTAR(1001)
INTEGER NI,NJ
CHARACTER*20 DFNAME
C INPUT  ************************************************************
DELTA=.16
NI=60
NJ=45
DZ=.02
PE=240
CO=1.
PI=3.141593
DR=(1-DELTA)/NI
DTHETA=PI/NJ
WRITE (*,*) 'Z(START),Z(END),Z(STEP) ?'
READ(*,*) ZSTART,ZEND,ZSTEP
PRINT *,'ZWANT= ?'
READ (*,*) ZWANT
```

```
PRINT *,'EXPT''L DATA IS IN ? FILE (eg. Q30Z24.6)'
READ '(A)',DFNAME
PRINT *,'Q1* = ?'
READ(*,*)Q1STAR
C        ************************************************************
  CALL READIN(QSTAR)
C NOW ALL C'S ARE ZEROS, USED TO DERIVE EQUILIBRIUM ERROR.
CALL calerr(COLD,DFNAME,DELTA,QSTAR,0,0,ERRFIN)
C ASSIGNING INITIAL CONDITION TO NODES
CALL ASSIGN (DELTA,QSTAR,COLD,Q1STAR,F1STAR)
CALL calerr(COLD,DFNAME,DELTA,QSTAR,Q1STAR,F1STAR,ERRINI)
        WRITE(*,*)'ERRINI=',ERRINI,'ERRFIN=',ERRFIN
PREERR=MAX(ERRINI,ERRFIN)
K=0
KKK=0
  150   K=K+1
IF (Z.EQ.ZWANT) THEN
  CALL MKFL(COLD,DELTA,QSTAR,Q1STAR,F1STAR)
  PRINT *,'ZWANT AFTER',ZWANT,'IS ?'
  READ (*,*) ZWANT
ELSE
ENDIF
        CALL ADI (COLD,CNEW)
   Z=K*DZ
ZC=ZSTART+ZSTEP*KKK
IF (ZC.GE.ZEND) ZWANT=Z
IF (ABS(ZC-Z).LE.DZ/2) THEN
          CALL calerr (CNEW,DFNAME,DELTA,QSTAR,Q1STAR,F1STAR,SUMERROR)
```

```
  WRITE (*,*)'THE SUM OF ABS. ERR. AT Z =',Z,'IS',SUMERROR
  IF (SUMERROR.GT.PREERR) THEN
    CALL MKFL (COLD,DELTA,QSTAR,Q1STAR,F1STAR)
    WRITE(*,*)'SECOND DFNAME ?'
    READ '(A)', DFNAME
    WRITE(*,*)'ZSTART,ZEND,ZSTEP = ?'
    READ(*,*)ZSTART,ZEND,ZSTEP
    KKK=0
    CALL CALERR (COLD,DFNAME,DELTA,QSTAR,0,0,ERRFIN)
    PREERR=ERRFIN
  ELSE
    PREERR=SUMERROR
    KKK=KKK+1
  ENDIF
ELSE
ENDIF
DO 130 I=1,NI+1
  DO 140 J=1,NJ+3
    COLD(I,J)=CNEW(I,J)
  140     CONTINUE
  130   CONTINUE
GOTO 150
END
C*********************************************************************
SUBROUTINE READIN(QSTAR)
DIMENSION QSTAR(1001)
OPEN  (UNIT=11,FILE='FLOWFILE.DAT',STATUS='OLD')
DO 1 I=2,1001
```

```
  READ(11,*,END=2) QSTAR(I)
   1    CONTINUE
   2 QSTAR(1)=.5
        QSTAR(1001)=0.0
        RETURN
END
C*********************************************************************
  SUBROUTINE ASSIGN (DELTA,QSTAR,COLD,Q1STAR,F1STAR)
  COMMON CO,NI,NJ,DR,DTHETA,DZ,PE
REAL QY(501),INTEGRAL,QSTAR(1001),COLD(65,50)
PARAMETER (NUM=500)
PI=4*ATAN(1.)
QTOT=1.-Q1STAR
Q1ST=Q1STAR
IF (Q1STAR.GT..5) Q1ST=1-Q1STAR
DO 11 II=1,1001
  IF (QSTAR(II).GE.Q1ST.AND.Q1ST.GE.QSTAR(II+1)) GOTO 12
  11    CONTINUE
  WRITE(*,*)'WRONG AT SEARCHING FOR S'
STOP
  12    S=(-1)**(Q1STAR.GT..5)*((II-1)/1000.)
IF (S.EQ.0)THEN
  F1STAR=.5
ELSE
  CALL FSEVA (DELTA,S,F1STAR)
ENDIF
HMAX=1/((1-DELTA)**2-(1-DELTA)**4/3)
N=20
```

```
C
QY(1)=.5
DO 1 I=2,NUM+1
  Y=(I-1.)/NUM
  XHI=1.
  XLO=SQRT(S**2+Y**2)
  H=(XHI-XLO)/N
  IF (H.LT.0) THEN
    QY(I)=0.
    GOTO 1
  ELSE
  ENDIF
  IF (S.EQ.0)THEN
    SUM=0
  ELSE
    SUM=(S.GT.0)*(-1)*(XLO-XLO**3)*(PI-2*ATAN(Y/S))
  ENDIF
    DO 2 J=2,N
      XI=XLO+(J-1)*H
      IF (S.EQ.0) THEN
        YI=(XI-XI**3)*(PI/2-ASIN(Y/XI))
      ELSE
        YI=(XI-XI**3)*(-PI*(S.GT.0)-((-1)**(S.LT.0))*ATAN(SQRT(
     &            XI**2-S**2)/ABS(S))-ATAN(Y/SQRT(XI**2-Y**2)))
      ENDIF
      IF (MOD(J,2).EQ.0) THEN
SUM=SUM+4*YI
      ELSE
```

```
SUM=SUM+2*YI
      ENDIF
  2     CONTINUE
  INTEGRAL =SUM*H/3
  IF (S.LE.0) GOTO 3
C
  XHI=XLO
  XLO=Y
  H=(XHI-XLO)/N
  SUM=0
  DO 4 IJ=2,N
    XI=XLO+(IJ-1)*H
    YI=(XI-XI**3)*(PI-2*ATAN(Y/SQRT(XI**2-Y**2)))
    IF (MOD(IJ,2).EQ.0) THEN
      SUM=SUM+4*YI
    ELSE
      SUM=SUM+2*YI
    ENDIF
  4       CONTINUE
  SUM=SUM+(XHI-XHI**3)*(PI-2*ATAN(Y/SQRT(XHI**2-Y**2)))
  INTEGRAL=INTEGRAL+SUM*H/3
  3       QY(I)=(2/PI)*INTEGRAL/QTOT
  1     CONTINUE
C
       DO 5 I=1,NI+1
  R=(I-1)*DR
  DO 10 J=2,NJ+2
    THETA=(J-2)*DTHETA
```

```
      XD=R*COS(THETA)
      YD=R*SIN(THETA)
      IF (ABS(XD).LT.0.001) THEN
          QXD=.5
      ELSE
        IF (XD.LT.0) THEN
          QXD=1.-QSTAR(NINT(-XD*1000))
        ELSE
          QXD=QSTAR(NINT(XD*1000))
        ENDIF
      ENDIF
      IF (YD.LT.0.001) THEN
        QYD=.5
      ELSE
        QYD=QSTAR(NINT(YD*1000))
      ENDIF
C     QXD=(QXUP-Q1STAR)/QTOT
      QXUP=QXD*QTOT+Q1STAR
C     QYD=QYUP/QTOT   SINCE QY(I) IS NORMALIZED ALREADY SO...
      QYUP=QYD
C     SEARCH FOR Y
      DO 6 JJ=1,NUM+1
        IF (QY(JJ).GE.QYUP.AND.QYUP.GE.QY(JJ+1)) GOTO 7
    6         CONTINUE
        WRITE (*,*) 'SOMETHING''S WRONG IN SEARCHING QY(I)'
        STOP
    7         YUP=REAL(JJ-1)/NUM
      QXU=QXUP
```

```
      IF (QXUP.GT..5) QXU=1.-QXUP
      DO 8 KK=1,1001
        IF (QSTAR(KK).GE.QXU.AND.QXU.GE.QSTAR(KK+1)) GOTO 9
    8         CONTINUE
        WRITE (*,*) 'SOMETHING''S WRONG IN SEARCHING QXU'
        STOP
    9         XUP=((KK-1)/1000.)*(-1)**(QXUP.GT..5)
      RUP=SQRT(XUP**2+YUP**2)
      IF (RUP.GT.(1-DELTA)) RUP=1-DELTA
      COLD(I,J)=HMAX*(1-(RUP/(1-DELTA))**2-((1.-F1STAR)/
     &         (1-Q1STAR))*(1-(R/(1-DELTA))**2))
    10      CONTINUE
    5     CONTINUE
  CALL BOUNDIMAGE(COLD)
    RETURN
  END
  C*****************************************************************
  SUBROUTINE BOUNDIMAGE (C)
  COMMON CO,NI,NJ,DR,DTHETA,DZ,PE
  DIMENSION C(65,50)
  DO 60 I=1,NI+1
    C(I,NJ+3)=C(I,NJ+1)
    C(I,1)=C(I,3)
    60    CONTINUE
  DO 6 J=1,NJ+3
    C(NI+2,J)=C(NI,J)
    6     CONTINUE
  RETURN
```

```
END
C*********************************************************************
SUBROUTINE ADI (COLD,CNEW)
COMMON CO,NI,NJ,DR,DTHETA,DZ,PE
DIMENSION CNEW(65,50),COLD(65,50),CMID(65,50),A(65,4)
C   C    C     C      C       C        C         C          C       C
CC  SOLVE CMID (HALF ADVANCED CONCENTRATION)
CC  Advance in centerline first
CALL HALFCENTER (HALF,COLD)
DO 80 J=2, NJ+2
  A(1,1)=0
  A(1,2)=(2/DR**2)+(2*PE*(1-DR**2))/DZ
  A(1,3)=-(1/DR**2+1/(2*DR*DR))
  A(1,4)=(COLD(2,J-1)-2*COLD(2,J)+COLD(2,J+1))/(DR*DTHETA)**2
     &     +2*PE*COLD(2,J)*(1-DR**2)/DZ+HALF/(2*DR**2)
          DO 90 I=3,NI
    R=(I-1)*DR
    A(I-1,1)=1/(2*R*DR)-1/DR**2
    A(I-1,2)=2*PE*(1-R**2)/DZ+2/DR**2
    A(I-1,3)=-(1/DR**2+1/(2*R*DR))
            A(I-1,4)=(COLD(I,J-1)-2*COLD(I,J)+COLD(I
     &       ,j+1))/(r*dtheta)**2+2*PE*COLD(I,J)*(1-R**2)/DZ
  90      CONTINUE
  R=NI*DR
  A(NI,1)=-2/DR**2
  A(NI,2)=2*PE*(1-R**2)/DZ+2/DR**2
  A(NI,3)=0
  A(NI,4)=(COLD(NI+1,J-1)-2*COLD(NI+1,J)+COLD(NI+1,J+1))
```

```
     &     /(R*DTHETA)**2+2*PE*COLD(NI+1,J)*(1-R**2)/DZ
   CALL TRIDG (A,NI)
   CMID(1,J)=HALF
   DO 100 I=1,NI
   CMID(I+1,J)=A(I,4)
   100     CONTINUE
   80    CONTINUE
CALL BOUNDIMAGE (CMID)
C    C       C       C       C       C       C     C       C
CC    SOLVE FOR CNEW BY CMID AND COLD
CALL halfCENTER(FULLSTEP,CMID)
DO 7 J=2,NJ+2
   CNEW(1,J)=FULLSTEP
   7     CONTINUE
DO 8 I=2,NI+1
   R=(I-1)*DR
   A(1,1)=0
   A(1,2)=2/(R*DTHETA)**2+2*PE*(1-R**2)/DZ
   A(1,3)=-2/(R*DTHETA)**2
   A(1,4)=(CMID(I-1,2)-2*CMID(I,2)+CMID(I+1,2))/DR**2+(CMID
     &     (I+1,2)-CMID(I-1,2))/(2*R*DR)+2*PE*CMID(I,2)*(1-R**2)/DZ
   DO 9 J=3,NJ+1
     A(J-1,1)=-1/(R*DTHETA)**2
     A(J-1,2)=2/(R*DTHETA)**2+2*PE*(1-R**2)/DZ
     A(J-1,3)=A(J-1,1)
     A(J-1,4)=(CMID(I-1,J)-2*CMID(I,J)+CMID(I+1,J))/DR**2+(CMID
      &       (I+1,J)-CMID(I-1,J))/(2*R*DR)+2*PE*CMID(I,J)*(1-R**2)/DZ
   9       CONTINUE
```

```
  A(NJ+1,1)=-2/(R*DTHETA)**2
  A(NJ+1,2)=2/(R*DTHETA)**2+2*PE*(1-R**2)/DZ
  A(NJ+1,3)=0
  A(NJ+1,4)=(CMID(I-1,NJ+2)-2*CMID(I,NJ+2)+CMID(I+1,NJ+2))
     &      /DR**2+(CMID(I+1,NJ+2)-CMID(I-1,NJ+2))/(2*R*DR)+2*PE*
     &      CMID(I,NJ+2)*(1-R**2)/DZ
  CALL TRIDG (A,NJ+1)
  DO 110 J=1,NJ+1
    CNEW(I,J+1)=A(J,4)
  110      CONTINUE
  8      CONTINUE
CALL BOUNDIMAGE (CNEW)
C   C      C      C      C      C      C      C      C      C      C
RETURN
END
C*********************************************************************
SUBROUTINE HALFCENTER (HALF,C)
COMMON CO,NI,NJ,DR,DTHETA,DZ,PE
DIMENSION C(65,50)
SUM=0
DO 70 J=3,NJ+1
  SUM=SUM+2*C(2,J)
  70     CONTINUE
SUM=SUM+C(2,2)+C(2,NJ+2)
HALF=C(1,1)+DZ*2*(SUM/(NJ*2)-C(1,1))/(PE*DR**2)
RETURN
END
C*********************************************************************
```

```
SUBROUTINE TRIDG (A,N)
DIMENSION A(65,4)
DO 1 I=2,N
  A(I,1)=A(I,1)/A(I-1,2)
  A(I,2)=A(I,2)-A(I,1)*A(I-1,3)
  A(I,4)=A(I,4)-A(I,1)*A(I-1,4)
  1     CONTINUE
C  BACK SUBSTITUTING
NM1=N-1
A(N,4)=A(N,4)/A(N,2)
DO 2 I=NM1,1,-1
C  THE INDEX M WILL COUNT UP THE ROWS
  A(I,4)=(A(I,4)-A(I,3)*A(I+1,4))/A(I,2)
  2     CONTINUE
RETURN
END
C*****************************************************************
SUBROUTINE calerr(C,DFNAME,DELTA,QSTAR,Q1STAR,
     &    F1STAR,SUMERROR)
COMMON CO,NI,NJ,DR,DTHETA,DZ,PE
DIMENSION C(65,50),CN(65,50),QSTAR(1001)
CHARACTER*20 DFNAME
HMAX=1/((1-delta)**2-(1-DELTA)**4/3)
DO 1 I=1,NI+1
  R=(I-1)*DR
  DO 2 J=2,NJ+2
    CN(I,J)=C(I,J)+HMAX*((1.-F1STAR)/(1-Q1STAR))*(1-
     &        (R/(1-DELTA))**2)
```

```
  2   CONTINUE
  1 CONTINUE
  OPEN (UNIT=12,FILE='TEST.DAT',STATUS='SCRATCH')
  CALL INTEGRATION (CN,1.,TNORM)
  DO 180 S=-1,1,.005
    CALL INTEGRATION(CN,S,TOTO)
    FSTAR=TOTO/TNORM
    IF (ABS(S).LT.0.001) THEN
      QS=.5
    ELSE
      IF (S.LT.0) THEN
        QS=QSTAR(NINT(-S*1000))
      ELSE
        QS=1.-QSTAR(NINT(S*1000))
      ENDIF
    ENDIF
    WRITE (12,190)QS,FSTAR
 190        FORMAT (1X,2F12.7)
 180     CONTINUE
OPEN (9,FILE=DFNAME,STATUS='OLD')
SUMERROR=0.
DO WHILE (.TRUE.)
  READ(9,*,END=20)DQ2,DF2
  REWIND (12)
          READ (12,*)CQ2,CF2
  SMALLCQ2=CQ2
  SMALLCF2=CF2
  READ (12,*)CQ2,CF2
```

```
  BIGCQ2=CQ2
  BIGCF2=CF2
  DO WHILE (DQ2 .GT. BIGCQ2)
    SMALLCQ2=BIGCQ2
    SMALLCF2=BIGCF2
    READ (12,*)CQ2,CF2
    BIGCQ2=CQ2
    BIGCF2=CF2
  END DO
IF (SMALLCQ2 .LT. DQ2 .AND. DQ2 .LT. BIGCQ2) THEN
  RATIO=(DQ2-SMALLCQ2)/(BIGCQ2-SMALLCQ2)
  F2=SMALLCF2+RATIO*(BIGCF2-SMALLCF2)
  ERROR2=ABS(DF2-F2)
ELSE
  PRINT *,'SOMETHING''S WRONG2'
  RETURN
ENDIF
SUMERROR=SUMERROR+ERROR2
END DO
  20    CLOSE (9)
CLOSE (12)
RETURN
END
C*****************************************************************
SUBROUTINE MKFL(C,DELTA,QSTAR,Q1STAR,F1STAR)
COMMON CO,NI,NJ,DR,DTHETA,DZ,PE
DIMENSION C(65,50),CN(65,50),QSTAR(1001)
HMAX=1/((1-delta)**2-(1-DELTA)**4/3)
```

```
DO 1 I=1,NI+1
  R=(I-1)*DR
  DO 2 J=2,NJ+2
    CN(I,J)=C(I,J)+HMAX*((1.-F1STAR)/(1-Q1STAR))*(1-
   &        (R/(1-DELTA))**2)
  2   CONTINUE
  1 CONTINUE
  OPEN (UNIT=12,FILE='PLOT.DAT',STATUS='NEW')
  CALL INTEGRATION (CN,1.,TNORM)
  DO 180 S=-1,1,.01
    CALL INTEGRATION(CN,S,TOTO)
    FSTAR=TOTO/TNORM
    IF (ABS(S).LT.0.001) THEN
      QS=.5
    ELSE
      IF (S.LT.0) THEN
        QS=QSTAR(NINT(-S*1000))
      ELSE
        QS=1.-QSTAR(NINT(S*1000))
      ENDIF
    ENDIF
    IF (FSTAR.LT.0.AND.FSTAR.GT.-.001) FSTAR=0
    WRITE (12,190)QS,FSTAR
 190        FORMAT (1X,2F12.7)
 180     CONTINUE
CLOSE (12)
RETURN
END
```

```
C*********************************************************************
SUBROUTINE INTEGRATION(C,S,TOTO)
   COMMON CO,NI,NJ,DR,DTHETA,DZ,PE
DIMENSION C(65,50)
PI=4*ATAN(1.)
TOTO=0
  DO 2 J=2,NJ+2
    THETA=(J-2)*DTHETA
    SUM=0
    IF (S.GE.0.) SUM=C(1,J)*DR**2*(.25-DR**2/32)/NJ
    DO 1 I=2,NI
      R=(I-1)*DR
      X=R*COS(THETA)
      IF (X .LT. S) THEN
        SUM=SUM+C(I,J)*R*DR*(2-2*R**2-DR**2/2)/NJ
            ELSE
      ENDIF
   1     CONTINUE
    R=NI*DR
    X=R*COS(THETA)
    IF (X.LT.S) SUM=SUM+C(NI+1,J)*DR*(R-DR/4+DR**3/32-
     & R**3+.75*R**2*DR-.25*R*DR**2)/NJ
    IF ((J.EQ.2).OR.(J.EQ.NJ+2)) SUM=SUM/2
  TOTO=TOTO+SUM
   2      CONTINUE
TOTO=TOTO*2
RETURN
END
```

```
C*****************************************************************
SUBROUTINE FSEVA (DELTA,S,FS)
INTEGER I,J
PI=4*ATAN(1.)
SC=S
IF (S.LT.0) SC=-S
        N=INT((1.-DELTA-SC)*500)
IF (MOD(N,2).EQ.1) THEN N=N+1
IF (N.EQ.0) STOP
H=(1.-DELTA-SC)/N
SUM=0
DO 1 J=2,N+1
  XI=SC+(J-1)*H
  HXI=(1-(XI/(1-DELTA))**2)/((1-DELTA)**2-(1./3)*(1-DELTA)**4)
  VXI=2/PI*(1-XI**2)
  VAL=ACOS(SC/XI)*XI*HXI*VXI
  IF (J.EQ.N+1) GOTO 2
  IF (MOD(J,2) .EQ. 0 ) THEN
    SUM=SUM+4*VAL
  ELSE
    SUM=SUM+2*VAL
  ENDIF
  1     CONTINUE
  2     SUM=SUM+VAL
FS=2*SUM*H/3
IF (S.LT.0) FS=1.-FS
RETURN
END
```

Appendix B

Numerical Check

The computer program is checked in three ways. First, the convergence and stability are investigated by varying mesh sizes. Second, the mass balance is checked between two axial locations. Third, an analytical solution for an axisymmetric condition is used to compare the results from numerical methods. Flat velocity profile is used throughout the calculation in this chapter.

B.1 Mesh sizes check

By using flat separating surfaces to obtain the flux-flow curve for each concentration profile, the difference between two crossectional concentration profiles is quantified by calculating the area, ΔI, between the two corresponding flux-flow curves. The conditions used in this section are listed below:

- initial condition: Q1*=40%
- dimensionless gap width: G=0.07
- axial location where concentration profile is withdrawn for flux-flow curve comparison: η/Pe=19/240

The calculated ΔI at different mesh sizes are listed below. A reference value of ΔI is the area between the flux-flow curves of the initial concentration profile and the axisymmetric concentration profile which has the value of 2.74×10^{-2}.

Table B.1: Concentration difference, at NJ=45 and $\Delta\eta$/Pe=0.02/240.

NI	$\frac{\Delta\eta/\mathrm{Pe}}{(\Delta\xi)^2}$	ΔI
10	0.010	2.56×10^{-5}
20	0.039	4.44×10^{-6}
30	0.087	2.48×10^{-6}
40	0.154	2.37×10^{-7}
60	0.347	8.61×10^{-6}
70	0.472	4.48×10^{-6}
80	0.617	unstable
90	0.780	unstable

Table B.2: Concentration difference, at NI=60, NJ=45 and Pe=240.

$\Delta\eta$	$\frac{\Delta\eta/\mathrm{Pe}}{(\Delta\xi)^2}$	ΔI
0.002	0.035	6.56×10^{-7}
0.005	0.087	2.65×10^{-6}
0.010	0.173	4.05×10^{-6}
0.020	0.347	8.61×10^{-6}
0.030	0.520	unstable

Table B.3: Concentration difference, at NI=60, $\Delta\eta$/Pe=0.02/240.

NJ	$\frac{\Delta\eta/\mathrm{Pe}}{(\Delta\xi)^2}$	ΔI
20	0.347	1.11×10^{-5}
45	0.347	8.61×10^{-6}
60	0.347	1.54×10^{-6}
80	0.347	2.06×10^{-6}
90	0.347	5.34×10^{-8}
95	0.347	4.94×10^{-7}

B.2 Mass balance check

With Q1*=40% the initial concentration profile gives the totoal red cell flow of 0.7835338 by numerical integration. The concentration profile, calculated by the ADI finite difference method at an axial location $\Delta\eta$/Pe=19/240, results in a total red cell flow of 0.7836066. The difference is less than 0.01%.

B.3 Analytical solution check

The bessel functions in Equation 5.11 are evaluated from IMSL-SFUN, the integral is evaluated by IMSL subroutine QDAGS. The same initial condition for both analytical and numerical calculation is a step function with the jump located at ξ=0.5. The rest of the conditions used are as the same as those used in Section B.1. Using four terms for ths series under the specified conditions gives at least seven figures of accuracy. The comparison of analytical and numerical solution is listed below. Both four terms and ten terms results are listed for the analytical solution.

Table B.4: Concentration distribution at η/Pe=19/240.

	Analytical		Numerical
ξ	4 terms	10 terms	
0.000	0.35645	0.35645	0.36137
0.186	0.34692	0.34692	0.35176
0.372	0.32234	0.32234	0.32696
0.558	0.29288	0.29288	0.29724
0.744	0.27015	0.27015	0.27432
0.930	0.26198	0.26198	0.26608

Table B.5: Concentration distribution at η/Pe=5/240.

ξ	Analytical 4 terms	Numerical
0.000	0.77695	0.78333
0.186	0.70937	0.71605
0.372	0.53075	0.53739
0.558	0.31431	0.31947
0.744	0.15136	0.15446
0.930	0.09473	0.09694

Appendix C

Table C.1: Flux-flow data grouped by z/Q

Q1*=30%				Q1*=40%			
z/Q=24.6 s/mm^2		z/Q=134.2		z/Q=24.4		z/Q=142.0	
Q2*	F2*	Q2*	F2*	Q2*	F2*	Q2*	F2*
0.601	0.614	0.340	0.318	0.264	0.200	0.689	0.702
0.586	0.570	0.681	0.676	0.646	0.640	0.751	0.772
0.507	0.496	0.544	0.534	0.779	0.790	0.208	0.197
0.576	0.563	0.480	0.479	0.688	0.674	0.445	0.447
0.589	0.568	0.869	0.899	0.563	0.468	0.056	0.050
0.443	0.442	0.871	0.890	0.510	0.499	0.320	0.264
0.486	0.474	0.429	0.409	0.563	0.547	0.294	0.244
0.596	0.584	0.329	0.324	0.812	0.820	0.517	0.487
0.234	0.195	0.192	0.181	0.373	0.321	0.463	0.430
0.660	0.656	0.057	0.040	0.318	0.296	0.079	0.078
0.779	0.784	0.557	0.565	0.285	0.231		
0.399	0.374	0.517	0.483	0.563	0.550		
0.693	0.697	0.510	0.494	0.342	0.309		
0.787	0.794	0.792	0.829	0.289	0.270		
0.509	0.491			0.243	0.213		
0.438	0.407			0.220	0.207		
0.486	0.450						

Q1*=50%				Q1*=60%			
z/Q=22.2		z/Q=153.9		z/Q=52.6		z/Q=488.2	
Q2*	F2*	Q2*	F2*	Q2*	F2*	Q2*	F2*
0.359	0.283	0.584	0.550	0.346	0.318	0.541	0.515
0.220	0.140	0.644	0.615	0.425	0.426	0.855	0.898
0.889	0.858	0.753	0.781	0.495	0.497	0.385	0.329
0.229	0.149	0.438	0.409	0.450	0.447	0.492	0.415
0.595	0.568	0.312	0.253	0.519	0.509	0.619	0.619
0.649	0.602	0.165	0.158	0.477	0.480		
0.330	0.262	0.270	0.221	0.486	0.479		
0.179	0.126	0.116	0.045				
0.388	0.335	0.736	0.748				
0.766	0.773	0.625	0.596				
		0.694	0.668				
		0.766	0.691				
		0.414	0.411				
		0.353	0.267				
		0.071	0.061				
		0.171	0.115				

Table C.2: Flux-flow data grouped by η/Pe

$Q1^*$=30%				$Q1^*$=40%	
$(\eta/Pe)_{avg.}$=0.082		$(\eta/Pe)_{avg.}$=0.094		$(\eta/Pe)_{avg.}$=0.094	
$Q2^*$	$F2^*$	$Q2^*$	$F2^*$	$Q2^*$	$F2^*$
0.340	0.318	0.605	0.527	0.209	0.197
0.871	0.890	0.681	0.689	0.445	0.447
0.429	0.409	0.544	0.534	0.056	0.049
0.329	0.324	0.480	0.479	0.320	0.264
0.660	0.656	0.792	0.797	0.646	0.640
0.779	0.784	0.869	0.899	0.779	0.790
0.693	0.697	0.586	0.570	0.517	0.487
0.486	0.450	0.507	0.496	0.079	0.078
		0.087	0.072	0.812	0.820
		0.576	0.563	0.373	0.321
		0.192	0.181	0.318	0.296
		0.057	0.040	0.285	0.231
		0.557	0.565	0.563	0.550
		0.517	0.483	0.342	0.309
		0.510	0.494	0.289	0.270
		0.792	0.829	0.243	0.213
		0.443	0.442	0.220	0.207
		0.486	0.474		
		0.596	0.584		
		0.234	0.195		
		0.399	0.374		
		0.787	0.794		
		0.509	0.491		
		0.438	0.407		

Q1*=50%				Q1*=60%			
$(\eta/Pe)_{avg.}$=0.061		$(\eta/Pe)_{avg.}$=0.095		$(\eta/Pe)_{avg.}$=0.118		$(\eta/Pe)_{avg.}$=0.898	
Q2*	F2*	Q2*	F2*	Q2*	F2*	Q2*	F2*
0.220	0.140	0.606	0.494	0.425	0.426	0.701	0.736
0.889	0.856	0.357	0.348	0.495	0.497	0.855	0.898
0.229	0.149	0.587	0.550	0.450	0.447	0.385	0.329
0.595	0.568	0.644	0.615	0.519	0.509	0.492	0.415
0.649	0.602	0.753	0.781	0.477	0.480	0.619	0.619
0.330	0.262	0.312	0.253	0.486	0.479		
0.179	0.126	0.165	0.158				
0.388	0.335	0.270	0.221				
0.317	0.397	0.116	0.045				
		0.330	0.287				
		0.688	0.613				
		0.742	0.811				
		0.146	0.121				
		0.736	0.748				
		0.625	0.569				
		0.694	0.668				
		0.414	0.411				
		0.353	0.267				
		0.071	0.061				
		0.171	0.115				
		0.311	0.281				
		0.766	0.773				

Appendix D

The experimental data shown include the separating surfaces and streamline tracing. Rectangular coordinates are used and the data listed are normalize by the tube radius.

Table D.1: Side-branch-type separating surfaces, equal diameters.

Q*=5%	x	.636	.681	.687	.691					
	y	.659	-.613	.109	-.085					
10%	x	.604	.574	.608	.603	.541	.558	.505		
	y	.321	-.373	-.011	.562	-.622	.741	-.778		
20%	x	.452	.436	.413	.423					
	y	.104	-.159	.590	-.582					
30%	x	.216	.193	.209	.246	.234	.261	.252	.235	.229
	y	-.004	-.908	.904	.715	-.719	.536	-.540	.324	-.328
40%	x	.024	.117	.098	.106	.097	.094	.107	.084	.067
	y	.000	.276	-.284	.497	-.499	.766	-.764	.960	-.962
50%	x	-.026	.009	-.040	.026	-.014	.014			
	y	.503	-.504	.755	-.756	.268	-.268			
60%	x	-.068	-.072	-.135	-.094	-.104	-.062	-.123	-.064	-.096
	y	.001	.312	-.290	.536	-.534	.705	-.697	.918	-.915
70%	x	-.216	-.247	-.221	-.242	-.251	-.194	-.229	-.195	-.166
	y	.004	.284	-.304	.496	-.492	.677	-.666	.846	-.852
80%	x	-.412	-.400	-.448	-.421	-.421	-.355	-.355		
	y	.007	.414	-.362	.579	-.579	.836	-.836		
90%	x	-.656	-.567	-.604	-.538	-.512				
	y	.011	.547	-.507	.741	-.759				

Table D.2: T-branch (side-branch=feed branch), equal diameter.

Q*=5%	x	-.696	-.699	-.699					
	y	-.012	-.356	.356					
10%	x	-.630	-.589	-.604	-.604	-.626	-.626	-.560	
	y	-.255	.340	.525	-.525	-.696	.696	.000	
20%	x	-.436	-.460	-.460	-.480	-.451	-.438	-.479	
	y	.000	-.373	.373	.552	-.577	-.791	.767	
30%	x	-.184	-.239	-.256	-.234	-.279	-.246	-.270	-.283	-.225
	y	.000	.341	-.328	.526	-.504	.677	-.668	.821	-.838
40%	x	-.040	-.073	-.127	-.099	-.099	-.084	-.119	-.090	-.105
	y	.000	.316	-.298	-.466	.466	.683	-.678	-.855	.854
50%	x	.056	-.023	.023	-.016	.024	.023	-.023	.000	.000
	y	.000	.259	-.259	-.456	.455	.668	-.668	.860	-.860
60%	x	.040	.100	.093	.142	.068	.113	.101	.117	.102
	y	.000	.205	-.208	.412	-.431	-.638	.640	.832	-.834
70%	x	.204	.220	.257	.248	.256	.267	.234	.258	.230
	y	.000	.315	-.285	.466	-.462	.630	-.643	.795	-.804
80%	x	.455	.443	.438	.461	.470	.435	.440		
	y	-.701	.709	-.342	.311	.486	-.518	.000		

Table D.3: Side-branch-type, unequal size (Db/Dp=1/2).

Q*=10%	x	.682	.636	.567	.555	.719	.709	.473
	y	.410	-.479	.314	-.334	.561	-.574	.050
20%	x	.359	.342	.499	.527	.246	.246	
	y	.233	-.258	.535	-.508	.057	-.057	
50%	x	.052	.022	.022	.024	-.014	.005	
	y	.421	-.423	.689	-.685	.260	-.260	
80%	x	-.335	-.363	-.193	-.233			
	y	.536	-.518	.772	-.761			
90%	x	-.236	-.174	-.495	-.480	-.311	-.361	-.533
	y	-.881	.895	.430	-.447	.732	-.709	-.056

Table D.4: At high Reynolds number.

Q*=10%	x	.033	-.114	.272	.219	.105	.030		
	y	.935	-.929	.748	-.765	.858	-.863		
30%	x	-.384	-.490	-.272	-.324	-.048	-.096	.194	.194
	y	.787	-.726	.748	-.727	.686	-.681	.534	-.534
40%	x	.306	.125	.034	-.041	-.132	-.305	-.337	-.557
	y	.257	.468	-.483	.587	-.573	.626	-.609	.597
	x	-.625	-.743	-.798	-.885	-.885			
	y	-.525	.501	-.407	.412	-.412			
50%	x	-.971	-.975	-.745	-.786	-.509	-.599	-.284	-.417
	y	.102	-.034	.430	-.350	.565	-.468	.582	-.496
	x	-.009	-.142						
	y	.516	-.496						

Table D.5: Mapping data, equal diameters (Db/Dp=1).

Q*=18%					
R=0.31		R=0.49		R=0.73	
x	y	x	y	x	y
-0.283	-0.020	-0.468	-0.108	-0.668	-0.179
-0.261	0.111	-0.444	0.062	-0.691	0.085
-0.195	0.233	-0.369	0.240	-0.606	0.350
-0.096	0.314	-0.257	0.367	-0.441	0.544
0.051	0.364	-0.089	0.459	-0.208	0.681
0.182	0.315	0.084	0.533	0.064	0.737
0.284	0.247	0.274	0.456	0.412	0.686
0.427	0.227	0.497	0.403	0.495	-0.634
0.525	0.141	0.743	0.285	0.165	-0.713
0.597	0.063	0.644	-0.357	-0.113	-0.715
0.606	-0.085	0.386	-0.444	-0.379	-0.584
0.522	-0.190	0.121	-0.522	-0.587	-0.396
0.390	-0.294	-0.082	-0.465	-0.660	-0.165
0.245	-0.337	-0.233	-0.387		
0.093	-0.323	-0.367	-0.257		
-0.060	-0.310	-0.470	-0.100		
-0.168	-0.258				
-0.231	-0.128				
-0.278	-0.029				

Q*=50%					
R=0.31		R=0.54		R=0.76	
x	y	x	y	x	y
0.031	0.008	-0.335	-0.122	-0.658	-0.239
0.020	-0.003	-0.318	0.109	-0.678	0.119
0.152	0.088	-0.217	0.288	-0.574	0.387
0.281	0.244	-0.064	0.407	-0.342	0.592
0.470	0.282	0.214	0.530	0.000	0.744
0.542	-0.326	0.272	-0.512	0.051	-0.734
0.211	-0.261	-0.047	-0.446	-0.275	-0.648
0.044	-0.175	-0.236	-0.303	-0.502	-0.452
-0.015	-0.037	-0.331	-0.120	-0.652	-0.163

Q*=82%			
R=0.68		R=0.83	
x	y	x	y
0.217	0.538	-0.475	-0.492
-0.125	0.325	-0.684	-0.012
-0.291	0.073	-0.616	0.341
-0.239	-0.161	-0.286	0.643
0.036	-0.414	0.243	0.796
0.538	-0.502	0.211	-0.734
		-0.296	-0.634
		-0.564	-0.395

Table D.6: Mapping data, unequal diameters (Db/Dp=1/2).

Q*=18%					
R=0.29		R=0.47		R=0.74	
x	y	x	y	x	y
-0.243	-0.026	-0.397	-0.137	-0.687	-0.264
-0.246	0.071	-0.411	0.029	-0.712	0.012
-0.167	0.155	-0.371	0.197	-0.690	0.279
-0.085	0.211	-0.259	0.320	-0.541	0.522
0.004	0.244	-0.120	0.419	-0.340	0.666
0.106	0.250	0.072	0.454	-0.052	0.746
0.243	0.260	0.239	0.430	0.232	0.715
0.391	0.226	0.460	0.334	0.560	0.560
0.598	0.149	0.627	-0.253	0.463	-0.638
0.721	0.101	0.361	-0.374	0.172	-0.744
0.784	0.000	0.135	-0.469	-0.131	-0.745
0.599	-0.106	-0.059	-0.420	-0.387	-0.645
0.457	-0.213	-0.211	-0.381	-0.591	-0.478
0.255	-0.293	-0.339	-0.274	-0.702	-0.269
0.093	-0.285	-0.410	-0.110		
-0.035	-0.250				
-0.119	-0.190				
-0.193	-0.121				
-0.230	-0.028				

Q*=50%					
R=0.30		R=0.45		R=0.73	
x	y	x	y	x	y
0.064	0.008	-0.203	-0.047	-0.654	-0.200
0.000	0.000	-0.205	0.067	-0.695	0.085
0.040	0.069	-0.150	0.192	-0.610	0.352
0.150	0.155	-0.049	0.280	-0.394	0.584
0.371	0.214	0.109	0.356	-0.438	0.561
0.416	-0.231	0.555	0.098	0.219	0.715
0.135	-0.208	0.264	-0.406	0.400	-0.665
-0.005	-0.072	-0.035	-0.334	-0.026	-0.732
0.035	0.007	-0.169	-0.208	-0.343	-0.619
		-0.244	-0.089	-0.548	-0.429
				-0.679	-0.169

Q*=82%			
R=0.65		R=0.80	
x	y	x	y
-0.120	-0.094	-0.545	-0.198
-0.089	0.086	-0.582	0.082
-0.004	0.236	-0.438	0.381
0.352	0.377	-0.169	0.588
0.046	-0.325	0.359	0.647
-0.131	-0.099	0.096	-0.681
		-0.320	-0.493
		-0.522	-0.243

Bibliography

[1] Poiseuille, J. L.(1840). *Compte Rendus*, **11**. 961 and 1041;(1840).**12**. 112.

[2] Baker M. and Wayland, H. (1974). On-line volumetric flow rate and velocity profile measurement for blood microvessels. *Microvasc. Res.*, **7**. 131-143.

[3] Lipowsky H. H. and Zweifach B. W. (1977). Method for the simultaneous measurement of pressure differentials and flow in single unbranched vessels of the microcirculation for rheological studies. *Microvasc. Res.*, **14**. 345-361.

[4] Caro C. G. , Pedley, T. J., Schroter, R. C., and Seed, W. A. (1978). *The mechanics of the circulation*. Oxford.

[5] Kanzow, G., Pries, A. R., and Gaehtgens, P. (1982). Analysis of the hematocrit distribution in the mesenteric microcirculation. *Int. J. Microcirc. Clin. Exp.*, **1**. 67-79.

[6] Schmid-Schönbein, G. W., and Zweifach, B. W. (1975). RBC velocity profiles in arterioles and venules of the rabbit omentum. *Microvasc. Res.*, **10**. 153-164.

[7] Klitzman, B., and Duling, B. R. (1979). Microvascular hematocrit and red cell flow in resting and contracting striated muscle. *Am. J. Physiol.*, **237**, H481-H490.

[8] Klitzman, B., and Johnson, P. C. (1982). Capillary network geometry and red cell distribution in hamster cremaster muscle. *Am. J. Physiol.*, **242**, H211-H219.

[9] Lipowsky, H. H., Usami, S., and Chien, S. (1980). *In vivo* measurements of "apparent viscosity" and microvessel hematocrit in the mesentery of the cat. *Microvasc. Res.*, **19**. 297-319.

[10] Cokelet, G. R. (1982). Speculation on a cause of low vessel hematocrits in the microcirculation. *Microcirc.*, **2**, 1-18.

[11] Wiedeman, M. P., Tuma, R. F., and Mayrovitz, H. N. (1981). *An Introduction to Microcirculation*, Academic Press, New York.

[12] Tyml, K., Ellis, C. G., Safranyos, R. G., Fraser, S., and Groom, A. C. (1981). Temporal and spatial distributions of red cell velocity in capillaries of resting skeletal muscle, including estimate of red cell transit time. *Microvasc. Res.*, **22**, 14-31.

[13] Rand, R. P., and Burton, A. C. (1964). Mechanical properties of the red cell membrane: I. Membrane stiffness and intracellular pressure. *Biophys. J.*, **4**, 303-316.

[14] Hochmuth, R. M., and Mohandas, N. (1972). Uniaxial loading of the red cell mimbrane. *J. Biomech.*, **5**, 501-509.

[15] Cokelet, G. R. (1972). The rheology of human blood, in Y. C. Fung, N.Perrone, and M. Anliker (eds.), *Biomechanics, Its Foundations and Objectives*, Prentice-Hall, Englewood Cliffs, N. J., pp. 63-103.

[16] Chien, S. (1970). Shear dependence of effective cell volume as a determinant of blood viscosity. *Science*, **168**, 977.

[17] Chien, S., Tvetenstrand, C. T., Farrell Epstein, M. A., and Schmid-Schönbein G. W. (1986). Model studies on distributions of blood cells at microvascular bifurcations. *Am. J. Physiol.*, **248**, H568-H576.

[18] Fahraeus, R., and Lindqvist, T. (1931). The viscosity of the blood in narrow capillary tubes. *Am. J. Physiol.*, **96**, 562-568.

[19] Barbee, J. H., and Cokelet, G. R. (1971). Prediction of blood flow in tubes with diameters as small as 29 μm. *Microvasc. Res.*,**3**, 17-21.

[20] Fahraeus, R. (1928). Die Strömungsverhältnisse und die Verteilung der Blutzellen im Gefäßsystem. *Klin. Wochenschr.*, **7**, 100-106.

[21] Goldsmith, H. L. (1971). Red cell motions and wall interactions in tube flow. *Federation Proceedings*, **30**, 1578-1588.

[22] Bugliarello, G. and Sevilla, J. (1970). Velocity distribution and other characteristics of steady and pulsatile blood flow in fine glass tubes. *Biorheology*, **7**, 85-107.

[23] Bugliarello, G., and Hsiao, C. C. (1964). Phase separation in suspensions flowing through bifurcations: A simplified hemodynamic model. *Science*, **143**, 469-471.

[24] Carr, R. T. (1984). Plasma Skimming in Replicas of Microvascular Bifurcations. PhD thesis, University of Rochester.

[25] Phibbs, R. H. and Burton, A. C. (1968). *Hemorheology*, edited by A. L. Copley, Pergamon, Oxford, pp. 617.

[26] Palmer, A. A. (1965). Axial drift of cells and partial plasma skimming in blood flowing through glass slits. *Am. J. Physiol.*, **209**, 1115-1122.

[27] Krogh, A. (1922). *The Anatomy and Physiology of Capillaries*, Yale University, New Haven, CT.

[28] Pappenheimer, J. R. (1956). Role of the red blood corpuscles in the glomerular regulation of renal blood flow and filtration rate. *Physiologist*, 1(3):8-24.

[29] Yen, R. T., and Fung, Y. C. (1978). Effect of velocity distribution on red cell distribution in capillary blood vessels. *Am. J. Physiol.*, **235**, H251-H257.

[30] Øfjord, E. S., Clausen, G. , and Aukland, K. (1981). Skimming of microspheres in vitro: Implications for measurement of intrarenal blood flow. *Am. J. Physiol.*, **241**, H342-H347.

[31] Øfjord, E. S., and Clausen, G. (1983). Intrarenal flow of microspheres and red cells, skimming in slit and tube models. *Am. J. Physiol.*, **245**, H429-H436.

[32] Pries, A. R., Albrecht, K. H., and Gaehtgens, P. (1981). Model studies on phase separations at a capillary orifice. *Biorheology*, **18**, 355-367.

[33] Dellimore, J. W., Dunlop, M. J., and Canham, P. B. (1983). Ratio of cells and plasma in blood flowing past branches in small plastic channels. *Am. J. Physiol.*, **244**, H635-643.

[34] Svanes, S. R., and Zweifach, B. W. (1968). Variations in small blood vessel hematocrits produced in hypothermic rats by micro-occlusion. *Microvasc. Res.*, **1**, 210-221.

[35] Johnson, P. C. (1971). Red cell separation in the mesenteric capillary network. *Am. J. Physiol.*, **221**, 99-104.

[36] Johnson, P.C., Blaschke, J., Burton, K. S., and Diol, J. H. (1971). Influence of flow variations on capillary hematocirt in mesentery. *Am. J. Physiol.*, **221**, 105-112.

[37] Fenton, B. M., Carr, R. T. and Cokelet, G. R. (1985). Nonuniform red cell distribution in 20 to 100 μm bifurcations. *Microvasc. Res.*, **29**, 103-126.

[38] Perkkio, J., Wurzinger, L. J., and Schmid-Schönbein, H. (1987). Plasma and platelet skimming at T-junctions. *Thrombosis Research*, **45**, 517-526.

[39] Dedrick, R. L. (1988). Arterial drug infusion: Pharmacokinetic problems and pitfalls. *J. Nat. Cancer Inst.*, **80.2**, 84-89.

[40] Barbee, J. H. (1971). The flow of human blood through capillary tubes with inside diameters between 8.7 and 2.21 microns. PhD thesis, California Institute of Technology.

[41] Schmid-Schönbein, G. W., skalak, R., Usami, S., and Chien, S. (1980). Cell distribution in capillary networks. *Microvasc. Res.*, **19**, 18-44.

[42] Charm, S. E., and Kurland, G. S. (1974). *Blood Flow and Microcirculation*, John Wiley and Sons, New York, Chapter 3.

[43] Perkkio, J., and Keskinen, R. (1983). Hematocrit reduction in bifurcations due to plasma skimming. *Bull. Math. Biol.*, **45**, 41-50.

[44] Pries, A. R., Ley, K., Claassen, M., Gaehtgens, P. (1989). Red cell distribution at Microvascular bifurcations. *Microvasc. Res.*, **38**, 81-101.

[45] Lipowsky, H. H., Rofe, S., Tannenbaum, L., Firrell, J. C., Usami, S, Chien, S. (1981). Microvessel hematocrit distributions at bifurcations. *Microvasc. Res.*, **21**, 249-250.

[46] Levine, R. and Goldsmith, H. L. (1977). Particle Behavior in Flow through Small Bifurcations. *Microvasc. Res.*, **14**, 319-344.

[47] Segre, G. , Silberberg, A. (1962a). Behavior of macroscopic rigid spheres in Poiseulle flow. *J. Fluid Mech.*, **14**, 115-136.

[48] Segre, G. , Silberberg, A. (1963). Non-Newtonian behavior of dilute suspension of macroscopic spheres in a capillary viscometer. *J. Colloid Sci.*, **18**, 312.

[49] Thomas, H. W., French, R. J., Groom, A. C., and Rowlands, S. (1965). in *Proceedings of the 4th International Conference on Rheology* (A. L. Copley, Ed.), Wiley, New York, pp. 381.

[50] Goldsmith, H. L., Mason, S. G. (1967). The microrheology of dispersions. In Rheology-Theory and Applications, **4** (ed. F. R. Eirich). Academic.

[51] Eckstein, E. C., Bailey, D. G., Shapiro, A. H. (1977). Self-diffusion of particles in shear flow of a suspension. *J. Fluid Mech.*, **79**, 191-208.

[52] Everage, A. E., Jr. (1973). Theory of bicomponent flow of polymer melts. I. Equilibrium Newtonian tube flow. *Trans. Soc. Rheol.*, **17**, 629-646.

[53] Southern, J. H., and Ballman, R. L. (1973). Stratified bicomponent flow of polymer melts in a tube. *Appl. Polymer Symp.*, **20**, 175-189.

[54] Joseph, D. D. (1984). Instability of the flow of two immiscible liquids with different viscosities in a pipe. *J. Fluid Mech.*, **141**, 309-317.

[55] Everage, A. E., Jr. (1975). Theory of stratified bicomponent flow of polymer melts. II, Interface motion in transient flow. *Trans. Soc. Rheol.*, **19**, 509-522.

[56] Lamb, H. (1932). *Hydrodynamics*. 6th Ed., Cambridge University Press.

[57] Yih, C. S. (1977). *Fluid Mechanics*, West River Press, Ann Arbor, MI, pp. 12-16.

[58] Karino, T., Kwong, H. H. W., and Goldsmith, H. L. (1979). Particle flow behavior in models of branching vessels. I. Vortices in 90° T-junctions. *Biorheology*, **16**, 231-248.

[59] Stoltz, J. F., Larcan, A., and Wackenheim, E. (1973). Etude theorique et experimentale du concept de zone d'influence a une bifuracation du lit vasculaire. *Angiologica*, **10**, 1-9.

[60] Deakin, M. A. B., and Blest, D. C. (1970). Flow at the junction of two pipes: The shape of the separating surface. *Nature* (London), **226**, 259-260.

[61] Pinchak, A. C., and Ostrach, S. (1976). Blood flow in branching vessels. *J. Appl. Physiol.*, **41**, 646-658.

[62] Gerald, C.F., Wheatley, P. O. (1984). *Applied Numerical Analysis*, 3rd. Ed., Addison-Wesley Pub. Co.

[63] Carslaw, H. S., and Jaeger, J. C. (1959). *Conduction of Heat in Solids*, Oxford. pp.204.

[64] Carr, R. T., and Wickham L. L. (1990). Plasma Skimming in Serial Microvascular Bifurcations. *Microvasc. Res.* (accepted for publication, March 1990).

[65] Carr, R. T. (1989). Estimation of hematocrit profile symmetry recovery length downstream from a bifurcation. *Biorheol.*, **26**, 907-920.

[66] Zydney, A. L., and Colton, C. K. (1988). Augmented solute transport in the shear flow on a concentrated suspension. *PhysicoChem. Hydrodyn.*, **10.1**, 77-96.

[67] Leighton, D. and Acrivos, A. (1987). Measurement of shear-induced self-diffusion in concentrated suspensions of spheres. *J. Fluid Mech.*, **177**, 109-131.

[68] Leighton, D. and Acrivos, A. (1987). The shear-induced migration of particles in concentrated suspensions. *J. Fluid Mech.*, **181**, 415-439.

[69] Pries, A. R., Ley, K., and Gaehtgens, P. (1986). Generalization of the Fahraeus principle for microvessel networks. *Am. J. Phisiol.*, **251**, H1324-H1332.

[70] Ley, K., Lindbom, L., and Arfors, K. -E. (1988). Haematocrit distribution in rabbit tenuissimus muscle. *Acta. Physiol. Scand.*, **132**, 373-383.

[71] Fenton, B. M., Zweifach, B. W. (1981). Microcirculatory model relating geometrical variation to changes in pressure and flow rate. *Annals Biomed. Eng.*, **9**, 303-321.

[72] Zweifach, B. W., and Lipowsky, H. H. (1977). Quantitative studies of microcirculatory structure and function. III. Microvascular hemodynamics of cat mesentery and rabbit omentum. *Circ. Res.*, **41**, 380-390.

[73] Horton, R. E. (1945). Erosional development of streams and their drainage basins: hydrophysical approach to quantitative morphology. *Bull. Geol. Soc. Am.*, **56**, 275-370.

[74] Popel, A. S. (1987). Network models of peripheral circulation. *Handbook of bioengineering*. R. Skalak and S. Chien, eds. McGraw Hill, New York.